True Three-Dimensional Proximity Effect Correction in Electron-beam Lithography: Control of Critical Dimension and Sidewall Shape

by

Qing Dai

A dissertation submitted to the Graduate Faculty of
Auburn University
in partial fulfillment of the
requirements for the Degree of
Doctor of Philosophy

Auburn, Alabama
May 4, 2013

Keywords: Electron-beam Lithography, Proximity Effect Correction, Three-dimensional, Resist Profile, Critical Dimension, Sidewall Shape

Copyright 2013 by Qing Dai

Approved by

Soo-Young Lee, Professor of Electrical and Computer Engineering
Stanley Reeves, Professor of Electrical and Computer Engineering
Bogdan Wilamowski, Professor of Electrical and Computer Engineering

Abstract

One of the major limiting factors in electron-beam (e-beam) lithography is the geometric distortion of written features due to electron scattering, i.e., proximity effect, which puts a fundamental limit on the minimum feature size and maximum pattern density that can be realized. A conventional approach to proximity effect correction (PEC) is, through two-dimensional (2-D) simulation, to determine the dose distribution and/or shape modification for each feature in a circuit pattern such that the written pattern is as close to the target pattern as possible. For circuit patterns with nanoscale features, it is not unusual that the actual written pattern is substantially different from the written pattern estimated by a 2-D PEC method. One of the reasons for this deviation is that the 2-D model ignores the exposure variation along the resist depth dimension.

Earlier, it was shown that three-dimensional (3-D) PEC which considers the variation of exposure along the resist depth dimension would be required for nanoscale features, especially for feature size well below 100 nm. In 3-D PEC, the resist profile estimated through simulation of resist development process was employed instead of the exposure distribution, in order to obtain more realistic results.

However, It has been demonstrated that in order to minimize any deviation from a target resist profile, a 3-D PEC scheme must check the estimated resist profile during the dose optimization procedure. One practical issue of such an approach to 3-D PEC is that a time-consuming resist development simulation needs to be carried out in each iteration of the dose optimization for each feature. For the case of large-scale circuit patterns, such a feature-by-feature correction procedure would be too time-consuming to be practical. Also, it has been shown that the dose distribution of "V-shape", which is used by most 2-D PEC

schemes, is not optimal for realizing a vertical sidewall of the resist profile, especially when the total dose is to be minimized.

In this dissertation, the characteristics of our 3-D exposure model are further analyzed and utilized for accurate estimation of resist profiles. Our true 3-D PEC method is also extended to applications for large-scale circuit patterns. A variety of optimizations are developed in order to improve the correction efficiency, such as path-based resist development simulation, critical-location-based dose control, etc. New types of dose distributions are derived under our 3-D exposure model and 3-D PEC method for achieving better sidewall shapes with total dose being minimized. For improving the correction efficiency without sacrificing the correction quality, a dose optimization scheme with a systematic type-based dose updating procedure is developed which is adaptable to different dose distribution types. A dose determination scheme is also developed which can adaptively determine the optimal dose distribution type and the minimum of required total dose based on a given circuit pattern and substrate system settings. The results from extensive simulation along with experiments are provided for performance analysis.

Acknowledgments

First of all, I would like to express my gratitude to my advisor Dr. Soo-Young Lee for leading me into this exciting research area of proximity effect correction in electron-beam lithography and providing me with valuable support throughout my doctoral program. Without his detailed guidance and helpful suggestions this dissertation would not have been possible. I thank him for his patience and encouragement that carried me on through difficult times. I appreciate his vast knowledge and skills in many areas that greatly contributed to my research and this dissertation.

Special thanks are also given to the other members of my committee, Dr. Stanley Reeves and Dr. Bogdan Wilamowski, for their valuable assistance and comments. I also benefited a lot from the courses taught by them.

I would like to extend my gratitude to former and current members of our research group. I would like to thank Pengcheng Li, Xinyu Zhao, and Rui Guo for our memorable collaborations in learning and improving PYRAMID. Thanks are also due to Samsung Electronics Co., Ltd. for funding this research.

Finally, I am greatly indebted to my parents, Xichao Dai and Xuyan Xie, for their support to me through my entire life, and in particular to my wife, Rong Zhang, for her love, patience, and understanding.

Table of Contents

Abstract ii

Acknowledgments iv

List of Figures viii

List of Tables xix

1 Introduction 1

1.1 Problem Definition 1

1.2 Background Review 2

1.2.1 Dose Modification PEC Techniques 3

1.2.2 Shape Modification PEC Techniques 10

1.2.3 Distinctive PEC Techniques 12

1.2.4 Hybrid PEC Techniques 15

1.2.5 Summary 16

1.3 Motivation and Objectives 18

1.4 Organization of Dissertation 19

2 Essential Models in Electron-beam Lithography 21

2.1 Electron-beam Lithography 21

2.2 Point Spread Function 22

2.3 Exposure Model 25

2.4 Development Method 26

2.4.1 Exposure-to-rate Conversion Formula 27

2.4.2 Cell Removal Method 28

2.4.3 Proposed Path-based Method 29

2.4.4 Results and Discussion 36

3 Estimation of Resist Profile for Line/Space Patterns . . . 42
3.1 Introduction . . . 42
3.2 Conventional Estimation Approach . . . 43
3.3 Proposed Estimation Approach . . . 43
3.3.1 Base Patterns . . . 43
3.3.2 2-D Exposure Model . . . 45
3.3.3 Layer-based Exposure Model . . . 46
3.4 Estimation Procedure . . . 48
3.5 Results and Discussion . . . 53
3.5.1 Line/Space Patterns . . . 53
3.5.2 Simulation Results . . . 53
3.5.3 Performance Comparison . . . 57
3.5.4 Experimental Results . . . 60
3.6 Summary . . . 61
4 Critical Dimension Control for Large-scale Uniform Patterns . . . 62
4.1 Introduction . . . 62
4.2 Large-scale Uniform Patterns . . . 63
4.3 Correction Methods . . . 63
4.3.1 2-D Exposure Correction (2-D PEC) . . . 64
4.3.2 3-D Resist Profile Correction (3-D PEC) . . . 65
4.4 Proposed Correction Procedure . . . 66
4.4.1 Correction of a Single Feature . . . 67
4.4.2 Feature-wise Global Adjustment . . . 67
4.4.3 Critical-location-based Dose Control . . . 71
4.5 Results and Discussion . . . 74
4.5.1 Test Patterns . . . 74
4.5.2 Simulation Results . . . 75

4.5.3 Performance Comparison 79
4.6 Summary 80
5 Sidewall Shape Control: Vertical Sidewall 82
5.1 Introduction 82
5.2 Dose Distribution Types 83
5.2.1 Conventional Type 84
5.2.2 Proposed Types 86
5.3 Dose Optimization Scheme 91
5.3.1 Fast Exposure Computation 91
5.3.2 Critical-path-based Resist Development Simulation 93
5.3.3 Type-based Dose Updating 94
5.4 Dose Determination Scheme 97
5.5 Sidewall Shape Control for Large-scale Uniform Patterns 100
5.6 Sidewall Shape Control for Large-scale Nonuniform Patterns 103
5.7 Results and Discussion 106
5.7.1 Performance Comparison for Single Features 106
5.7.2 Performance Comparison for Large-scale Uniform Patterns 114
5.7.3 Performance Comparison for Large-scale Nonuniform Patterns 126
5.7.4 Dependency on Feature and Lithographic Parameters 139
5.8 Summary 143
6 Conclusions 145
Bibliography 148

List of Figures

2.1 Illustration of the e-beam binary lithographic process. 22

2.2 PSF for the substrate system of 300 nm PMMA on Si with the beam energy of 50 KeV. 23

2.3 Monte Carlo simulation of (a) electron paths (cross-section) and (b) energy distribution (cross-section). 24

2.4 Illustration of the substrate system where H is the initial thickness of resist. . . 25

2.5 Illustration of the remaining resist profile after the resist development process. . 26

2.6 The experiment-based nonlinear exposure-to-rate conversion formula. 27

2.7 Illustration of the cell removal method where the dashed curve represents a cross-section of resist profile. 28

2.8 Illustration of the path-based method where the dashed curve represents a cross-section of resist profile. 29

2.9 A path turns to (a) only the positive direction of the X-axis at the point (x, y, z) if $r(x, y, z) > r(x + \Delta x, y, z)$ but $r(x, y, z) \leq r(x - \Delta x, y, z)$ and (b) both the positive and negative directions of the X-axis at the point (x, y, z) if $r(x, y, z) > r(x + \Delta x, y, z)$ and $r(x, y, z) > r(x - \Delta x, y, z)$. 30

2.10 The development paths with one and two turns where the black and gray lines are the vertical and lateral path segments, respectively, and the dashed curve represents a cross-section of resist profile. The Z-axis corresponds to the resist depth dimension. 31

2.11 The computation of each path terminates when the sum of the time spent on its path segments is equal to the given developing time T. 32

2.12 (a) All the points in the resist are marked as "undeveloped" before the resist development simulation. (b) After one path is computed, the points which it passes through are marked as "developed". (c) After another path is computed, more points are marked as "developed". (d) The final resist profile is determined by tracing the boundaries between those developed points and those which are not. 33

2.13 Flowchart of the computation of a two-turn path, where Δt_x, Δt_y, and Δt_z ($\Delta t_x+\Delta t_y+\Delta t_z = T$) are the time spent on the path segment in the X-dimension, Y-dimension, and Z-dimension, respectively, and **p** is the vector representation of the path in the 3-D space. 35

2.14 The layout of (a) Pattern I and (b) Pattern II. 37

2.15 Contours (top view) of resist profiles for Pattern I at the (a) top, (c) middle, and (e) bottom layers of resist by the cell removal method, and at the (b) top, (d) middle, and (f) bottom layers of resist by the path-based method. 38

2.16 Contours (top view) of resist profiles for Pattern II at the (a) top, (c) middle, and (e) bottom layers of resist by the cell removal method, and at the (b) top, (d) middle, and (f) bottom layers of resist by the path-based method. 39

3.1 Illustration of the conventional estimation approach where both exposing step and developing step are simulated. 44

3.2 Cross-section of the resist profile of a base pattern. 45

3.3 Difference in estimation of remaining resist profiles between 2-D model and 3-D model through (a) linear mapping ($r = e$) and (b) nonlinear mapping ($r = e^2$). . 46

3.4 Distribution curves of layer-based exposure of three arbitrary points in (a) the exposed area and (b) the unexposed area on the substrate system of 500 nm PMMA on Si. The curves were obtained through computing the 3-D exposure distribution. 48

3.5 The developing process can be modeled as two separate parts, i.e., vertical development and lateral development. 49

3.6 Depth at x, $d(x)$, may be modeled as a combination of vertical component $d_V(x)$ and lateral component $d_L(x)$. 50

3.7 Estimation of the lateral component $d_L(x)$: (a) the initial resist profile $d(x)$, (b) after the lateral component for point x_1 is estimated, and (c) after the estimation for all points is completed. 51

3.8 Flowchart of the proposed estimation method. 52

3.9 Cross-section of the resist profile of a line/space pattern. 53

3.10 Remaining resist profiles of an 8-line pattern with (a) L = 100 nm/S = 100 nm and (b) L = 100 nm/S = 200 nm on the substrate system of 300 nm PMMA on Si. 54

3.11 Remaining resist profiles of an 8-line pattern with (a) L = 100 nm/S = 100 nm and (b) L = 100 nm/S = 200 nm on the substrate system of 500 nm PMMA on Si. 55

3.12 Remaining resist profiles of an 8-line pattern with (a) L = 100 nm/S = 100 nm and (b) L = 100 nm/S = 200 nm on the substrate system of 1000 nm PMMA on Si. 56

3.13 Average and maximum percent depth errors with respect to (a) the ratio of L to S with N = 8 on the substrate system of 1000 nm PMMA on Si; (b) the number of lines with L = 100 nm/S = 100 nm on the substrate system of 500 nm PMMA on Si; (c) the developed depth (controlled by the developing time) with L = 100 nm/S = 100 nm and N = 8 on the substrate system of 1000 nm PMMA on Si; (d) the resist thickness (PMMA thickness) with L = 100 nm/S = 100 nm and N = 8. 59

3.14 Experimental results of (a) resist profile of set I measured from the SEM image; (b) resist profile of set II measured from the SEM image; (c) resist profile of set I estimated from that of set II; (d) resist profile of set II estimated from that of set I. 60

4.1 The deviation of resist profiles at corner, edge and center of a large-scale uniform pattern without PEC. 64

4.2 The target 2-D exposure distribution is illustrated for a line feature. 65

4.3 The cross-section of resist profile is illustrated for a line feature where p_j and q_j are the actual and target widths at the j-th layer, respectively, where the resist is modeled by 10 layers. 66

4.4 Illustration of (a) the region-wise dose distribution within the feature before correction, (b) the region-wise dose distribution within the feature after correction, (c) the corresponding resist profile before correction, and (d) the corresponding resist profile after correction. 68

4.5 For each location (m, n) of the feature (line segment), $d(i)$ is weighted by the deconvolution surface $A(m, n,)$. 69

4.6 The exposure distributions obtained using the global (weighted) dose distribution. 70

4.7 The corresponding resist profiles at (a) corner, (b) edge, and (c) center of the pattern from the exposure distributions obtained using the global (weighted) dose distribution. 70

4.8 Line segments only at the critical locations of the pattern are corrected individually. 71

4.9 The adjusted dose distributions for (a) corner, (b) edge, and (c) center of the pattern. 72

4.10 (a) The corresponding exposure distributions and (b) the corrected resist profile using the adjusted dose distributions. 72

4.11 Flowchart of the proposed correction procedure. 73

4.12 Critical locations (marked by ∘) and test locations (marked by ⋄) in a test pattern. 74

4.13 Cross-section resist profiles without correction (i.e., uniform dose) at the critical locations ((a) corner, (b) edge and (c) center; refer to Fig. 4.12) and the test locations ((d), (e) and (f); refer to Fig. 4.12). 76

4.14 Cross-section resist profiles achieved by 2-D PEC method at the critical locations ((a) corner, (b) edge and (c) center; refer to Fig. 4.12) and the test locations ((d), (e) and (f); refer to Fig. 4.12). 77

4.15 Cross-section resist profiles achieved by 3-D PEC method at the critical locations ((a) corner, (b) edge and (c) center; refer to Fig. 4.12) and the test locations ((d), (e) and (f); refer to Fig. 4.12). 78

5.1 The region-wise feature partition with a uniform dose distribution. 84

5.2 The target 2-D exposure distribution is illustrated for a line feature. 85

5.3 The cross-section of resist profile is illustrated for a line feature where p_j and q_j are the actual and target widths at the j-th layer, respectively, where the resist is modeled by 10 layers. 87

5.4 Comparison of (a) the uniform dose distribution and (b) the corresponding distribution curves of 3-D exposure along Z-dimension (resist depth), with (c) a non-uniform dose distribution and (d) the corresponding distribution curves of 3-D exposure along Z-dimension (resist depth) at three points (A, B, and C) on the substrate system of 300 nm PMMA on Si. 88

5.5 The resist profile during development process (a) at time T_1, (b) at time T_2, and (c) at time T for Type-V case, respectively, where $T_1 < T_2 < T$. 89

5.6 The resist profile during development process (a) at time T_1, (b) at time T_2, and (c) at time T for Type-M case, respectively, where $T_1 < T_2 < T$. 90

5.7 The resist profile during development process (a) at time T_1, (b) at time T_2, and (c) at time T for Type-A case, respectively, where $T_1 < T_2 < T$. 91

5.8 The exposure distribution of the top, middle and bottom layers of resist when only (a) the two edge regions, (b) the two middle regions, and (c) the center region are exposed with a unit dose. 92

5.9 The outer width errors and the inner width errors defined at the cross-section of resist profile. 93

5.10 The resist profile (a) before dose updating and (b) after dose updating for Type-V case, respectively. 94

5.11 The resist profile (a) before dose updating and (b) after dose updating for Type-M case, respectively. 95

5.12 The resist profile (a) before dose updating and (b) after dose updating for Type-A case, respectively. 95

5.13 Flowchart of the proposed dose optimization scheme. 96

5.14 The critical path for (a) Type-V case, (b) Type-M case, and (c) Type-A case, respectively. 98

5.15 Flowchart of the proposed dose determination scheme for a specific dose distribution type. 99

5.16 Flowchart of the improved dose optimization scheme with the proposed dose determination scheme. 101

5.17 Flowchart of the correction procedure for large-scale uniform patterns. 102

5.18 Flowchart of the correction procedure for large-scale nonuniform patterns. . . . 104

5.19 A feature is partitioned into 5 regions (a) along X-dimension and (b) along Y-dimension, respectively. The region-wise dose distribution (c) in X-dimension ($d_{m,n}(x)$) and (d) in Y-dimension ($d_{m,n}(y)$) after correction, respectively. 105

5.20 Illustration of the 2-D interpolation for computing the 2-D region-wise dose distribution $d_{m,n}(x, y)$. 106

5.21 Cross-section resist profiles: (a) the uniform dose distribution, (b) the Type-V dose distribution, (c) the Type-M dose distribution, and (d) the Type-A dose distribution on the substrate system of 100 nm PMMA on Si. 107

5.22 Cross-section resist profiles: (a) the uniform dose distribution, (b) the Type-V dose distribution, (c) the Type-M dose distribution, and (d) the Type-A dose distribution on the substrate system of 300 nm PMMA on Si. 108

5.23 Cross-section resist profiles: (a) the uniform dose distribution, (b) the Type-V dose distribution, (c) the Type-M dose distribution, and (d) the Type-A dose distribution on the substrate system of 500 nm PMMA on Si. 109

5.24 Cross-section resist profiles: (a) the uniform dose distribution (total dose $430\mu C/cm^2$), (b) the Type-V dose distribution (total dose $320\mu C/cm^2$), (c) the Type-M dose distribution (total dose $250\mu C/cm^2$), and (d) the Type-A dose distribution (total dose $230\mu C/cm^2$) on the substrate system of 300 nm PMMA on Si. 111

5.25 Cross-section resist profiles at the corner location of Pattern I: (a) the uniform dose distribution, (b) the Type-V dose distribution, (c) the Type-M dose distribution, and (d) the Type-A dose distribution on the substrate system of 300 nm PMMA on Si without considering the variation of background exposure. 115

5.26 Cross-section resist profiles at the edge location of Pattern I: (a) the uniform dose distribution, (b) the Type-V dose distribution, (c) the Type-M dose distribution, and (d) the Type-A dose distribution on the substrate system of 300 nm PMMA on Si without considering the variation of background exposure. 116

5.27 Cross-section resist profiles at the center location of Pattern I: (a) the uniform dose distribution, (b) the Type-V dose distribution, (c) the Type-M dose distribution, and (d) the Type-A dose distribution on the substrate system of 300 nm PMMA on Si without considering the variation of background exposure. 117

5.28 Cross-section resist profiles at the corner location of Pattern I: (a) the uniform dose distribution, (b) the Type-V dose distribution, (c) the Type-M dose distribution, and (d) the Type-A dose distribution on the substrate system of 300 nm PMMA on Si. 119

5.29 Cross-section resist profiles at the edge location of Pattern I: (a) the uniform dose distribution, (b) the Type-V dose distribution, (c) the Type-M dose distribution, and (d) the Type-A dose distribution on the substrate system of 300 nm PMMA on Si. 120

5.30 Cross-section resist profiles at the center location of Pattern I: (a) the uniform dose distribution, (b) the Type-V dose distribution, (c) the Type-M dose distribution, and (d) the Type-A dose distribution on the substrate system of 300 nm PMMA on Si. 121

5.31 Cross-section resist profiles at the corner location of Pattern II: (a) the uniform dose distribution, (b) the Type-V dose distribution, (c) the Type-M dose distribution, and (d) the Type-A dose distribution on the substrate system of 100 nm PMMA on Si. 122

5.32 Cross-section resist profiles at the edge location of Pattern II: (a) the uniform dose distribution, (b) the Type-V dose distribution, (c) the Type-M dose distribution, and (d) the Type-A dose distribution on the substrate system of 100 nm PMMA on Si. 123

5.33 Cross-section resist profiles at the center location of Pattern II: (a) the uniform dose distribution, (b) the Type-V dose distribution, (c) the Type-M dose distribution, and (d) the Type-A dose distribution on the substrate system of 100 nm PMMA on Si. 124

5.34 Five test locations in the test nonuniform pattern. 126

5.35 Cross-section resist profiles in X-dimension at the test location 1 of the nonuniform pattern: (a) the uniform dose distribution, (b) the Type-V dose distribution, (c) the Type-M dose distribution, and (d) the Type-A dose distribution on the substrate system of 300 nm PMMA on Si without considering the variation of pattern density. 128

5.36 Cross-section resist profiles in Y-dimension at the test location 1 of the nonuniform pattern: (a) the uniform dose distribution, (b) the Type-V dose distribution, (c) the Type-M dose distribution, and (d) the Type-A dose distribution on the substrate system of 300 nm PMMA on Si without considering the variation of pattern density. 129

5.37 Cross-section resist profiles in X-dimension at the test location 5 of the nonuniform pattern: (a) the uniform dose distribution, (b) the Type-V dose distribution, (c) the Type-M dose distribution, and (d) the Type-A dose distribution on the substrate system of 300 nm PMMA on Si without considering the variation of pattern density. 130

5.38 Cross-section resist profiles in Y-dimension at the test location 5 of the nonuniform pattern: (a) the uniform dose distribution, (b) the Type-V dose distribution, (c) the Type-M dose distribution, and (d) the Type-A dose distribution on the substrate system of 300 nm PMMA on Si without considering the variation of pattern density. 131

5.39 Cross-section resist profiles in X-dimension at the test location 1 of the nonuniform pattern: (a) the uniform dose distribution, (b) the Type-V dose distribution, (c) the Type-M dose distribution, and (d) the Type-A dose distribution on the substrate system of 300 nm PMMA on Si. 133

5.40 Cross-section resist profiles in Y-dimension at the test location 1 of the nonuniform pattern: (a) the uniform dose distribution, (b) the Type-V dose distribution, (c) the Type-M dose distribution, and (d) the Type-A dose distribution on the substrate system of 300 nm PMMA on Si. 134

5.41 Cross-section resist profiles in X-dimension at the test location 4 of the nonuniform pattern: (a) the uniform dose distribution, (b) the Type-V dose distribution, (c) the Type-M dose distribution, and (d) the Type-A dose distribution on the substrate system of 300 nm PMMA on Si. 135

5.42 Cross-section resist profiles in Y-dimension at the test location 4 of the nonuniform pattern: (a) the uniform dose distribution, (b) the Type-V dose distribution, (c) the Type-M dose distribution, and (d) the Type-A dose distribution on the substrate system of 300 nm PMMA on Si. 136

5.43 Cross-section resist profiles in X-dimension at the test location 5 of the nonuniform pattern: (a) the uniform dose distribution, (b) the Type-V dose distribution, (c) the Type-M dose distribution, and (d) the Type-A dose distribution on the substrate system of 300 nm PMMA on Si. 137

5.44 Cross-section resist profiles in Y-dimension at the test location 5 of the nonuniform pattern: (a) the uniform dose distribution, (b) the Type-V dose distribution, (c) the Type-M dose distribution, and (d) the Type-A dose distribution on the substrate system of 300 nm PMMA on Si. 138

List of Tables

2.1 Profile difference between the cell removal method and the path-based method. 40

2.2 Simulation time of the cell removal method and the path-based method. 40

2.3 Speedup of the path-based method to the cell removal method. 40

3.1 Average and maximum percent depth errors with respect to the ratio of L to S with N = 8 on the substrate system of 1000 nm PMMA on Si. 57

3.2 Average and maximum percent depth errors with respect to the number of lines with L = 100 nm/S = 100 nm on the substrate system of 500 nm PMMA on Si. 58

3.3 Average and maximum percent depth errors with respect to the developed depth (controlled by the developing time) with L = 100 nm/S = 100 nm and N = 8 on the substrate system of 1000 nm PMMA on Si. 58

3.4 Average and maximum percent depth errors with respect to the resist thickness (PMMA thickness) with L = 100 nm/S = 100 nm and N = 8. 58

4.1 Average and maximum percent width errors in resist profiles of Pattern I for no correction, 2-D PEC method and 3-D PEC method. 79

4.2 Average and maximum percent width errors in resist profiles of Pattern II for no correction, 2-D PEC method and 3-D PEC method. 80

5.1 Average and maximum percent width errors in resist profiles of 50 nm feature size for uniform, Type-V, Type-M and Type-A dose distributions. 112

5.2 Average and maximum percent width errors in resist profiles of 100 nm feature size for uniform, Type-V, Type-M and Type-A dose distributions. 112

5.3 The best dose distribution type with the minimum of required total dose under a variety of system parameters. 113

5.4 Average and maximum percent width errors in resist profiles of Pattern I on the substrate system of 300 nm PMMA on Si for uniform, Type-V, Type-M and Type-A dose distributions without considering the variation of background exposure. 118

5.5 Average and maximum percent width errors in resist profiles of Pattern I on the substrate system of 300 nm PMMA on Si for uniform, Type-V, Type-M and Type-A dose distributions. 125

5.6 Average and maximum percent width errors in resist profiles of Pattern II on the substrate system of 100 nm PMMA on Si for uniform, Type-V, Type-M and Type-A dose distributions. 125

5.7 Average and maximum percent width errors in X-dimension of resist profiles of the nonuniform pattern for uniform, Type-V, Type-M and Type-A dose distributions on the substrate system of 300 nm PMMA on Si without considering the variation of pattern density. 127

5.8 Average and maximum percent width errors in Y-dimension of resist profiles of the nonuniform pattern for uniform, Type-V, Type-M and Type-A dose distributions on the substrate system of 300 nm PMMA on Si without considering the variation of pattern density. 132

5.9 Average and maximum percent width errors in X-dimension of resist profiles of the nonuniform pattern for uniform, Type-V, Type-M and Type-A dose distributions on the substrate system of 300 nm PMMA on Si. 139

5.10 Average and maximum percent width errors in Y-dimension of resist profiles of the nonuniform pattern for uniform, Type-V, Type-M and Type-A dose distributions on the substrate system of 300 nm PMMA on Si. 139

5.11 Region-wise dose contrast for the Type-V dose distribution. 141

5.12 Region-wise dose contrast for the Type-M dose distribution. 142

5.13 Region-wise dose contrast for the Type-A dose distribution. 143

Chapter 1
Introduction

Electron-beam (e-beam) lithography plays an important role in nanofabrication, being able to transfer high-resolution circuit patterns onto the resist. However, as the feature size decreases well below micron into nanoscale, blurring in the written pattern caused by the proximity effect due to electron scattering in the resist puts a fundamental limit on the minimum feature size and maximum pattern density that can be realized. The importance of developing effective schemes for correcting the proximity effect has been well recognized and extensively investigated for a long time, and various methods were proposed and implemented by many researchers. This dissertation addresses a specific issue in true three-dimensional (3-D) proximity effect correction (PEC) in e-beam lithography, i.e., control of critical dimension (CD) and sidewall shape. The main goal of our work is to design practical and effective methods for minimizing the deviation of resist profile from the target one in terms of CD error and sidewall shape, while minimizing the total dose. This chapter provides the problem definition and background review along with the motivation and objectives of this dissertation.

1.1 Problem Definition

The proximity effect in e-beam lithography is an effect due to forward-scattering of electrons in the resist and backscattering of electrons from the substrate. The electron scattering leads to undesired exposure (e-beam energy deposited) of the resist in the unexposed regions adjacent to those exposed by the e-beam, which in turn causes changes in the dissolution rate of the resist. Therefore, the unexposed regions receiving the scattered electrons are

also partially developed, which results in circuit patterns with dimensions different from the target ones.

In general, the scattering of electrons causing the proximity effect can be modeled as a convolution of the dose (e-beam energy given) distribution of a circuit pattern with a proximity function [1]. The proximity function, usually referred to as the point spread function (PSF), is radially symmetric and shows how the electron energy is distributed throughout the resist when a single point is exposed.

While the resist is inherently 3-D, most PEC schemes developed so far employ a two-dimensional (2-D) model where the exposure variation along the resist depth dimension is not taken into account. In other words, a 3-D PSF is not directly used in correction but averaged along the resist depth dimension to obtain a 2-D PSF.

In the previous work [94, 95, 96], the limitations of 2-D PEC were analyzed and the need for 3-D PEC was well demonstrated for circuit patterns with nanoscale features. In [95], the idea of true 3-D PEC was proposed and its first implementation for a single line and a small number of lines was reported. In this implementation, the resist profile estimated through simulation of resist development process was employed instead of the exposure distribution, in order to obtain more realistic results.

In this dissertation, an extension of the true 3-D PEC method for specific applications is described. A challenge is that a 3-D PEC method requires a tremendous amount of computation due to the increased dimensionality and simulation of resist development process.

1.2 Background Review

It is well known that the proximity effect can be reduced or corrected by appropriate measures, including physical techniques and software-based techniques [2]-[102].

The physical techniques are to modify the physical conditions of the e-beam lithography systems or the physical characteristics of resists, such as high beam energy technique [5], low

beam energy technique [5, 47, 51], substrate material optimization technique [6], multilayer resists technique [15], intermediate layer technique [56], etc.

Experimental results show that these physical techniques provide a possible way to reduce the proximity effect, however they can only reduce it to some extent, with drawbacks and limitations. For example, the multilayer resists technique requires a complicated resist process step which introduces extra complexity and does not work for circuit patterns with feature size of 1 μm or less. The high beam energy technique and the low beam energy technique are also affected by the backscattering range and the resist thickness, respectively.

Therefore, most of previous work was focused on developing practical and effective software-based correction schemes in order to eliminate the proximity effect completely, which is presented in detail as below.

1.2.1 Dose Modification PEC Techniques

Self-consistent Method

The first work in this specific type of PEC schemes was done by Parikh in 1978 [2, 7, 8, 9], who developed a self-consistent PEC method for resist exposure. The purpose of this PEC method is to compute the dose which must be applied in order to obtain identical average absorbed (incident plus backscattered) exposure in the resist in each written shape of the pattern addressed by the e-beam.

The self-consistent PEC method can be formulated mathematically by solving the following set of linear equations:

$$\begin{cases} E_T = I_{11} \cdot D_1 + I_{12} \cdot D_2 + \cdots I_{1N} \cdot D_N \\ E_T = I_{21} \cdot D_1 + I_{22} \cdot D_2 + \cdots I_{2N} \cdot D_N \\ \vdots \\ E_T = I_{N1} \cdot D_1 + I_{N2} \cdot D_2 + \cdots I_{NN} \cdot D_N \end{cases}, \qquad (1.1)$$

where N is the number of shapes, E_T is the required target exposure for each shape, D_i is the dose given for shape i, and I_{ij} is the proximity interaction between shape i and shape j.

The integral defining the proximity interaction I_{ij} between shape i and shape j with area A_i and area A_j is given by:

$$I_{ij} = \int_{A_i} \int_{A_j} \mathrm{psf}(r) dA_j dA_i, \tag{1.2}$$

where psf(r) is the PSF.

In general, the integral in Eq. 1.2 cannot be evaluated explicitly for two arbitrary shapes, i.e., a general formula does not exist. However, Parikh derived an analytical expression for evaluating the proximity interaction between two rectangular shapes. For any other types of shape, such as trapezoid, it can be approximated by a set of rectangles, which has the same total area as the original shape. Then the proximity interaction between two arbitrary shapes can be approximated by a summation of the proximity interactions between these rectangular components. Since the proximity interaction between two rectangular shapes can be computed rather exactly, one can split the whole pattern into rectangles before correction and set up the proximity interaction matrix I in Eq. 1.1. Once the proximity interaction matrix I is computed, the N linear equations in Eq. 1.1 can be uniquely solved for each D_i, i.e., the corrected dose for each shape.

Later many researchers developed various PEC methods based on the self-consistent PEC method to further improve its correction accuracy and efficiency.

One limitation of the self-consistent PEC method is that it relies only on the constraint that the average exposure in the resist is identical within the exposed area of each written shape. Therefore, it does not take the exposure in the regions not addressed by the e-beam into account. In order to solve this issue, Parikh developed another PEC method, i.e., the unaddressed-region compensation method [7], which attempts to account for the exposure in the unaddressed regions between shapes. The unaddressed regions, also known as the unexposed area, receive undesired exposure due to electron scattering, which has to

be minimized. Therefore, the purpose of this PEC method is to make the exposure below a specific value in the unexposed area while the identical average exposure is still received in each exposed shape. Note that this PEC method can be considered as an expansion of the self-consistent PEC method as the latter one is a special case of the former one when the exposure threshold for the unexposed area becomes large enough.

In Parikh's self-consistent PEC method, average exposure in each exposed shape is computed by integrating the exposure over the shape. However, Phang and Ahmed pointed out that the exposure value at the edge of the exposed shape is more important for obtaining accurate pattern fidelity of the fabricated structure. Based on this conclusion, they developed a PEC method for line patterns [4]. In this PEC method, for an exposed line element, a dose is required such that the edge of the exposed line element has an exposure equal to E_T, i.e., the threshold of exposure for the dissolution of the resist. This is the fundamental principle involved in obtaining pattern fidelity between the designed and the actual fabricated structure. Similar to the self-consistent PEC method, an exposure equation to compute the the exposure at the edge of a line element is set up for each exposed line element. Then the dose of each line element can be derived by solving a set of linear equations.

Carroll pointed out that Parikh's self-consistent PEC method is not general as its model is based on equality constraints which requires exactly as many constraints as variables. He developed a PEC method based on inequality constraints which is far more general and can have arbitrarily many constraints [11, 16]. In this PEC method, N pixels on the resist surface is chosen for exposure computation. For those pixels in the exposed area, their exposure values are required to be not smaller than a target threshold E_{T1} (but not have to be equalized), while for those pixels in the unexposed area, their exposure values are required to be not larger than another target threshold E_{T2}. Through this way, N inequality constraints can be formed with N dose values as variables. In general, a system of this form is usually underdetermined, thus a cost function is employed to help solving this underdetermined

system. In the cost function, the total dose which represents the total exposure time, is to be minimized. The best solution can be derived through linear programming approach.

As mentioned before, the computation of average exposure results in a single exposure value for each shape, i.e., each exposed shape is considered as a whole in Parikh's self-consistent PEC method. Kratschmer developed a new PEC method in which each exposed shape is partitioned into elements in order to gain more flexibility in dose control and thus achieve better exposure distribution [12]. In this PEC method, each shape is first partitioned to account for the intra proximity effect, then the subshapes at the edges of each shape are further partitioned to account for the inter proximity effect. The setting up and solving of exposure equations are the same as in the self-consistent PEC method, but here each exposure equation corresponds to a partitioned element rather than a whole shape. By appropriate partitioning, the number of linear equations can be limited to reduce the computation time.

For a pattern of N shapes, the implementation of the self-consistent PEC method requires the computation of N^2 proximity interaction coefficients I_{ij}. This number can be reduced to $N(N+1)/2$ as matrix I is symmetric ($I_{ij} = I_{ji}$) according to the reciprocity principle, which however is still a significant amount of computation. A series of approaches was employed in order to reduce the computation time, including Otto and Griffith's parallel processing approach [28, 29] and Vermeulen et al.'s clustering approach [33]. By applying those approaches, the linear equation set in Eq. 1.1 is decomposed into a number of independent linear equation sets of lower order which are handled independently, thus the correction speed can be remarkably increased.

Transform-based Method

In 1983, Chow et al. proposed that the PEC problem can be solved by employing conventional image processing approaches, based on which they developed a transform-based PEC method [18].

In this PEC method, the required dose distribution $d(x)$ is solved through direct deconvolution of the target exposure distribution $e(x)$ with the PSF $\mathrm{psf}(x)$, which is given by:

$$d(x) = e(x) \circledast^{-1} \mathrm{psf}(x). \tag{1.3}$$

The above deconvolution can also be implemented in the frequency domain using the forward and inverse Fourier transforms, which is given by:

$$d(x) = F^{-1}\left[\frac{F[e(x)]}{F[\mathrm{psf}(x)]}\right]. \tag{1.4}$$

Note that unlike the above-mentioned self-consistent PEC methods in which the corrected dose is constant within each shape or partitioned element, the transform-based PEC method is based on the pixel level, thus derives an extremely accurate solution for the dose distribution which is almost exact.

However, this simple PEC method suffers from two major problems. The first problem is that the solved dose distribution has negative values at some locations due to the Gibbs phenomenon from the Fourier transform, which cannot be physically realized. To solve this problem, the method applies corner rounding to the target exposure distribution to minimize the negative dose values in the solution. Then the remaining negative values is further removed by adding a constant to the solved dose distribution to sufficiently guarantee the positive condition. The second problem is that the solved dose distribution contains too much details from rapid oscillations, thus results in an extremely large data base, which is unmanageable and inefficient. The method solve this problem based on an approximation process by introducing the Walsh transform thinning algorithm to reduce the detail part while preventing the deterioration of the effective dose. Through Walsh transform, the data base compression is achieved, and the final data is stored in the form of its Walsh coefficients.

Since the Fourier transform can be implemented using its fast algorithm on special purpose computing hardware, the computation time of this method can be greatly reduced.

Haslam et al. later further improved this PEC method and verified it through experiments [22, 25, 27]. The most notable improvement was to extent the application of this method from simple one-dimensional line patterns to two-dimensional general patterns. In order to achieve further data compression, the data thinning algorithm employs the more powerful two-dimensional Haar transform instead of the previous Walsh transform. An additional benefit of using the Haar transform is that its fast algorithm can be implemented by the same computing hardware which is used for the fast Fourier transform. Eisenmann et al. later achieved a further reduction of the computation time by separating the calculation into correction related and pattern related steps [55, 61].

Approximate Formula-based Method

In 1989, Abe et al. found that the forward-scattered electron range can be assumed to be negligibly small especially for the cases of high beam energy or thin resist thickness. Based on this assumption, they developed a PEC method which utilizes an approximate dose correction formula [35].

In this PEC method, the corrected dose $D(x)$ for a specific feature is derived by the following approximate formula:

$$D(x) = D_0(1 - kU(x)), \tag{1.5}$$

where D_0 is the initial dose for each feature, and k is a parameter selected to minimize the relative error of exposure. The function $U(x)$ corresponds to the exposure caused by the backscattered electrons, which is given by:

$$U(x) = \frac{1}{\pi\beta^2} \int_A \exp\left[-\frac{(x - x')^2}{\beta^2}\right] dx', \tag{1.6}$$

where β is as described in the double-Gaussian PSF (refer to Eq. 2.1), and the region A is the exposed area within 3β from the center of the feature.

The first and second terms of Eq. 1.5 corresponds to the initial dose and the background dose by the backscattered electrons, respectively. Therefore, the corrected dose $D(x)$ for a specific feature is approximated by subtracting its background dose from the initial dose D_0. In order to reduce the computation time, the function $U(x)$ can be modified into another form which contains only the mathematical error function erf(z) by dividing or approximating all the features of the circuit pattern into rectangles, where the values of the error function table can be predetermined for fast referring.

Abe et al. later further accelerate the correction speed by adding the pattern inversion method and the data compaction method, and installed it into a high beam energy e-beam direct writing system [32]. A more powerful representative figure method is later employed to further reduce the computation time with negligible error being introduced [42, 63].

Pattern Area Density Map Method

In 1992, Murai et al. developed a PEC method adjusting dose by referring to a pattern area density map which is calculated by utilizing the fixed size of square meshes [46].

In this PEC method, the circuit pattern is partitioned with a fixed sized mesh. The mesh size is chosen such that the variation of exposure by the backscattered electrons within a single mesh site is negligible. The pattern area density λ, which is defined as the ratio of the exposed area to the total area in a region, is computed in each mesh site, giving a pattern area density map for the circuit pattern. The λ map is then convolved with a smoothing filter, giving a smoothed λ map, i.e., λ_{sm} map. Each circuit feature is then partitioned into rectangles, and a λ' value is assigned to each rectangle which is the linear interpolation of the λ_{sm} values of the four nearest mesh sites to the rectangle. Finally, a corrected dose is assigned to each rectangle which is given by:

$$D = C\frac{2(1+\eta)}{1+2\lambda'\eta}, \tag{1.7}$$

where η is as described in the double-Gaussian PSF (refer to Eq. 2.1), and C is a constant depending on the specific resist and beam energy used.

The determination of the mesh size is important because the correction error depends on the mesh size and the smoothing range. In order to reduce the error, a small mesh size and a wide smoothing range are desirable, which however needs to be compromised with the amount of map size. The smoothing filter is based on a form of template convolution where the forward scattering is neglected for fast computation purpose.

Kasuga et al. later improved the correction accuracy of this PEC method by employing an adaptive partition and dose adjustment algorithm based on the gradient vector from the pattern area density map [64]. Ea and Brown further enhanced this PEC method by reducing the correction error using an iterative algorithm and a framing procedure [76], and incorporating it with a corner correction scheme [82].

Other Methods

Other dose modification PEC methods include Greeneich's dose compensation curve method [14], Pavkovich's integral equation approximate solution method [23], Gerber's splitting equation exact solution method [26], Frye's adaptive neural network method [40], Aristov et al.'s simple compensation method [49], Rau et al.'s nonlinear optimization method [62], Watson et al.'s inherent forward scattering correction method [68], etc.

1.2.2 Shape Modification PEC Techniques

Empirically-determined Method

The history of the shape modification PEC techniques began as early as the dose modification PEC techniques. In 1978, Sewell developed the first PEC method in this specific area

[3]. The core part of this PEC method is that although the change in the pattern dimensions during fabrication depends on parameters such as beam current, beam scan frequency, developing time, developing temperature, etc., there is a basic relationship between the designed pattern dimensions and the pattern dimensions after development. Therefore, the changes in the designed pattern dimensions to compensate the influence of proximity effect could yield patterns with the correct dimensions in the resist. By analyzing the changes in the actual measured pattern dimensions for different amount of dose values from experimental results, a set of empirical curves is derived to set up design tables. For a design table, a specific feature is chosen as the control feature to set the exposure condition such that all resist exposed above a specific value is developed, and the rest of the pattern dimensions are all adjusted using this exposure threshold. Based on the design table, the pattern dimensions after development can be predicted, and the designed pattern dimensions are adjusted to compensate the proximity effect.

Analytically-determined Method

In 1979, Parikh analytically modeled the relationship between the designed pattern dimensions and the pattern dimensions after development, and pointed out that this leads to an underdetermined system of nonlinear equations, whose solution is extremely difficult and impractical for an arbitrary shape [7]. However, for simple shapes such as squares and infinitely long lines, the solution is possible to derive as only one dimension variable (e.g., width) needs to be considered for each shape. In 1980, he developed a shape-dimension adjustment method in which exact solutions can be obtained for simple shapes based on analytical calculation instead of the empirical method [10].

In this PEC method, the formulation of intra proximity effect and inter proximity effect lead to a set of simultaneous nonlinear equations, which is individually given by.

$$E_T = \frac{1}{2(1+\eta)}\left[f(\alpha) + \eta f(\beta)\right], \tag{1.8}$$

where α, β, and η are as described in the double-Gaussian PSF (refer to Eq. 2.1), E_T is the threshold of exposure for the dissolution of the resist, and the function $f(x)$ is given by:

$$f(x) = \text{erf}\left(\frac{w_a}{2x}\right)\left[\text{erf}\left(\frac{w_a - w_d}{2x}\right) + \text{erf}\left(\frac{w_a + w_d}{2x}\right)\right], \tag{1.9}$$

where w_d is the designed width of the pattern while w_a is the actual width of the pattern after development, and erf(z) is the error function as defined in mathematics.

For the case of isolated features which consider only intra proximity effect, only one nonlinear equation for the exposure at the edge of a square or line is required to solve for the designed width of the square or line, i.e., w_d. For the case of interacting features which consider both intra proximity effect and inter proximity effect, a set of nonlinear equations for the exposure at different locations are required which are much more difficult in solving. For a simple case such as an infinitely long line adjacent to a large area, both the exposure at the left and right edge of the line are calculated to set up nonlinear equations to solve for the designed width of the line, i.e., w_d.

1.2.3 Distinctive PEC Techniques

Background Exposure Equalization Method

In 1983, Owen and Rissman developed a PEC method, GHOST, which does not suffer from the lengthy and costly computation required in the dose and shape modifications [19]. The correction scheme of GHOST is based on equalization of the background exposure, i.e., backscattered electron dose, received by all points within a pattern.

The pattern is first exposed (to generate a pattern exposure) using a focused beam with a dose D_e. Then the reverse field of the pattern is exposed (to generate a correction exposure) using a defocused electron beam with a diameter d_c:

$$d_c = \frac{\beta}{(1+\eta)^{1/4}}, \tag{1.10}$$

and a reduced dose D_c:

$$D_c = D_e \cdot \frac{\eta}{1+\eta}, \tag{1.11}$$

where β and η are as described in the double-Gaussian PSF (refer to Eq. 2.1).

By making a correction exposure in addition to the pattern exposure for equalizing the background exposure, the compensation for the proximity effect is achieved. As a result, all the features in the pattern will develop out in a more uniform manner in the resist development stage. Note that the implementation of GHOST only requires image reversal of the pattern data without any further computation.

Since the correction scheme of GHOST is simple and general enough to be implemented on any type of e-beam lithography systems, its application was further extended with various patterns and e-beam parameter settings [21, 30, 31, 34, 36, 37, 38, 54]. Watson et al. later improved GHOST by applying the pattern exposure and the correction exposure at the same time to eliminate the throughput drawback of the direct-write GHOST [58, 71].

Hierarchical Rule-based Method

In 1991, Lee et al. developed a PEC method, PYRAMID, which has a hierarchical rule-based correction scheme [41, 74, 75]. One of the most distinct features of PYRAMID is its two-level hierarchy in exposure estimation and correction, which is not restricted to either dose modification or shape modification. The first version and early improvements of PYRAMID adopted a shape modification for the correction part. However, there is nothing inherent in PYRAMID that requires shape modification, later the same overall correction hierarchy was extended to dose modification and hybrid (dose/shape) modification [69, 84, 87, 88].

Based on the digital image processing model of e-beam lithography, the exposure estimation of PYRAMID is implemented by calculating the total exposure as the sum of two separated components, global exposure and local exposure. The reason that the exposure

can be separated into two components stems directly from the fact that the PSF can be considered as consisting of the sum of two distinct components, i.e., a sharp, short range local component and a flat, long range global component. The global exposure is an approximation of the exposure due to circuit features located far away from the critical point and is calculated through a coarse grain convolution. The process of calculating global exposure begins by producing a coarse image of the circuit pattern by dividing it into large pixels or global exposure blocks, where the value of each block is the circuit area contained within the corresponding global exposure block in the circuit pattern. The global exposure can then be found by convolving the coarse image with a 2-D sampled version of the PSF, which has a sampling pixel size equal to the global exposure block size. The local exposure, as opposed to the global exposure, is exact and considers circuit area located close to the critical point. The local exposure at a given point is calculated by applying exact convolution to all circuit area falling within a small window centered about the global exposure block containing the point. This window is termed the local exposure window and serves to separate circuit area contributing to global exposure (area outside the window) from area contributing to local exposure (area inside the window).

Similarly, the correction procedure of PYRAMID is also divided into two parts, local correction and global correction. The local correction attempts to adjust the local dose distribution (for dose modification) or the pattern shape (for shape modification) to compensate for intra proximity effect and inter proximity effect caused by all the features within a small window. The local correction itself is very systematic, using two levels of correction to minimize intra proximity effect and inter proximity effect, respectively. Rule tables are used to dictate correction modes for different situations. Special consideration is given to correction of features which are in close proximity or connected at junctions. While the local correction ignores interactions between widely separated features, the global correction takes general characteristics of the entire circuit pattern into account to makes adjustments to the

local corrections based on differences in exposure values at various geometric locations in the circuit pattern.

Later, Lee et al. made various improvements to enhance the correction accuracy and efficiency of PYRAMID, including an extension of PYRAMID for circuit patterns of arbitrary size to allow the rectangles to be partitioned arbitrarily [45], an extension of PYRAMID for thicker resists which have a much greater proximity effect than do thinner resists [53], an efficient convolution method based on a table of cumulative distribution function values for the local exposure calculation [53], an interior area removal method by allowing PYRAMID to remove area from circuit features not only from the edges, but also from the interior as well [57], a region-wise correction method for heterogeneous substrates in which exposure estimation and correction are more complicated than in homogeneous substrates [65], an application of global exposure estimation and adjustment factor correction for reducing the recursive effect due to the sequential process adopted by PYRAMID [70], an adaptive method for selection of control points for high-density fine-feature circuit patterns [72], a distributed implementation of PYRAMID on a network of workstations which is highly scalable for realistic size of circuit patterns [78], a neural network based correction method for reducing the recursive effect by correcting circuit features in a group [81], a new format for hierarchical representation of circuit patterns which maintains compactness of data structure and allows efficient searching [85], a two-step hierarchical procedure for representation of nonrectangular features and four different methods for exposure estimation of nonrectangular features [89], etc.

1.2.4 Hybrid PEC Techniques

In order to achieve better correction accuracy and efficiency, several hybrid PEC methods have been proposed. In a hybrid PEC method, two or more independent PEC methods are usually contained, e.g., a combination of dose modification method and shape modification method.

In Groves's hybrid PEC method, the analytically determined shape modification method is adopted to offset forward scattering while the self-consistent dose modification method is adopted to offset backscattering [52].

Later, Cook and Lee developed a hybrid PEC method for PYRAMID [69]. In this hybrid PEC method, a circuit feature is partitioned into regions for region-wise dose control, where each region is assigned a different dose using the self-consistent dose modification method and the hierarchical rule-based shape modification method is carried out within each region.

Wind et al. developed a suite of PEC programs incorporating several dose modification methods, where the self-consistent dose modification method is used for forward-scattering correction and the pattern area density map dose modification method is used for backscattering correction [73].

Takahashi et al. separated the forward-scattering correction and the backscattering correction such that the analytically-determined shape modification method is used for the forward-scattering and is performed only once for repeated features while the pattern area density map dose modification method is used for backscattering correction and is iterated for reducing error [80, 83, 86].

Recently, Klimpel et al. developed a model-based hybrid PEC method, where the PSF (the proximity function) is modeled in different forms for the forward-scattering correction and the backscattering correction, respectively [102]. Based on this model, an iterative shape modification method is adopted for forward-scattering correction while an iterative dose modification method is adopted for backscattering correction.

1.2.5 Summary

In sum, most existed PEC techniques can be classified into two types: (1) Adjustment of incident electron dose, i.e., dose modification. This is achieved by appropriate variations in the dwell time or the beam intensity of a e-beam scanning system. (2) Adjustment of pattern dimensions, i.e., shape modification. This is achieved by appropriate changes in

the pattern dimensions such that patterns with the desired dimensions are obtained after exposure and development.

The dose modification PEC technique has the advantage that it provides a mathematically unique solution which depends only on the form and the magnitude of the PSF. This PEC technique is general enough to apply to an arbitrary definition of a region, from the smallest electron beam defined element to an entire shape. However, this PEC technique requires a lengthy and costly computation to evaluate the correction and a large database to store the dose value of each region. Furthermore, it cannot be applied on some certain kinds of e-beam lithography systems, such as the e-beam projection systems, which do not have the freedom of being able to change the dose for each shape as the pattern is being exposed.

The shape modification PEC technique has the advantage that it does not require sophisticated dose adjustment, thus is much more simple than the dose modification PEC technique. Also in the case of e-beam projection systems, the shape modification PEC technique is a better choice as it requires a relatively simple pattern generator in terms of not changing the beam frequency and a relatively simple computer programs for correcting pattern dimensions. The main disadvantage of this PEC technique is similar to the dose modification PEC technique, i.e., requiring a lengthy and costly computation to evaluate the correction. Its correction accuracy is lower than the dose modification PEC technique. Furthermore, the minimum magnitude of the shape changes is limited by the resolution of e-beam lithography systems.

Other PEC techniques, such as the GHOST method, has the advantage that it is simple and general enough to be implemented on any type of e-beam lithography systems and does not suffer from the time-consuming computation and large database storage required in the dose and shape modifications. The main disadvantage of this PEC technique is that the throughput of the lithographic process is reduced, typically by a factor of 2, due to compensating the proximity effect by a correction exposure. Another drawback is the

contrast degradation between the pattern exposure and the background exposure which leads to a dull resist profile.

1.3 Motivation and Objectives

From the above review, it is noticed that a typical approach to PEC employs a 2-D model of resist layer, i.e., the exposure variation along the resist depth dimension is not taken into account. In a 2-D PEC, the exposures at the selected points in a circuit pattern are estimated by convolution between a circuit pattern and a 2-D PSF, which is obtained by averaging the corresponding 3-D PSF along the resist depth dimension. The dose amount or shape adjustment for each circuit feature is determined such that a desired exposure distribution is achieved. Recently, there were claims of 3-D PEC being proposed [90, 98, 101]. However, they were claimed to be 3-D due to considering the thickness control of the resist profiles while still employed a 2-D exposure model.

For circuit patterns with nanoscale features, it is not unusual that the actual written pattern is substantially different from the written pattern estimated by a 2-D PEC method. One of the reasons for this deviation is that the 2-D model ignores the exposure variation along the resist depth dimension. In an earlier study [94], it was shown that the remaining resist profile estimated using a 2-D model can be significantly different from the one based on a 3-D model which considers the depth-dependent exposure variation. Another reason is that the actual resist profile cannot be derived directly from the exposure distribution, e.g., the developing rate is not linearly proportional to the exposure at a given point. Therefore, the PEC methods which consider the exposure only may suffer from substantial CD errors or deviation from the target resist profile in general. In addition, with a 2-D model, it is not possible to consider the lateral development of resist which affects the resist profile, in particular the sidewall shape, significantly.

Therefore, a 3-D PEC, which employs the resist profile estimation through simulation of resist development process instead of the exposure distribution, is required in order to obtain

more realistic results. It has been demonstrated that in order to minimize any deviation from a target resist profile, a 3-D PEC scheme must check the estimated resist profile during the dose optimization procedure [95]. One practical issue of such an approach to 3-D PEC is that a time-consuming resist development simulation needs to be carried out in each iteration of the dose optimization for each feature. For the case of large-scale patterns, such a feature-by-feature correction procedure would be too time-consuming to be practical. Also, it has been shown that the dose distribution of "V-shape", which is used by most 2-D PEC schemes, is not optimal for realizing a vertical sidewall of the resist profile, especially when the total dose is to be minimized. Note that a higher total dose worsens the charging effect and lengthens the exposing time.

The main objectives of this dissertation are:

- To develop a fast method for 3-D resist development simulation suitable to be employed in an iterative PEC scheme.
- To develop an accurate and efficient approach for estimation of remaining resist profiles for line/space patterns.
- To develop a practical and efficient 3-D PEC method for handling correction of large-scale uniform patterns.
- To derive new types of dose distributions for achieving the target resist profile of vertical sidewall for nanoscale features with the minimum total dose.
- To develop adaptive dose optimization and dose determination schemes for our 3-D PEC method.

1.4 Organization of Dissertation

The rest of this dissertation is organized as follows:

- Chapter 2 introduces the essential models in e-beam lithography and a fast path-based method for 3-D resist development simulation employed in this study.
- Chapter 3 describes an adaptive approach for estimation of remaining resist profiles for line/space patterns using a layer-based exposure model which does not require exposure computation and resist development simulation [103].
- Chapter 4 discusses a critical-location-based 3-D PEC method for correction of large-scale uniform patterns avoiding the intensive computation without sacrificing the correction quality [104].
- Chapter 5 describes two new types of dose distributions being derived under our 3-D exposure model and 3-D PEC method and two adaptive schemes for dose optimization and dose determination being developed for improving the correction efficiency without sacrificing the correction quality [105].
- Chapter 6 presents conclusions of this dissertation.

Chapter 2

Essential Models in Electron-beam Lithography

2.1 Electron-beam Lithography

E-beam lithography is a lithographic process used to transfer circuit patterns onto silicon or other substrates. It employs a focused beam of electrons to expose a circuit pattern into the electron-sensitive resist applied to the surface of the substrate. The main advantage of e-beam lithography is that it can offer much higher patterning resolution than the conventional optical lithography which is limited by the diffraction of light, thus it is extremely suitable for fabrication of nanoscale features.

A typical e-beam binary lithographic process is illustrated in Fig. 2.1. In the first step, the areas containing circuit features of a circuit pattern are exposed by the e-beam with different dose amounts, depositing energy in the resist (refer to Fig. 2.1(a)). After the exposing step, a solvent developer is used to selectively remove either the exposed regions or the unexposed regions of the resist depending on the type of resist (refer to Fig. 2.1(b)). For a positive resist, the most common type, the exposed regions become soluble in the developer, while the unexposed regions become soluble in the developer for a negative resist. After the resist development process, it can be seen that the substrate is covered by the undeveloped resist with different thickness. Finally, a corrosive etchant is applied to selectively etch the substrate, transferring the circuit pattern onto the substrate (refer to Fig. 2.1(c)). In this step, the remaining resist profile serves as a mask to control the etched depth.

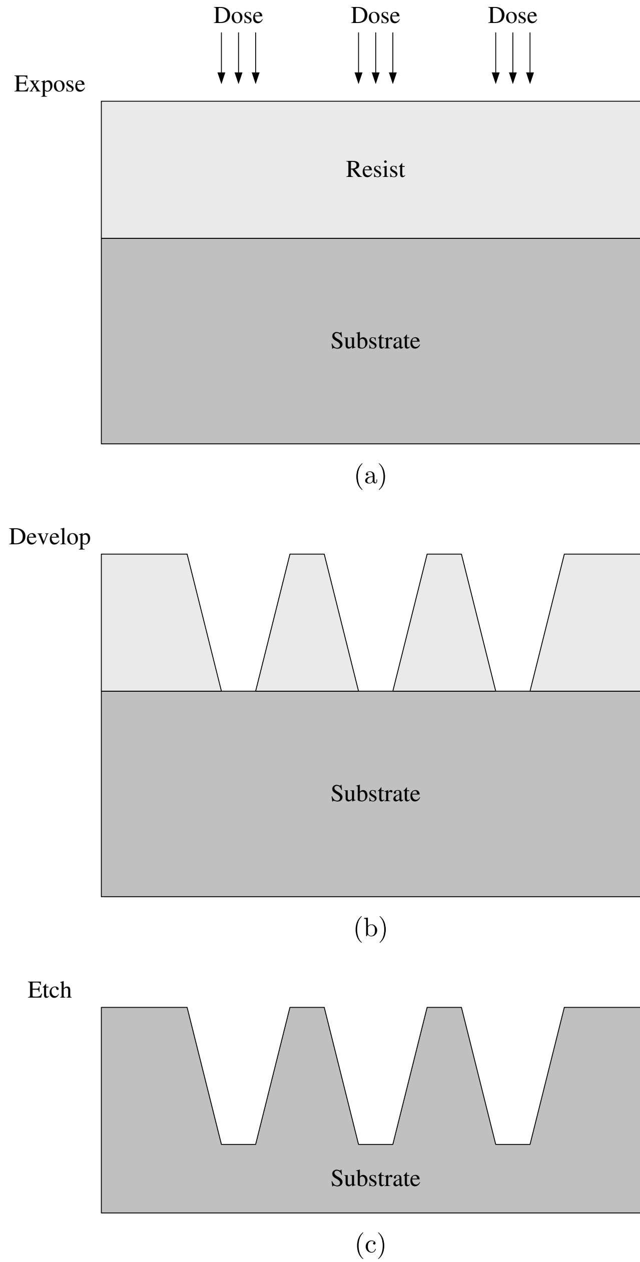

Figure 2.1: Illustration of the e-beam binary lithographic process.

2.2 Point Spread Function

The proximity effect in e-beam lithography is usually modeled by the convolution between the dose distribution of a circuit pattern and a proximity function or point spread function (PSF), which is radially symmetric and shows how the electron energy is distributed throughout the resist when a single point is exposed. Fig. 2.2 shows a typical PSF for the

substrate system of 300 nm PMMA on Si with the beam energy of 50 KeV, as a function of the distance from the exposed point.

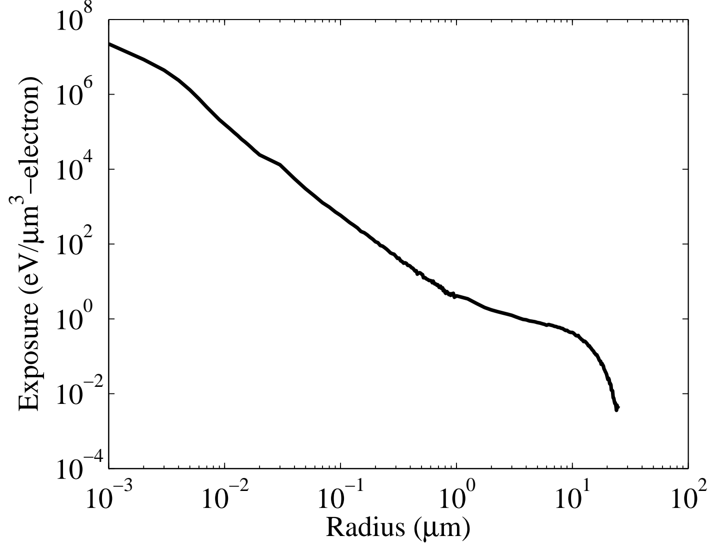

Figure 2.2: PSF for the substrate system of 300 nm PMMA on Si with the beam energy of 50 KeV.

In general, PSFs have the similar overall shape as illustrated in Fig. 2.2, which depends on resist thickness, substrate composition, beam energy, beam diameter, etc., and is independent of the dose given to the exposed point. One key property of the PSF is that it can be decomposed into two separate components, the local (or short range) component and the global (or long range) component. The local component, which has relatively large magnitude and is very sharp, describes the electron's forward scattering, while the global component, which has relatively low magnitude and is very flat, describes the electron's backward scattering.

One common way to model PSFs is through analytical approximation by a double-Gaussian function, which was proposed by Chang in 1975 [1], where one Gaussian function models the deposited energy due to the forward-scattering of electrons and the other Gaussian function models that due to the backscattering of electrons. The normalized double-Gaussian PSF is given by:

$$\text{psf}(r) = \frac{1}{\pi(1+\eta)}\left[\frac{1}{\alpha^2}\exp(\frac{-r^2}{\alpha^2}) + \frac{\eta}{\beta^2}\exp(\frac{-r^2}{\beta^2})\right], \tag{2.1}$$

where the parameter α represents the forward-scattering range, the parameter β represents the backscattering range, and the parameter η is the ratio of the backscattered energy level to the forward-scattered energy level.

Later more complicated forms of functions were proposed in order to enhance the accuracy of the Gaussian function fitting model, such as the triple-Gaussian function, the double Gaussian function plus an exponential term, etc [106, 107]. Furthermore, various methods for determination of the proximity effect parameters (α, β, and η) were developed [108, 109, 110, 112, 113, 116, 120].

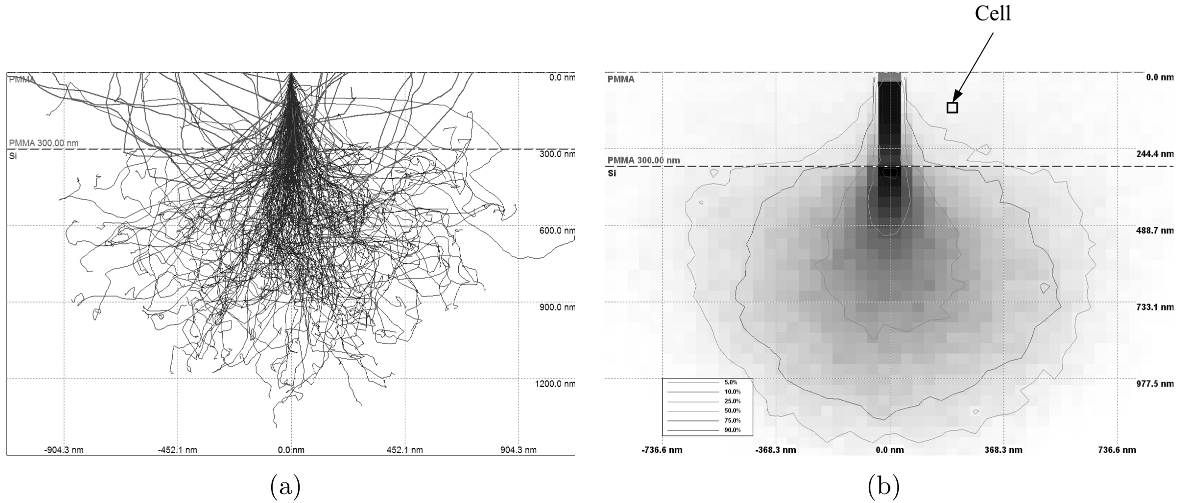

Figure 2.3: Monte Carlo simulation of (a) electron paths (cross-section) and (b) energy distribution (cross-section).

The Monte Carlo simulation is another widely used approach to deriving PSFs [111, 114, 115, 117, 121]. A substrate system including the resist layer is modeled as a 3-D array of cubic cells, and the random path of each individual electron is traced with the electron energy being deposited in the cells along the path which is stochastically determined based on the phenomena and effects theoretically modeled, as illustrated in Fig. 2.3(a). The final

electron energies deposited in the cells are computed along each path, to generate a 3-D PSF sampled at the interval of cell size, as illustrated in Fig. 2.3(b).

Recently, some researchers proposed experiment-based methods to generate much more realistic PSFs using experimental data, which are not constrained by a curve-fitting function and do not require a time-consuming simulation [118, 119].

2.3 Exposure Model

In a typical substrate system employed in this study, a resist layer with initial thickness of H is on top of the substrate, as illustrated in Fig. 2.4 where the X-Y plane corresponds to the top surface of resist and the resist depth is along the Z-dimension. The 3-D PSF is denoted by $\mathrm{psf}(x, y, z)$. Let $d(x, y, 0)$ represent the e-beam dose given to the point $(x, y, 0)$ on the surface of the resist for writing a circuit feature or pattern (refer to Fig. 2.4). For example, in the case of a uniform dose distribution,

$$d(x,y,0) = \begin{cases} D & \text{if } (x,y,0) \text{ is within a feature} \\ 0 & \text{otherwise} \end{cases}, \tag{2.2}$$

where D is a constant dose.

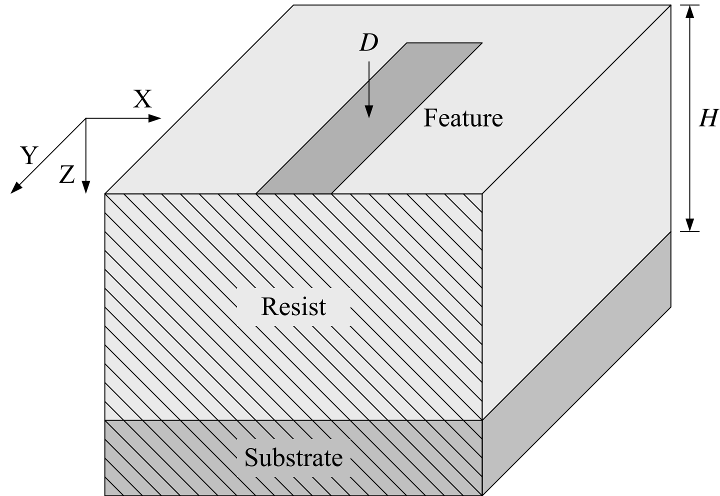

Figure 2.4: Illustration of the substrate system where H is the initial thickness of resist.

Let us denote the exposure at the point (x, y, z) in the resist by $e(x, y, z)$. Then, the 3-D spatial distribution of exposure can be expressed by the following convolution:

$$e(x, y, z) = \int\int d(x - x', y - y', 0)\text{psf}(x', y', z)dx'dy'. \tag{2.3}$$

From Eq. 2.3, it can be seen that the exposure distribution at a certain depth z_0 can be computed by the 2-D convolution between $d(x, y, 0)$ and $\text{psf}(x, y, z_0)$ in the corresponding plane $z = z_0$, i.e., $e(x, y, z)$ may be estimated layer by layer. Note that the PSF, $\text{psf}(x, y, z)$, reflects all the phenomena affecting energy deposition including the e-beam blur. The goal of PEC is to determine $d(x, y, 0)$ such that a target pattern is successfully transferred onto the resist layer.

2.4 Development Method

Although the 3-D exposure model provides the complete information on how electron energy is distributed in the resist, it does not directly depict the remaining resist profile after development, as illustrated in Fig. 2.5. Therefore, it is necessary to take the resist development process also into account in order to obtain a realistic correction result.

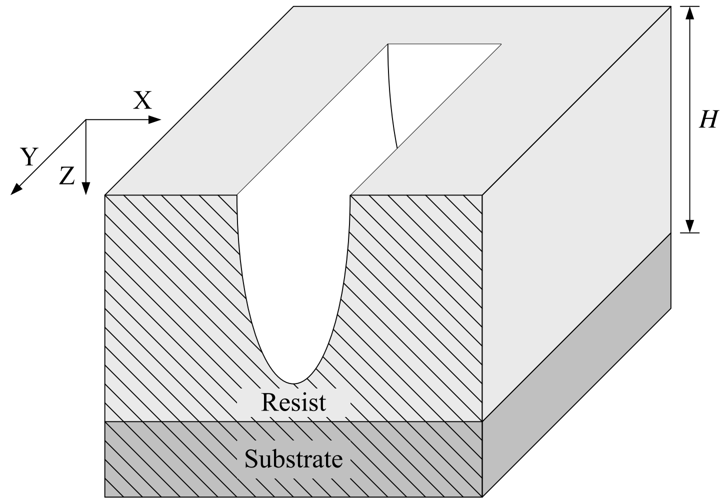

Figure 2.5: Illustration of the remaining resist profile after the resist development process.

2.4.1 Exposure-to-rate Conversion Formula

First, the developing rate at each point in the resist is computed based on the exposure at the point and developing conditions. Most resists are nonlinear in nature when exposed by the e-beam, i.e., the developing rate is not linearly proportional to the exposure. Therefore, the developing rate $r(x, y, z)$ at each point in the resist is calculated from its corresponding exposure $e(x, y, z)$ through a nonlinear exposure-to-rate conversion formula, which is obtained experimentally.

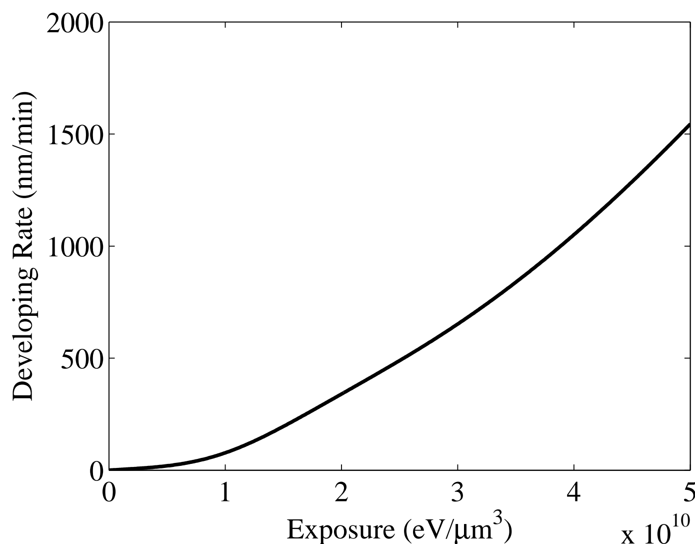

Figure 2.6: The experiment-based nonlinear exposure-to-rate conversion formula.

A long line with width of 100 nm is exposed with various dose levels. After resist development, the center depth is measured in the cross-section of remaining resist profile obtained for each dose level. Note that the resist is developed only vertically at the center of line when the dose distribution within the line is uniform. The center depth is also obtained for each dose level through simulation based on our 3-D exposure model. By comparing the two sets of depth measurements obtained experimentally and via simulation, the following conversion formula has been derived (also refer to Fig. 2.6):

$$r(x,y,z) = F[e(x,y,z)] = 3700 \cdot e^{-(\frac{e(x,y,z)-1.0e11}{5.6e10})^2} - 80 \cdot e^{-(\frac{e(x,y,z)-9.0e9}{9.0e9})^2} - 123, \tag{2.4}$$

where $r(x, y, z)$ is in nm/minute and $e(x, y, z)$ in $eV/\mu m^2$.

2.4.2 Cell Removal Method

Then, a development method is employed to derive the remaining resist profile. In the past, several 2-D and 3-D methods were developed, such as the the string method, the ray-tracing method, and the cell removal method. The string and ray-tracing methods usually have difficulties in the treatment of boundaries and the elimination of loops. In contrast, the cell removal method, e.g., PEACE [122], is quite stable and robust as it does not suffer from such problems.

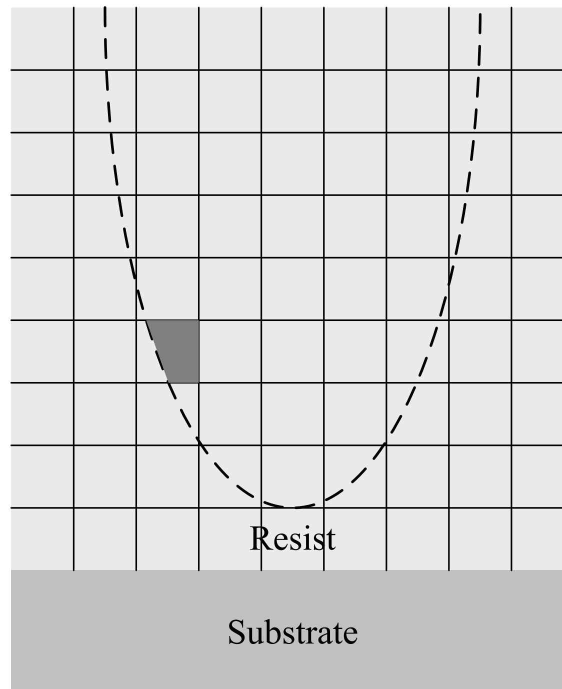

Figure 2.7: Illustration of the cell removal method where the dashed curve represents a cross-section of resist profile.

In this method, each resist layer is partitioned into cubic cells, and the resist development process is traced on a cell-by-cell basis (refer to Fig. 2.7). This kind of cell-based method is generally easy to implement which makes it widely used. However, the main drawback of the cell removal method is a long computation time required, specially for estimating 3-D resist profiles. When an iterative PEC scheme requires the resist development simulation in each iteration, it would not be practical to employ such a time-consuming method.

2.4.3 Proposed Path-based Method

In this study, a fast path-based method for 3-D resist development simulation which avoids the time-consuming computation without sacrificing the simulation accuracy has been proposed. The proposed method employs the concept of "development paths", which start from the top surface of resist toward the boundaries of the final resist profile, to model the development process.

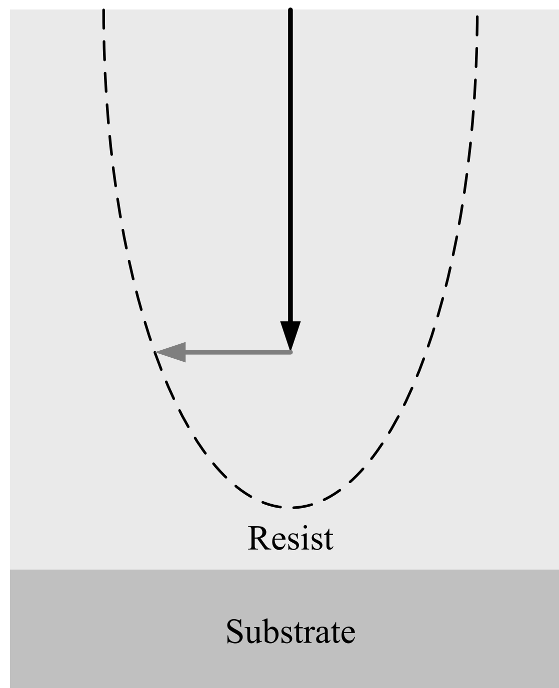

Figure 2.8: Illustration of the path-based method where the dashed curve represents a cross-section of resist profile.

Conventionally, one should model the development process in an isotropic way as the resist is developed in all possible directions in reality. However, in the proposed method, the development process is simply modeled as two separate parts, i.e., vertical development and lateral development. Similarly, each path is also modeled as consisting of two orthogonal types of path segments, i.e., vertical (to depict vertical development) and lateral (to depict lateral development) path segments (refer to Fig. 2.8). More specifically, each path has one and only one vertical path segment (along the Z-dimension) and may have one or more lateral path segments (along the X-dimension or Y-dimension).

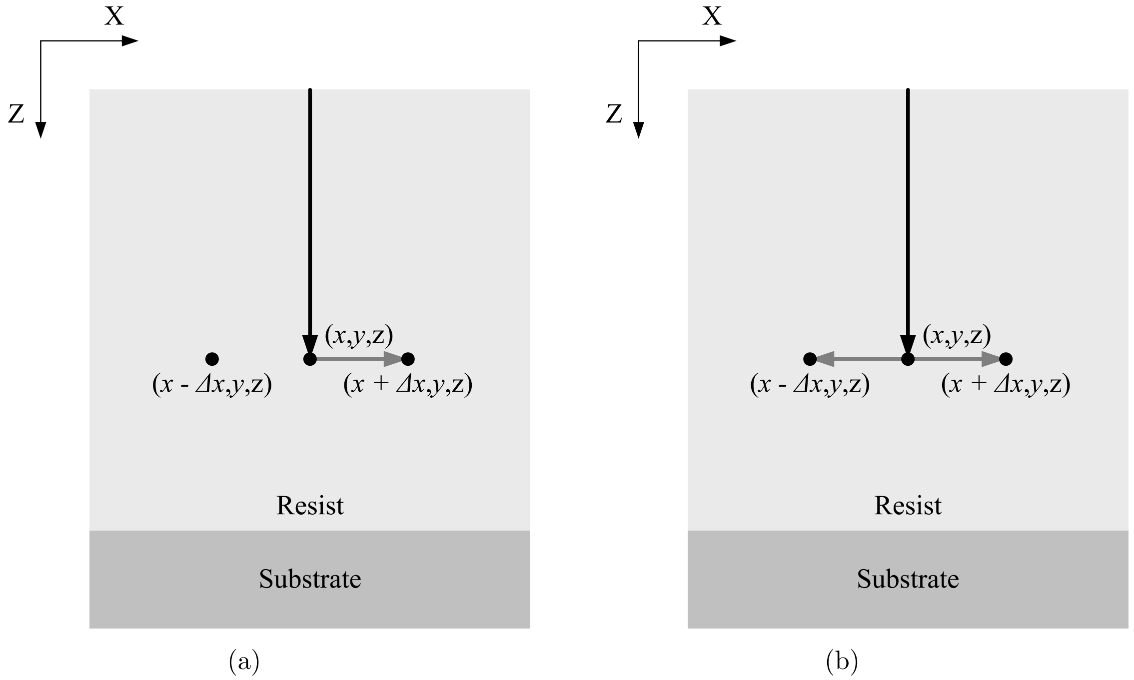

Figure 2.9: A path turns to (a) only the positive direction of the X-axis at the point (x, y, z) if $r(x, y, z) > r(x + \Delta x, y, z)$ but $r(x, y, z) \leq r(x - \Delta x, y, z)$ and (b) both the positive and negative directions of the X-axis at the point (x, y, z) if $r(x, y, z) > r(x + \Delta x, y, z)$ and $r(x, y, z) > r(x - \Delta x, y, z)$.

In order to model the resist profile in a more accurately way, the concept of "turns" is employed to compute each path based on its path segments. A path makes a turn when it switches from one vertical path segment to one lateral path segment or one lateral path segment to another lateral path segment. Whether and in what direction a path is to be turned at a point depends on the relative developing rates of adjacent points in X-Y plane

compared to that of the point. This is based on the fact that the developer passes a point with relatively higher developing rate faster than its adjacent points with relatively lower developing rates, then the developer will keep developing laterally toward those adjacent points. It is obvious that a larger lateral development takes place when there is a larger difference between the developing rates of adjacent points.

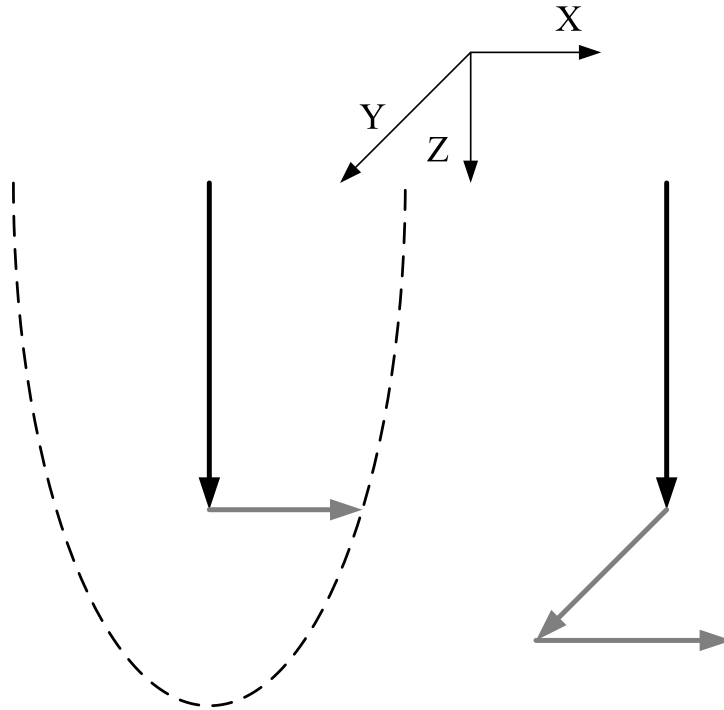

Figure 2.10: The development paths with one and two turns where the black and gray lines are the vertical and lateral path segments, respectively, and the dashed curve represents a cross-section of resist profile. The Z-axis corresponds to the resist depth dimension.

Let the distances between adjacent points in the X-dimension, Y-dimension, and Z-dimension be denoted by Δx, Δy, and Δz, respectively. A turn is allowed only from one point (x, y, z) with relatively higher developing rate to its adjacent points with relatively lower developing rates, i.e., $r(x, y, z) > r(x + \Delta x, y, z)$ or $r(x, y, z) > r(x - \Delta x, y, z)$ or $r(x, y, z) > r(x, y + \Delta y, z)$ or $r(x, y, z) > r(x, y - \Delta y, z)$. For example, a path turns to only the positive direction of the X-axis at the point (x, y, z) if $r(x, y, z) > r(x + \Delta x, y, z)$ but $r(x, y, z) \leq r(x - \Delta x, y, z)$, as illustrated in Fig. 2.9(a), while it turns to both the positive

and negative directions of the X-axis at the same point if $r(x, y, z) > r(x + \Delta x, y, z)$ and $r(x, y, z) > r(x - \Delta x, y, z)$, as illustrated in Fig. 2.9(b).

It is obvious that the more turns allowed, the more accurate the simulation result becomes, but the longer the simulation time is. It is found that in many cases, one turn is sufficient to achieve high accuracy of simulation, e.g., when one is interested only in cross-sections of resist profile for a line feature. Even for more general shapes of feature, two turns are sufficient to obtain accurate 3-D resist profiles at the expense of a longer simulation time compared to the case where only one turn is allowed (refer to Fig. 2.10).

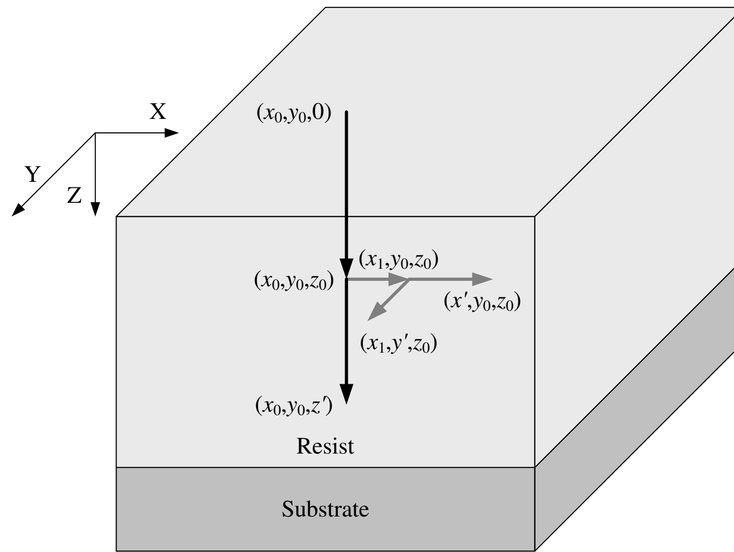

Figure 2.11: The computation of each path terminates when the sum of the time spent on its path segments is equal to the given developing time T.

The computation of each path terminates when the sum of the time spent on its path segments is equal to the given developing time T, which is given by (refer to Fig. 2.11):

$$\sum_{z=0}^{z'} \frac{\Delta z}{r(x_0, y_0, z)} = T, \tag{2.5}$$

for no-turn (vertical-only) paths,

$$\sum_{z=0}^{z_0} \frac{\Delta z}{r(x_0, y_0, z)} + \sum_{x=x_0}^{x'} \frac{\Delta x}{r(x, y_0, z_0)} = T, \tag{2.6}$$

for one-turn paths, and

$$\sum_{z=0}^{z_0} \frac{\Delta z}{r(x_0, y_0, z)} + \sum_{x=x_0}^{x_1} \frac{\Delta x}{r(x, y_0, z_0)} + \sum_{y=y_0}^{y'} \frac{\Delta y}{r(x_1, y, z_0)} = T, \tag{2.7}$$

for two-turn paths, respectively.

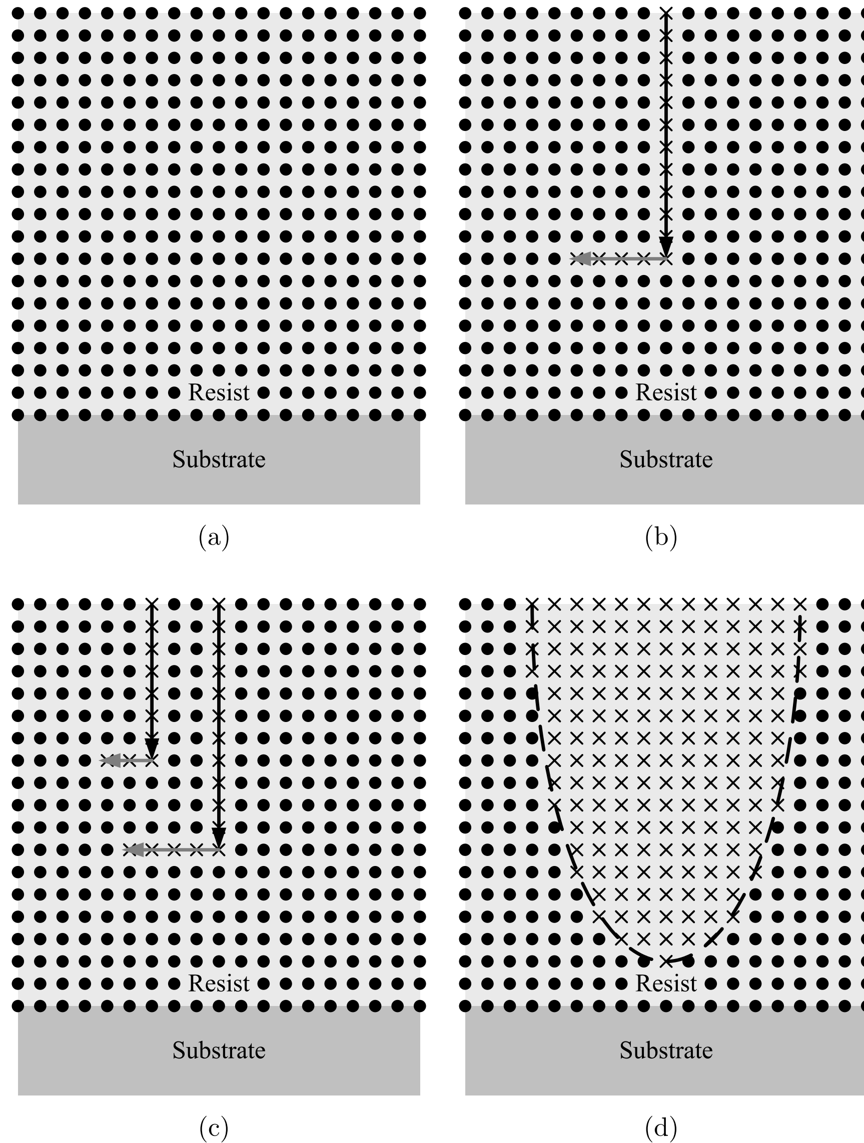

Figure 2.12: (a) All the points in the resist are marked as “undeveloped” before the resist development simulation. (b) After one path is computed, the points which it passes through are marked as “developed”. (c) After another path is computed, more points are marked as “developed”. (d) The final resist profile is determined by tracing the boundaries between those developed points and those which are not.

In order to derive the final resist profile, a mark is used to represent the status of each point during the resist development simulation. Initially, all the points in the resist are marked as "undeveloped". Then, after one path is computed, the points which it passes through are marked as "developed". It is obvious that more and more points are marked as "developed" as more and more paths are computed. The final resist profile is determined by tracing the boundaries between those developed points and those which are not (refer to Fig. 2.12).

The complete procedure of the path-based method is depicted below (also refer to the flowchart in Fig. 2.13).

Step 1: Compute the exposure distribution $e(x, y, z)$, and convert it into the developing rate distribution $r(x, y, z)$ through the conversion formula $F[\cdot]$ in Eq. 2.4.

Step 2: Compute a vertical path segment along the Z-dimension starting from a specific point $(x_0, y_0, 0)$ on the top surface of resist using the developing rate distribution $r(x, y, z)$ and the given developing time T, such that $\sum_{z=0}^{z'} \frac{\Delta z}{r(x_0, y_0, z)} = T$.

Step 3: Compute a lateral path segment along the X-dimension starting from a specific point (x_0, y_0, z_0) $(0 < z_0 < z')$ on the vertical path segment in Step 2 (if $r(x_0, y_0, z_0) > r(x_0 + \Delta x, y_0, z_0)$ or $r(x_0, y_0, z_0) > r(x_0 - \Delta x, y_0, z_0)$) using the developing rate distribution $r(x, y, z)$ and the given developing time T, such that $\sum_{z=0}^{z_0} \frac{\Delta z}{r(x_0, y_0, z)} + \sum_{x=x_0}^{x'} \frac{\Delta x}{r(x, y_0, z_0)} = T$.

Step 4: Compute a lateral path segment along the Y-dimension starting from a specific point (x_1, y_0, z_0) $(x_0 < x_1 < x')$ on the lateral path segment in Step 3 (if $r(x_1, y_0, z_0) > r(x_1, y_0 + \Delta y, z_0)$ or $r(x_1, y_0, z_0) > r(x_1, y_0 - \Delta y, z_0)$) using the developing rate distribution $r(x, y, z)$ and the given developing time T, such that $\sum_{z=0}^{z_0} \frac{\Delta z}{r(x_0, y_0, z)} + \sum_{x=x_0}^{x_1} \frac{\Delta x}{r(x, y_0, z_0)} + \sum_{y=y_0}^{y'} \frac{\Delta y}{r(x_1, y, z_0)} = T$.

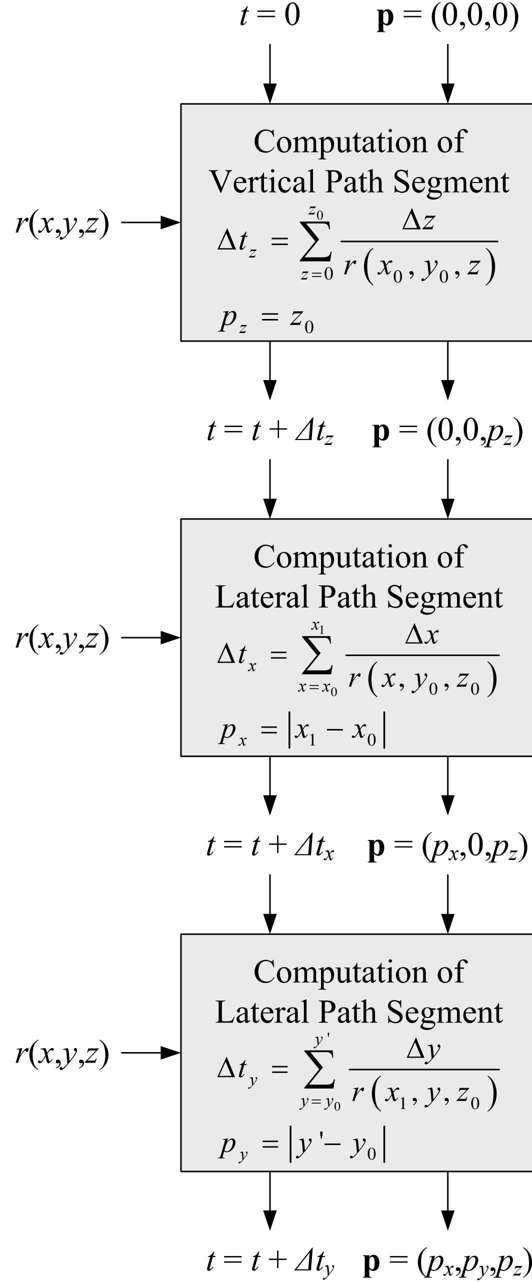

Figure 2.13: Flowchart of the computation of a two-turn path, where Δt_x, Δt_y, and Δt_z ($\Delta t_x + \Delta t_y + \Delta t_z = T$) are the time spent on the path segment in the X-dimension, Y-dimension, and Z-dimension, respectively, and $\mathbf{p}$ is the vector representation of the path in the 3-D space.

Step 5: Store the vector representation of the path in the 3-D space (considering all the above three path segments) as $\mathbf{p} = (p_x, p_y, p_z)$, where $p_x = |x_1 - x_0|$, $p_y = |y' - y_0|$, and $p_z = z_0$ are the three path segments, respectively.

Step 6: Mark the points which the path passes through as "developed" using $\mathbf{p} = (p_x, p_y, p_z)$.

Step 7: If all the possible paths are computed, proceed to Step 8. Otherwise, go back to Step 2.

Step 8: Determine the final resist profile by tracing the boundaries between those developed points and those which are not.

It can be seen that compared with the cell removal method which employs a time-consuming iterative procedure to update the status of each cell, the proposed method is more straightforward as it does not require any iterations in computing each path. Furthermore, the simulation of each cell is correlated in the cell removal method, which means that the final status (the portion being developed) of each cell cannot be determined until all the cells are simulated. However, each path is computed individually in the proposed method, thus avoids this kind of issue and reduces the simulation time.

In order to minimize the simulation time, an adaptive approach is incorporated into the simulation procedure. Before the final stage of simulation, the resist profile would be usually smooth without sharp shapes such as corners and junctions. Therefore, a developing period (time) is partitioned into two phases where only one turn is allowed in the first phase and two turns in the second phase. This adaptive approach reduces the simulation time greatly without sacrificing simulation accuracy substantially.

2.4.4 Results and Discussion

The proposed path-based method for 3-D resist development simulation has been implemented and its performance has been compared with the cell removal method in terms of simulation accuracy and time. Eight different test patterns (Patterns I-VIII) including Pattern I (shown in Fig. 2.14(a)) and Pattern II (shown in Fig. 2.14(b)) are considered in the comparison. The largest pattern size for simulation is 1 μm by 1 μm.

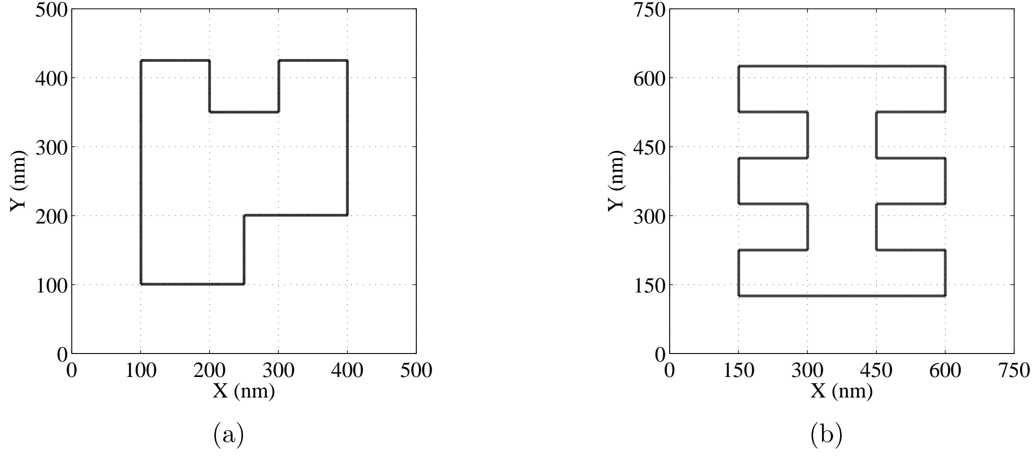

Figure 2.14: The layout of (a) Pattern I and (b) Pattern II.

The PSFs employed in the simulation are generated by a Monte Carlo simulation method, SEEL [111]. The substrate system assumed in this comparison is composed of 300 nm PMMA on Si. The beam energy is set to 50 KeV with the beam diameter of 5 nm. The developing time is 40 sec.

The resist profiles simulated by the proposed path-based method are compared with those simulated by the cell removal method with the constraint that the resolution of the resist profile is the same for both methods. The contours of resist profiles at the top, middle and bottom layers, obtained for Pattern I and Pattern II, are provided in Fig. 2.15 and Fig. 2.16.

By comparing the above resist profiles, it can be seen that the resist profiles by the proposed method are well matched with those by the cell removal method. The profile difference between the two methods is provided in Table 2.1. The same high accuracy is observed in all of the other test patterns.

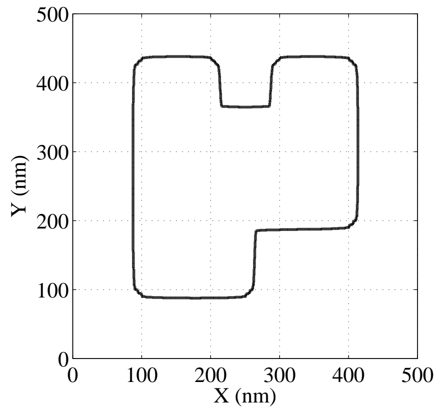

(a)

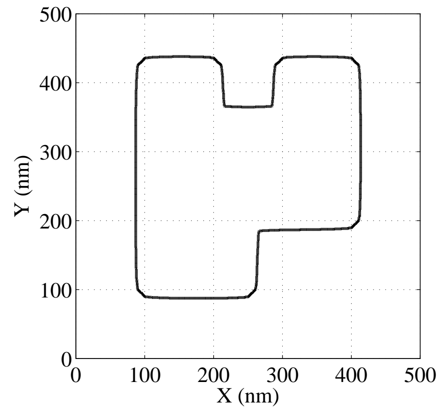

(b)

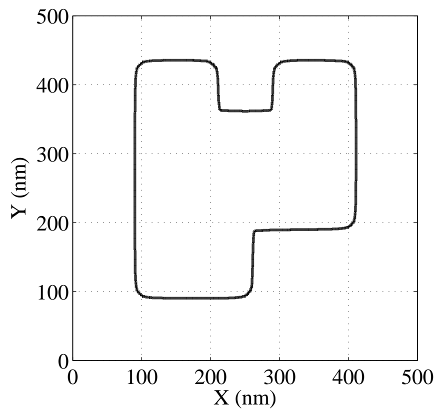

(c)

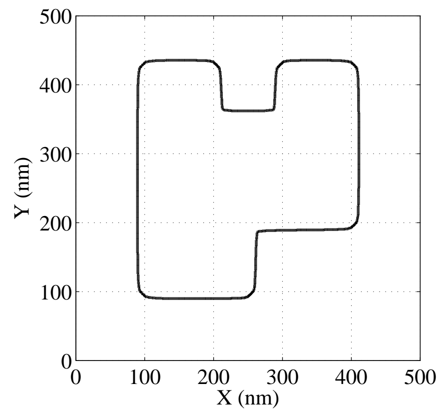

(d)

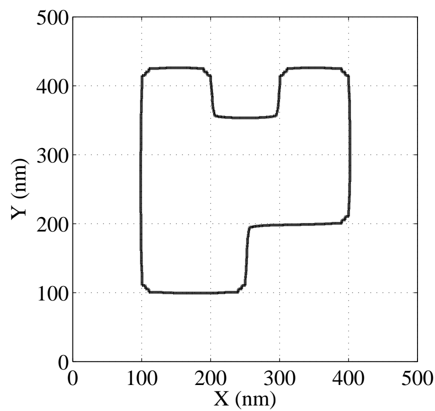

(e)

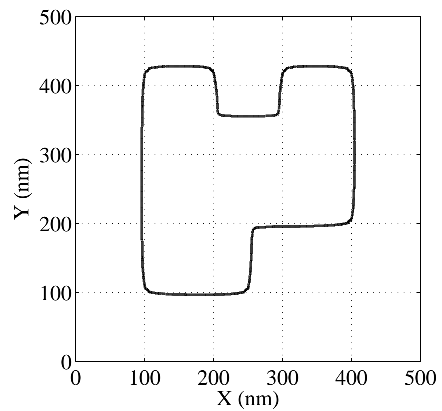

(f)

Figure 2.15: Contours (top view) of resist profiles for Pattern I at the (a) top, (c) middle, and (e) bottom layers of resist by the cell removal method, and at the (b) top, (d) middle, and (f) bottom layers of resist by the path-based method.

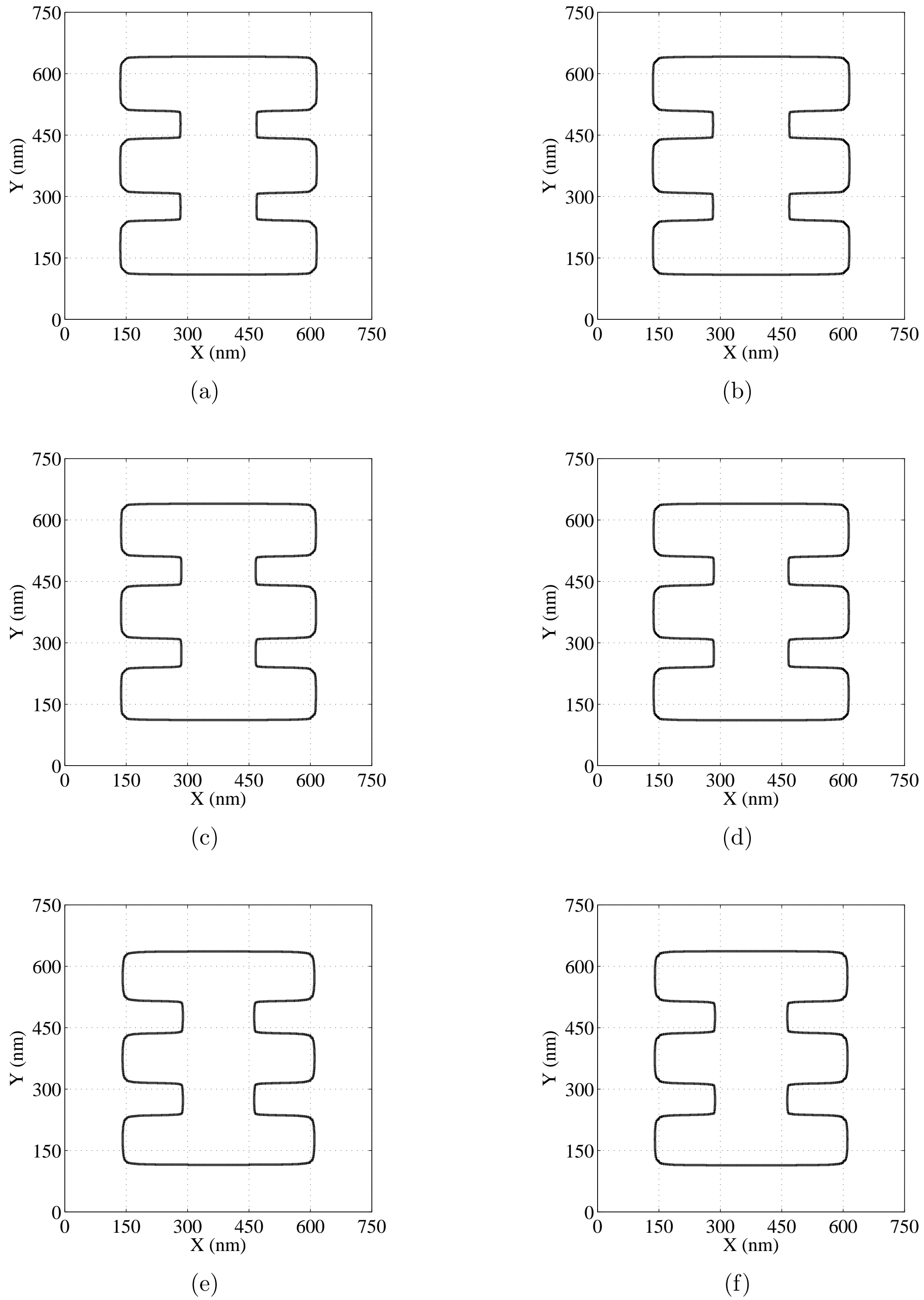

Figure 2.16: Contours (top view) of resist profiles for Pattern II at the (a) top, (c) middle, and (e) bottom layers of resist by the cell removal method, and at the (b) top, (d) middle, and (f) bottom layers of resist by the path-based method.

Pattern		Profile Difference		
ID	Size (nm × nm)	Top (%)	Middle (%)	Bottom (%)
I	500 × 500	0.45	0.53	1.19
II	750 × 750	0.42	0.49	1.54
III	1000 × 1000	0.48	0.78	2.89
IV	150 × 1000	0.70	0.78	3.37
V	250 × 1000	0.70	0.84	2.94
VI	350 × 1000	0.69	1.00	3.28
VII	450 × 1000	0.69	0.95	3.08
VIII	550 × 1000	0.69	1.04	2.41

Table 2.1: Profile difference between the cell removal method and the path-based method.

Pattern		Cell Removal	Path-based Method (sec)		
ID	Size (nm × nm)	Method (sec)	One-Turn	Two-Turn	Adaptive
I	500 × 500	403.86	6.96	32.52	18.73
II	750 × 750	1869.36	19.09	64.55	53.58
III	1000 × 1000	5332.55	27.01	116.07	88.97
IV	150 × 1000	160.72	4.89	19.50	12.21
V	250 × 1000	594.32	10.92	39.48	24.94
VI	350 × 1000	1050.71	13.92	59.99	38.56
VII	450 × 1000	1902.56	20.03	84.31	52.30
VIII	550 × 1000	2744.31	22.48	101.25	66.04

Table 2.2: Simulation time of the cell removal method and the path-based method.

Pattern		Speedup		
ID	Size (nm × nm)	One-Turn	Two-Turn	Adaptive
I	500 × 500	58.03	12.42	21.56
II	750 × 750	97.92	28.96	34.89
III	1000 × 1000	197.43	45.94	59.93
IV	150 × 1000	32.82	8.24	13.16
V	250 × 1000	54.42	15.05	23.83
VI	350 × 1000	75.48	17.51	27.25
VII	450 × 1000	94.99	22.57	36.38
VIII	550 × 1000	122.08	27.11	41.56

Table 2.3: Speedup of the path-based method to the cell removal method.

In Table 2.2, the simulation time measured on a PC with a 2.53 GHz CPU (Intel Core i5-540M) and 2 GB memory is provided for the test patterns. It is clear that the proposed

method takes much less time for simulation, compared to the cell removal method. Note that the simulation time of the cell removal method with respect to the pattern size is close to a quadratic relationship while that of the proposed method is almost linearly proportional to the pattern size. From Table 2.3, it can be seen that the speedup of the proposed method to the cell removal method increases significantly for larger patterns. Therefore, the proposed path-based method has a good potential to be a practical and efficient alternative to the existing methods such as the time-consuming cell removal method.

Chapter 3

Estimation of Resist Profile for Line/Space Patterns

3.1 Introduction

The e-beam lithographic process consists of selectively exposing resist by e-beam and subsequently developing the resist for pattern transfer. For applications such as predicting the remaining resist profile (just resist profile hereafter) in grayscale lithography and PEC, both steps are often simulated. In the first step, the exposure distribution is computed by convolution between a circuit pattern and a PSF. In the second step, the developing rate at each point in the resist is computed based on the exposure at the point and developing conditions, and a development method is employed to derive the remaining resist profile.

While such simulations are widely used, it is not unusual that the estimated profile of the remaining resist is substantially different from the actual profile obtained in experiment. The reasons for this deviation may include (i) the actual parameters such as beam diameter are different from those in the system specifications, (ii) certain effects may not be considered in simulation, and (iii) the actual remaining resist profile varies with the developing condition. Also, such simulations are very time-consuming. Hence, it is worthwhile to develop a new method which does not require exposure calculation and development simulation, in order to provide an alternative to the conventional simulation-based methods.

Resist profiles obtained in experiments reflect all effects and actual parameters involved in the e-beam lithographic process. Therefore, an experiment-based method has a potential to generate an estimated profile close to the actual one. A new method is proposed for estimating the resist profiles using a set of experimental results without exposure estimation and development simulation. This new method should be distinguished from the conventional approaches, where exposure distribution and/or resist profile is obtained through simulation.

The idea of the method is to adopt the concept of "base patterns." The resist profiles of the base patterns are obtained through experiments and are used in estimating the resist profile of a given pattern consisting of the base patterns. In this chapter, an implementation of the method which utilizes the base pattern of line to estimate resist profiles of line/space patterns is presented to demonstrate the feasibility of the method through computer simulation and experiments.

The rest of the chapter is organized as follows. The conventional estimation approach is briefly reviewed in Section 3.2. The proposed estimation approach is described in Section 3.3. Details of the estimation procedure are presented in Section 3.4. Simulation and experimental results are discussed in Section 3.5, followed by a summary in Section 3.6.

3.2 Conventional Estimation Approach

A conventional estimation approach is to compute the exposure distribution for a target pattern through convolution with the PSF and then to obtain the resist profile via simulation of development process based on the exposure distribution (refer to Section 2.3 and Section 2.4). Fig. 3.1 shows this approach being applied on a three-line pattern. It can be seen that the estimated profile of the remaining resist from this approach is completely dependent on the accuracy of the PSF which is usually obtained through modeling or simulation (refer to Section 2.2). Furthermore, this approach requires a tremendous amount of simulation time for patterns containing a large number of lines which is common in practical applications.

3.3 Proposed Estimation Approach

3.3.1 Base Patterns

The proposed estimation method is based on the approach where a minimal set of experiments is carried out in order to extract a minimally sufficient amount of information on the resist development process in a certain experimental set-up. The patterns employed in these experiments are referred to as base patterns, which are long rectangles in this study.

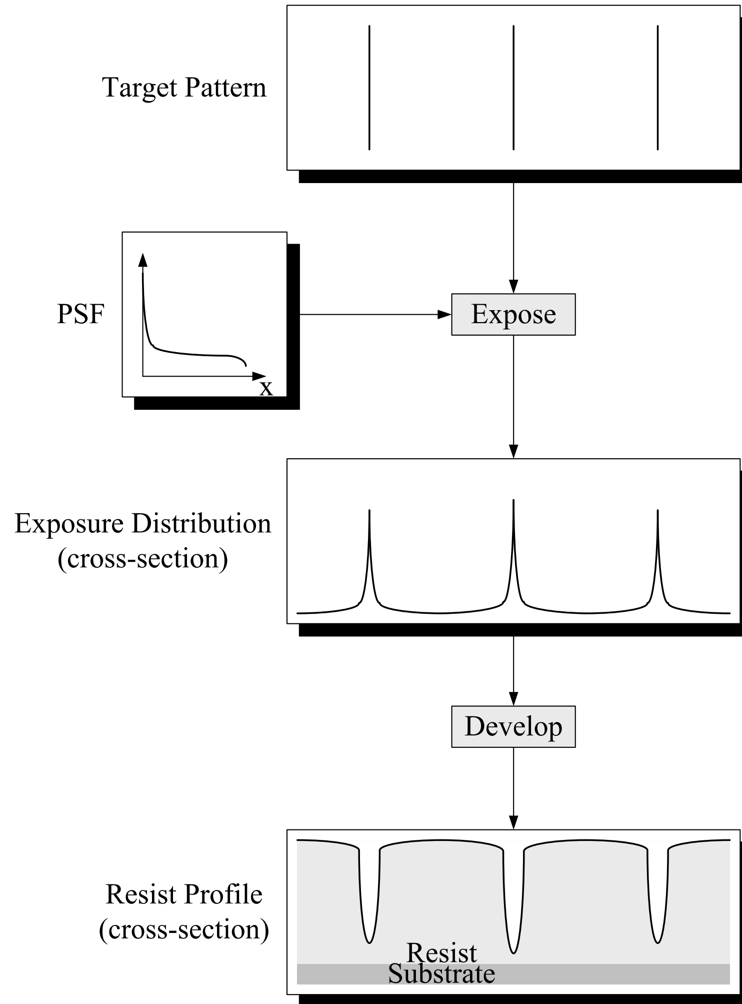

Figure 3.1: Illustration of the conventional estimation approach where both exposing step and developing step are simulated.

Through these experiments, the dose and width of rectangle are varied to collect the data needed for estimation of the remaining resist profile of a target pattern. The more data are collected, the more accurate estimation is possible. However, the number of experiments is to be minimized from the viewpoint of practicality. Therefore, it is required to sample a limited number of base patterns to collect enough data for the estimation.

It is assumed that a base pattern is sufficiently long along the Y-dimension such that any variation along the Y-dimension can be ignored, or only the cross-section of resist perpendicular to the Y-dimension is considered (refer to Fig. 3.2). In the cross-section, $e(x, y, z)$ and $r(x, y, z)$ are replaced by $e(x, z)$ and $r(x, z)$, respectively.

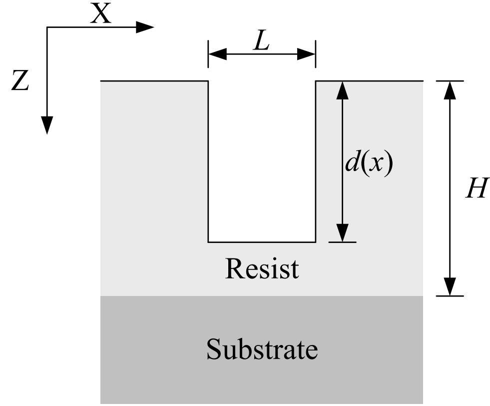

Figure 3.2: Cross-section of the resist profile of a base pattern.

3.3.2 2-D Exposure Model

In an earlier effort, a method which takes the above-mentioned (refer to Section 3.3.1) approach to estimation of remaining resist profiles was developed, but based on a 2-D exposure model. This method, referred to as "2-D Mod," is briefly described below, to be compared to the proposed method. In the 2-D exposure model, exposure is assumed not to change along the resist depth dimension (Z-dimension), i.e., $e(x, z)$ in the cross-section is averaged over $0 \leq z \leq H$ (see Fig. 2.4), resulting in $e(x)$.

Suppose that the target pattern consists of two identical lines and the center-to-center distance between the two lines is I. The base pattern for estimating the resist profile of the target pattern is a single line. Let the resist (depth) profile of the base pattern be represented by $d_1(x)$. The resist profile of the target pattern, $d_2(x)$, is estimated from $d_1(x)$ as follows. The developing rate is estimated as $r_1(x) = \frac{d_1(x)}{T}$ where T is the developing time, and the exposure distribution for the base pattern is computed by $e_1(x) = F^{-1}[r_1(x)]$ (refer to Eq. 2.4). Then, noting the linearity of exposure, the developing rate distribution for the target pattern can be obtained as:

$$r_2(x) = F[e_2(x)] = F[e_1(x) + e_1(x - I)]. \tag{3.1}$$

Finally, the resist profile of the target pattern is estimated to be:

$$d_2(x) = r_2(x) \cdot T. \tag{3.2}$$

A fundamental problem of this method is that the exposure variation along the resist depth dimension is not taken into account, which can lead to a significant estimation error [94, 95, 96]. Furthermore, the nonlinear mapping $F[\cdot]$ makes the error even larger, as illustrated in Fig. 3.3. Also, the lateral development of resist is not explicitly considered in the estimation procedure though $d_1(x)$ itself includes the lateral component of resist development. Therefore, in this chapter, an estimation method which employs a 3-D exposure model and explicitly accounts for lateral development is presented.

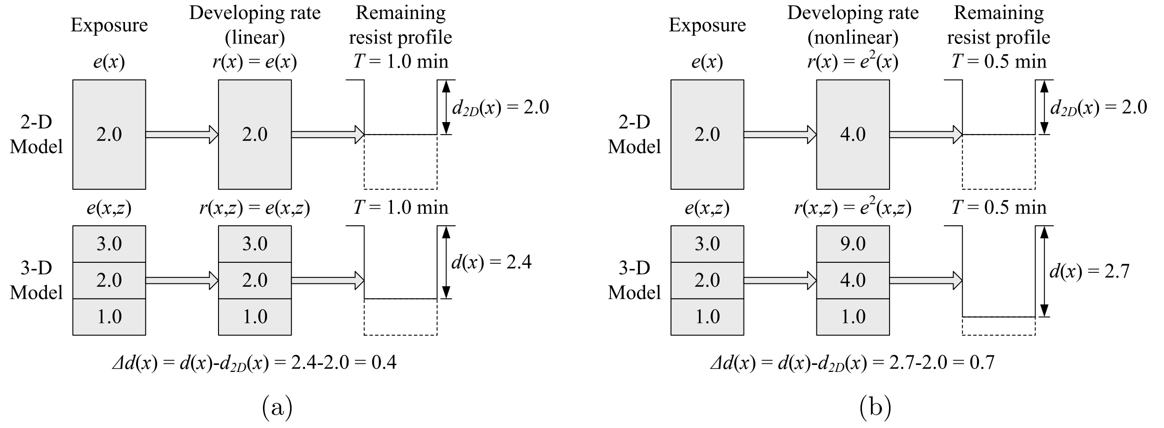

Figure 3.3: Difference in estimation of remaining resist profiles between 2-D model and 3-D model through (a) linear mapping ($r = e$) and (b) nonlinear mapping ($r = e^2$).

3.3.3 Layer-based Exposure Model

In this study, a new method which adopts the idea of layer-based exposure modeling has been developed in order to improve estimation accuracy. By analyzing the simulation results for several base patterns on different substrate systems, it is shown that the distribution of $e(x_i, z)$ with respect to z is similar to that of $e(x_j, z)$, where x_i and x_j are any two points within the exposed area, as shown in Fig. 3.4(a). Therefore, $e(x, z)$ can be modeled using a family of normalized decreasing functions with parameters including the resist thickness, the feature size (width of exposed area), and the distance from x to the center of a feature.

In this way, given a certain point x_0 within the feature, a normalized distribution curve of $e(x_0, z)$ can be modeled, which is denoted by $N(x_0, z)$. The actual values of $e(x_0, z)$ can be computed by:

$$e(x_0, z) = e(x_0) \cdot N(x_0, z), \tag{3.3}$$

where $e(x_0)$ is initiated by:

$$e(x_0) = F^{-1}[r(x_0)] = F^{-1}[\frac{d(x_0)}{T}]. \tag{3.4}$$

Then, for the developing time T, the estimated depth $d'(x_0)$ may be determined by:

$$\int_0^{d'(x_0)/d_0} \frac{d_0}{F[e(x_0, z)]} dz = T, \tag{3.5}$$

where d_0 is the thickness of each layer of the resist defined in the model. A smaller d_0 leads to a higher estimation accuracy.

Up to now a percentage depth error is derived by:

$$\Delta d(x_0) = \frac{d'(x_0) - d(x_0)}{d(x_0)}. \tag{3.6}$$

This error is used for controlling the increment of $r(x_0)$, or equivalently $e(x_0)$ to re-compute $e(x_0, z)$ until the error converges. Through this kind of iteration, $e(x_0, z)$ can be modeled accurately enough to avoid either underestimation or overestimation.

From the analysis of 3-D exposure distribution, it is also found that the distribution of $e(x, z)$ along the Z-dimension changes abruptly when crossing the boundary between the exposed and unexposed areas without a gradual transition region. The $e(x, z)'s$ for different x in the unexposed area are different from those in the exposed area, but similar among themselves, as shown in Fig. 3.4(b). Therefore, the same approach to modeling $e(x, z)$ (as the one described above for the exposed area) can be taken also for the points in the

unexposed area, i.e., outside features. This layer-based modeling is essential to the proposed estimation method, and is proved to be effective.

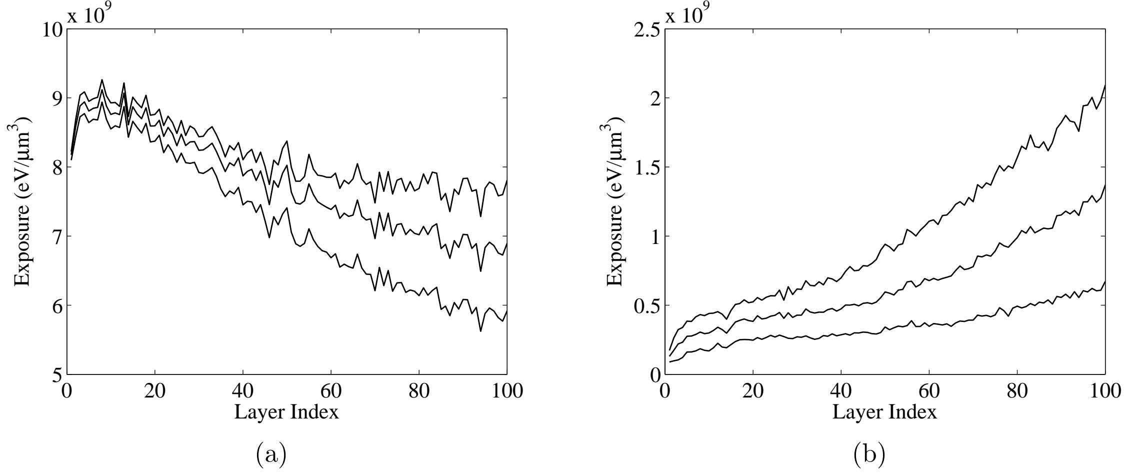

Figure 3.4: Distribution curves of layer-based exposure of three arbitrary points in (a) the exposed area and (b) the unexposed area on the substrate system of 500 nm PMMA on Si. The curves were obtained through computing the 3-D exposure distribution.

3.4 Estimation Procedure

In Section 3.3, it is implied that $d(x_0)$ is only dependent on $r(x_0, z)$. However, the resist developing process is isotropic and progresses in all possible directions. Therefore, $d(x_0)$ depends on not only $r(x_0, z)$ but also $r(x, z)$ in the domain which can be expressed by:

$$\{r(x, z)|0 < |x - x_0| \leq w\}, \tag{3.7}$$

where w is a certain width within which development of resist interacts laterally.

Though resist is developed in all possible directions, the developing process can be simply modeled as two separate parts, i.e., vertical development and lateral development, as illustrated in Fig. 3.5. Therefore, $d(x)$ may be modeled as a combination of vertical component $d_V(x)$ (defined as the depth increment due to vertical development) and lateral component $d_L(x)$ (defined as the depth increment due to lateral development), as illustrated

in Fig. 3.6. Note that the increased width due to lateral development makes the depth larger and $d_L(x)$ refers to this depth increment.

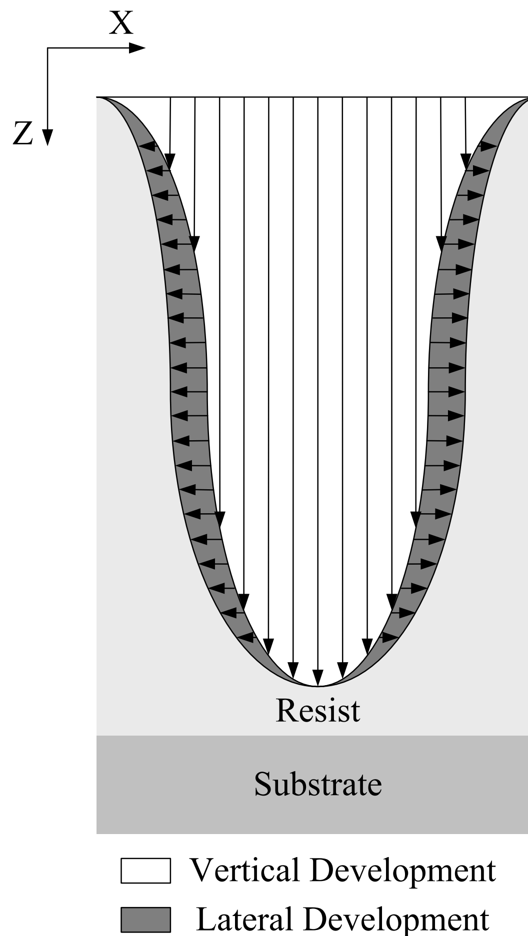

Figure 3.5: The developing process can be modeled as two separate parts, i.e., vertical development and lateral development.

For a feature as described in Section 3.3.1 with constant dose, the exposure is always highest in the center and decreases monotonically toward the tail part, which indicates the lateral development is non-existent in the center point. Hence, the exposure of the center of the feature can be estimated using the layer-based model (refer to Section 3.3.3) without considering any lateral development. For any other point in the exposed and unexposed areas, its exposure should be estimated by additionally considering its lateral development due to exposures or equivalently rates of all the points from the center point to the point

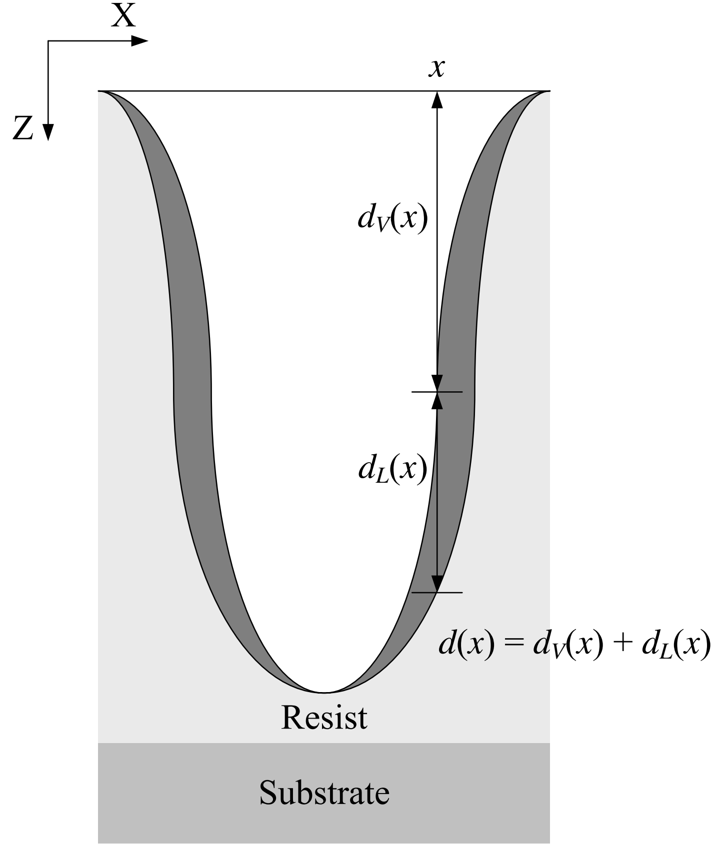

Figure 3.6: Depth at x, $d(x)$, may be modeled as a combination of vertical component $d_V(x)$ and lateral component $d_L(x)$.

itself. In the current implementation, an iterative procedure is employed in this estimation, which can be expressed by (also refer to Fig. 3.7):

$$d_L(x_i) = G[T, r(x_k)|k = 0, 1, 2, \cdots, i], \tag{3.8}$$

where $G_L[\cdot]$ represents the process of estimating lateral development.

For simplicity, the estimation procedure is described for a target pattern consisting of two lines sufficiently long along the Y-dimension and separated by distance I. In this case, the base pattern is a single line of which remaining resist profile obtained through experiment is denoted by $d_1(x)$, composed of vertical component $d_{1V}(x)$ and lateral component $d_{1L}(x)$. The remaining resist profile of the target pattern, which is to be estimated, is denoted by $d_2(x)$. The developing rate distributions of the base and target patterns are denoted by

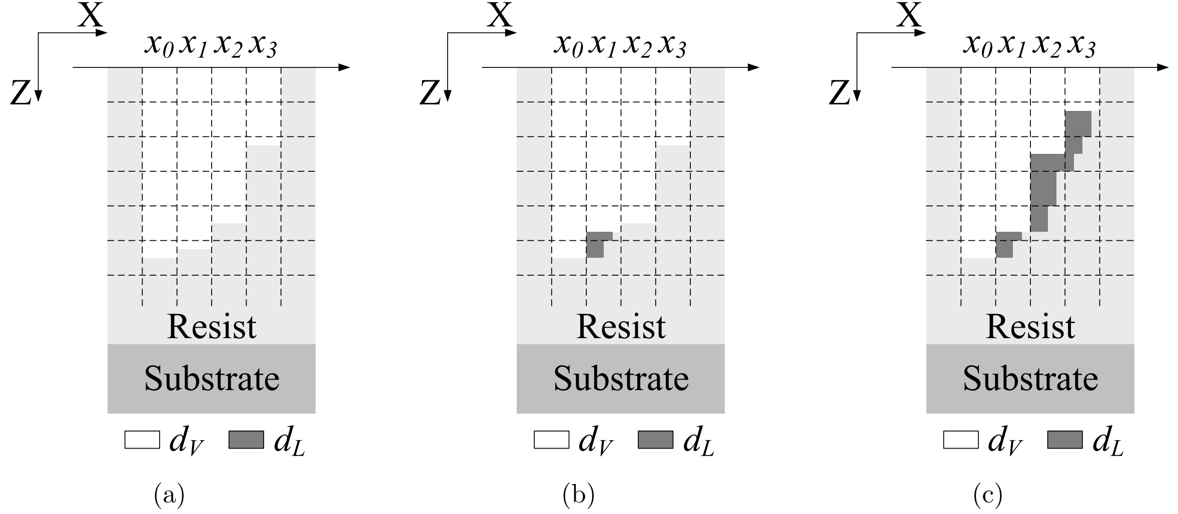

Figure 3.7: Estimation of the lateral component $d_L(x)$: (a) the initial resist profile $d(x)$, (b) after the lateral component for point x_1 is estimated, and (c) after the estimation for all points is completed.

$r_1(x,z)$ and $r_2(x,z)$, respectively. The estimation steps are depicted below (also refer to the flowchart in Fig. 3.8).

Step 1: For the base pattern, set an initial value for its exposure $e_1(x)$ (without considering change along the resist depth dimension), i.e., $e_1(x) = F^{-1}[r_1(x)] = F^{-1}[\frac{d_1(x)}{T}]$.

Step 2: Compute the layer-based exposure $e_1(x,z)$ based on $e_1(x)$ using Eq. 3.3, and convert it into developing rate $r_1(x,z)$ using the nonlinear mapping in Eq. 2.4.

Step 3: Compute the vertical component $d_{1V}(x)$ using Eq. 3.5, then additionally compute the lateral component $d_{1L}(x)$ using Eq. 3.8.

Step 4: Check the percentage depth error $\Delta d_1(x) = \frac{d_{1V}(x)+d_{1L}(x)-d_1(x)}{d_1(x)}$. If it is smaller than a certain threshold, proceed to Step 5. Otherwise, use it to control the increment of $r_1(x)$, or equivalently $e_1(x)$, and go back to Step 2.

Step 5: Compute the layer-based exposure $e_2(x,z)$, i.e., $e_2(x,z) = e_1(x,z) + e_1(x-I,z)$, and convert it into developing rate $r_2(x,z)$ using the nonlinear mapping in Eq. 2.4.

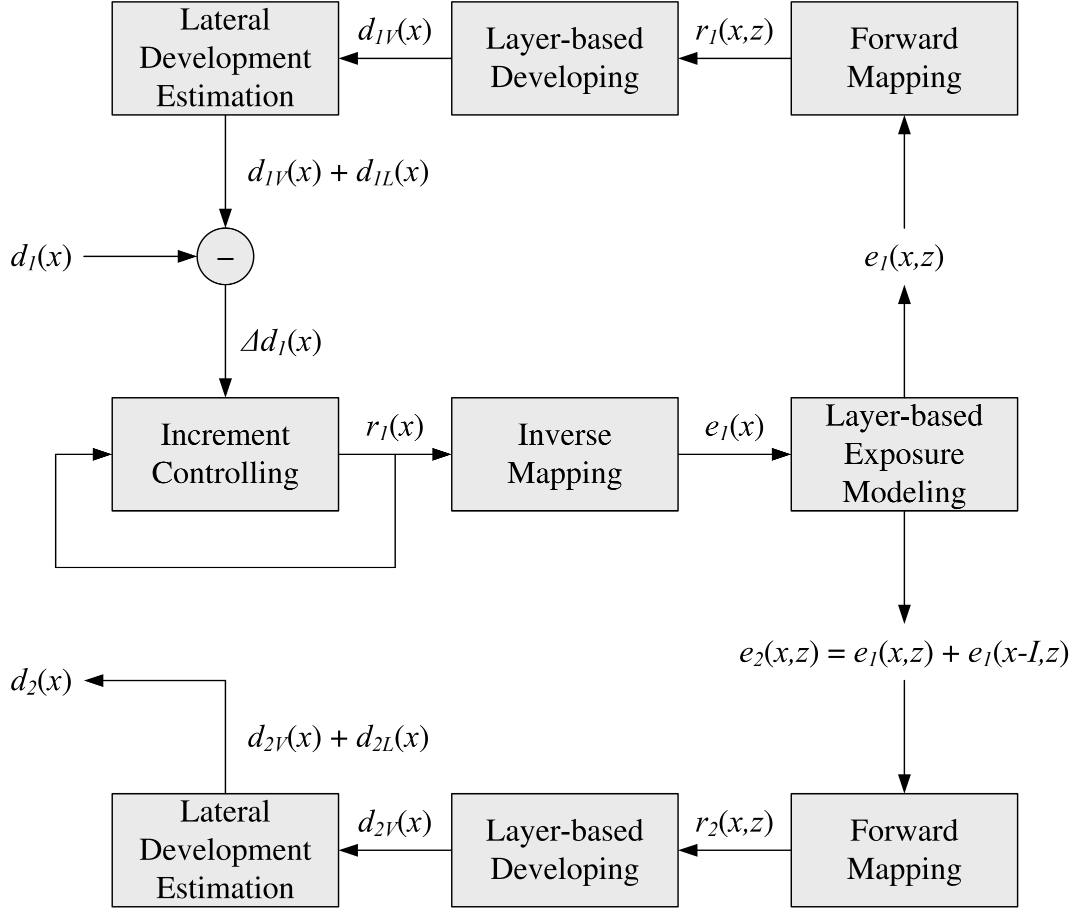

Figure 3.8: Flowchart of the proposed estimation method.

Step 6: Compute the vertical component $d_{2V}(x)$ using Eq. 3.5, then additionally compute the lateral component $d_{2L}(x)$ using Eq. 3.8.

Step 7: Derive the final depth profile $d_2(x)$ by taking both vertical and lateral components into account, i.e., $d_2(x) = d_{2V}(x) + d_{2L}(x)$.

It should be clear that the above estimation procedure can be easily generalized for N-line target patterns where $N > 2$.

3.5 Results and Discussion

3.5.1 Line/Space Patterns

In order to evaluate the performance of the proposed estimation method, an extensive simulation has been performed with line/space patterns and different substrate systems. The line width (L), space between lines (S) and the number of lines (N) are varied (refer to Fig. 3.9). The substrate system is composed of PMMA on Si where the three different PMMA thicknesses, 300 nm, 500 nm, and 1000 nm, are considered. In the current model, the resist consists of 100 layers.

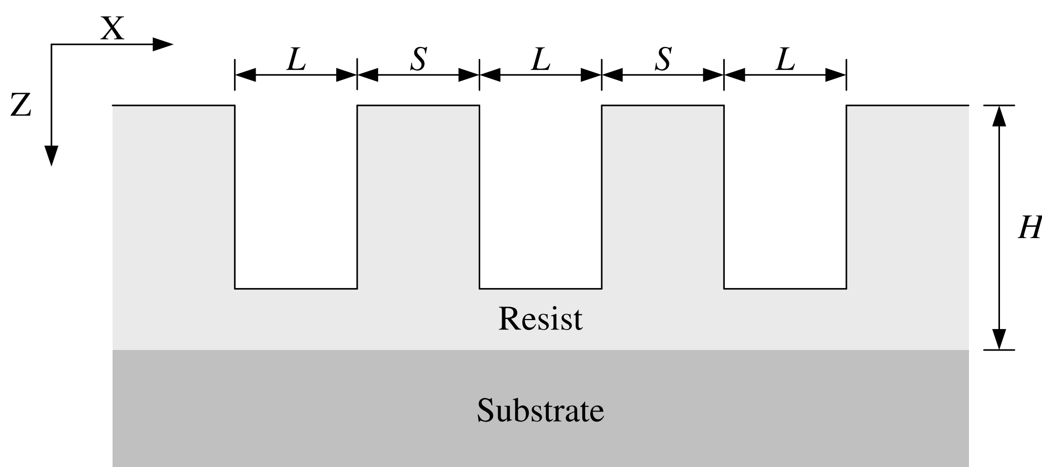

Figure 3.9: Cross-section of the resist profile of a line/space pattern.

3.5.2 Simulation Results

The proposed method and the 2-D Mod method (refer to Section 3.3.2) have been compared to the conventional method (Exp-Dev, refer to Section 3.2) which requires exposure computation and resist development simulation. A set of typical remaining resist profiles estimated by the three methods is provided in Figs. 3.10, 3.11, and 3.12.

Compared to the 2-D Mod method, it can be seen that the proposed method can achieve remaining resist profiles much closer to those by the Exp-Dev method in most cases. However, it should be noticed that the 2-D Mod method never overestimates remaining resist

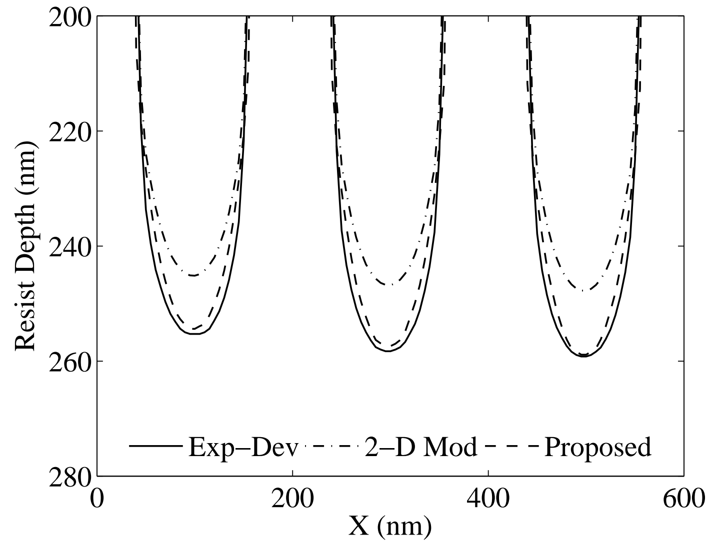

(a)

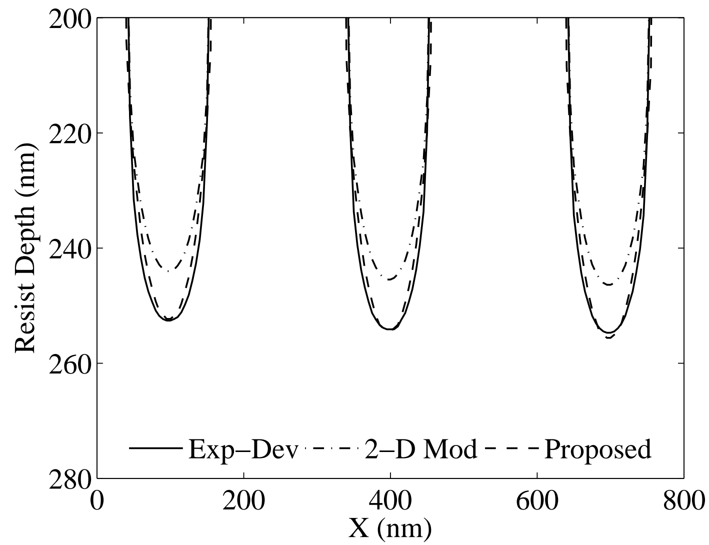

(b)

Figure 3.10: Remaining resist profiles of an 8-line pattern with (a) L = 100 nm/S = 100 nm and (b) L = 100 nm/S = 200 nm on the substrate system of 300 nm PMMA on Si.

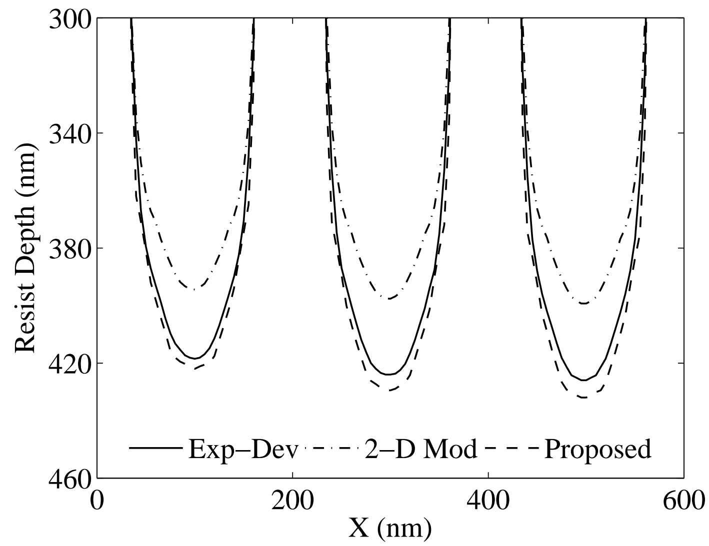

(a)

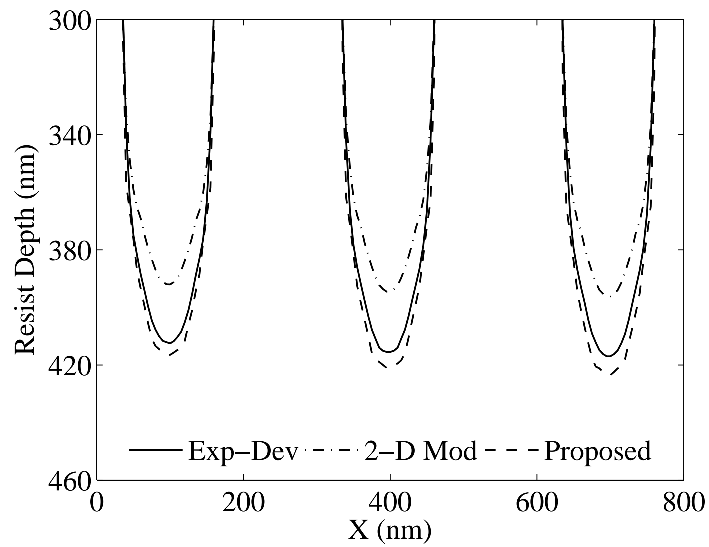

(b)

Figure 3.11: Remaining resist profiles of an 8-line pattern with (a) L = 100 nm/S = 100 nm and (b) L = 100 nm/S = 200 nm on the substrate system of 500 nm PMMA on Si.

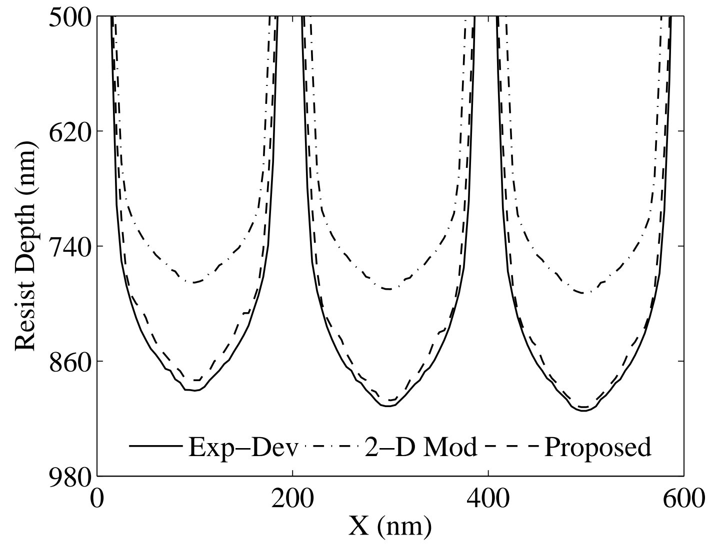

(a)

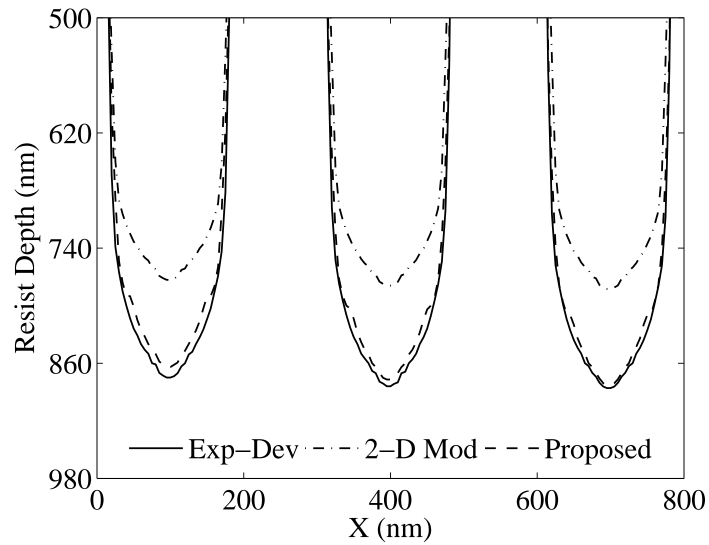

(b)

Figure 3.12: Remaining resist profiles of an 8-line pattern with (a) L = 100 nm/S = 100 nm and (b) L = 100 nm/S = 200 nm on the substrate system of 1000 nm PMMA on Si.

profiles since it employs the 2-D exposure model while the proposed method leads to a slight overestimation in some cases.

3.5.3 Performance Comparison

The 2-D Mod method and the proposed method are also compared quantitatively in terms of the percent depth errors:

$$Average\ Percent\ Depth\ Error = \frac{1}{n}\sum_{i=1}^{n}\frac{|d_{est}(i) - d_{sim}(i)|}{d_{sim}(i)} \times 100\%, \tag{3.9}$$

and

$$Max\ Percent\ Depth\ Error = \max_{i=1}^{n}\frac{|d_{est}(i) - d_{sim}(i)|}{d_{sim}(i)} \times 100\%, \tag{3.10}$$

where d_{est} denotes the depth estimated by the 2-D Mod method or the proposed method, and d_{sim} denotes the depth simulated by the Exp-Dev method, respectively, and n is the number of points along the X-dimension.

Simulation Settings				2-D Mod Method		Proposed Method	
Ratio of L to S	Number of Lines (N)	Developing Time (sec)	Resist Thickness (nm)	Average (%)	Maximum (%)	Average (%)	Maximum (%)
0.33	8	40	1000	10.78	11.47	0.89	2.57
0.5	8	40	1000	11.47	11.89	1.03	2.79
1.0	8	40	1000	13.08	13.58	1.02	2.74
2.0	8	40	1000	15.65	16.56	1.41	2.91

Table 3.1: Average and maximum percent depth errors with respect to the ratio of L to S with N = 8 on the substrate system of 1000 nm PMMA on Si.

Simulation Settings				2-D Mod Method		Proposed Method	
Ratio of L to S	Number of Lines (N)	Developing Time (sec)	Resist Thickness (nm)	Average (%)	Maximum (%)	Average (%)	Maximum (%)
1.0	8	40	500	6.08	6.61	1.51	2.21
1.0	16	40	500	7.23	7.91	1.69	2.82
1.0	32	40	500	7.69	9.08	4.03	6.36

Table 3.2: Average and maximum percent depth errors with respect to the number of lines with L = 100 nm/S = 100 nm on the substrate system of 500 nm PMMA on Si.

Simulation Settings				2-D Mod Method		Proposed Method	
Ratio of L to S	Number of Lines (N)	Developed Depth (nm)	Resist Thickness (nm)	Average (%)	Maximum (%)	Average (%)	Maximum (%)
1.0	8	333	1000	7.73	8.78	0.27	0.97
1.0	8	514	1000	8.85	9.66	0.29	1.12
1.0	8	716	1000	11.30	12.10	1.26	2.31
1.0	8	914	1000	13.08	13.58	1.02	2.74

Table 3.3: Average and maximum percent depth errors with respect to the developed depth (controlled by the developing time) with L = 100 nm/S = 100 nm and N = 8 on the substrate system of 1000 nm PMMA on Si.

Simulation Settings				2-D Mod Method		Proposed Method	
Ratio of L to S	Number of Lines (N)	Developing Time (sec)	Resist Thickness (nm)	Average (%)	Maximum (%)	Average (%)	Maximum (%)
1.0	8	40	300	4.57	5.14	1.26	3.05
1.0	8	40	500	6.08	6.61	1.51	2.21
1.0	8	40	1000	13.08	13.58	1.02	2.74

Table 3.4: Average and maximum percent depth errors with respect to the resist thickness (PMMA thickness) with L = 100 nm/S = 100 nm and N = 8.

This percent depth error is defined for general resist profiles (binary or grayscale lithography). But for binary lithography where feature width is of main concern, percent width error may be adopted. The average and maximum percent depth errors are provided with respect to the ratio of L to S, the number of lines, the developed depth (controlled by the developing time), and the resist thickness in Tables. 3.1, 3.2, 3.3, and 3.4, which are also plotted in Fig. 3.13. The results show that the proposed method outperforms the 2-D

Mod method by reducing the average error up to about 14.24%. And the reduction of the maximum error is about 13.65%.

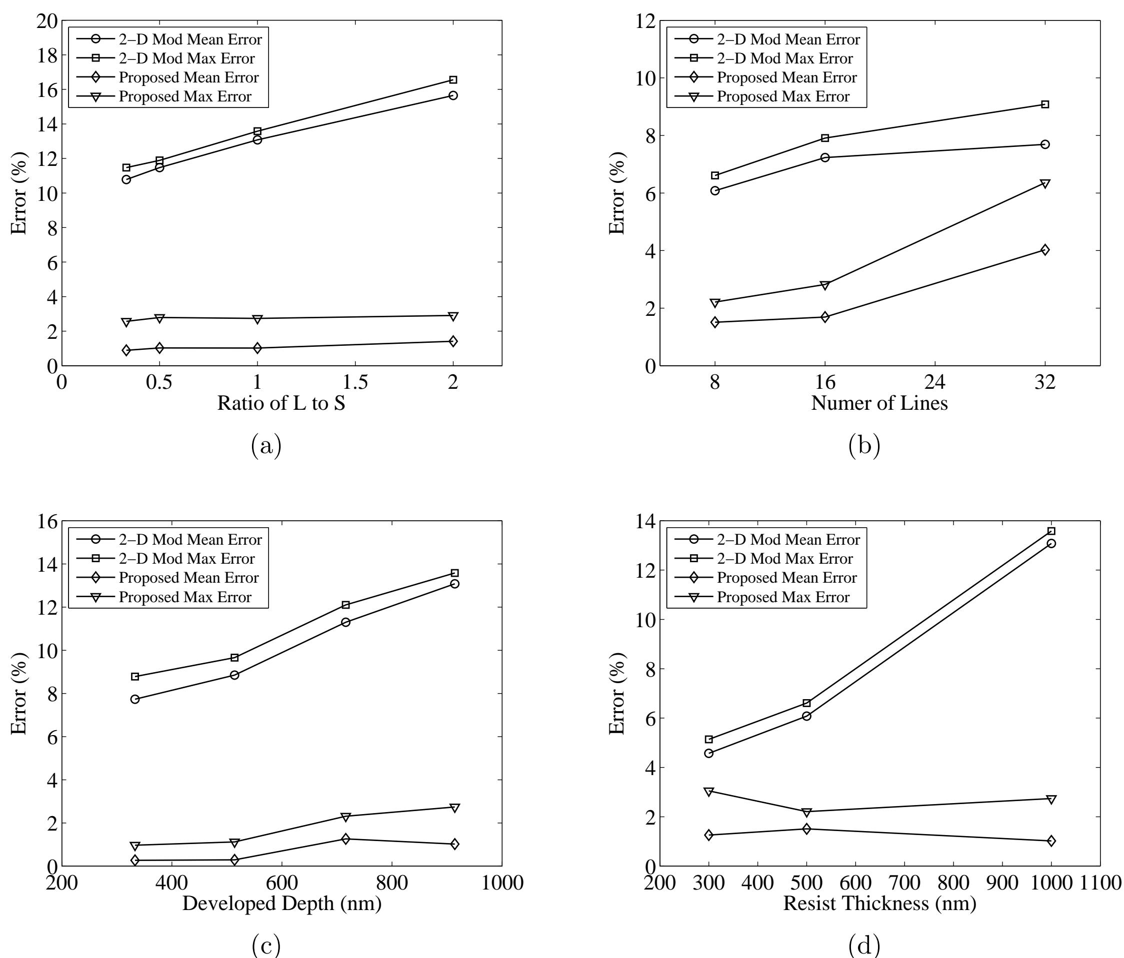

Figure 3.13: Average and maximum percent depth errors with respect to (a) the ratio of L to S with N = 8 on the substrate system of 1000 nm PMMA on Si; (b) the number of lines with L = 100 nm/S = 100 nm on the substrate system of 500 nm PMMA on Si; (c) the developed depth (controlled by the developing time) with L = 100 nm/S = 100 nm and N = 8 on the substrate system of 1000 nm PMMA on Si; (d) the resist thickness (PMMA thickness) with L = 100 nm/S = 100 nm and N = 8.

From the above tables and plots of errors, it is observed that as each of the ratio of L to S, the number of lines, the developed depth (controlled by the developing time), and the resist thickness increases, the advantage of the proposed method becomes more and more visible. For a larger ratio of L to S or a larger number of lines, interaction among lines increases and therefore a less accurate estimation method, 2-D Mod, suffers more. For a

thicker resist, the exposure variation along the resist depth dimension is larger, which makes the 2-D Mod cause larger errors since it ignores the variation.

3.5.4 Experimental Results

The proposed estimation scheme has been tested also via experiment. Si wafer was spin-coated with 300 nm PMMA and soft-baked at 160 ^{o}C for 1 minute. Two separated long lines of 100 nm wide were exposed with different doses ($200\mu C/cm^2$ and $225\mu C/cm^2$) using ELIONIX ELS-7000 e-beam lithography system (50 KeV) and the sample was developed in MIBK:IPA=1:2 for 40 seconds.

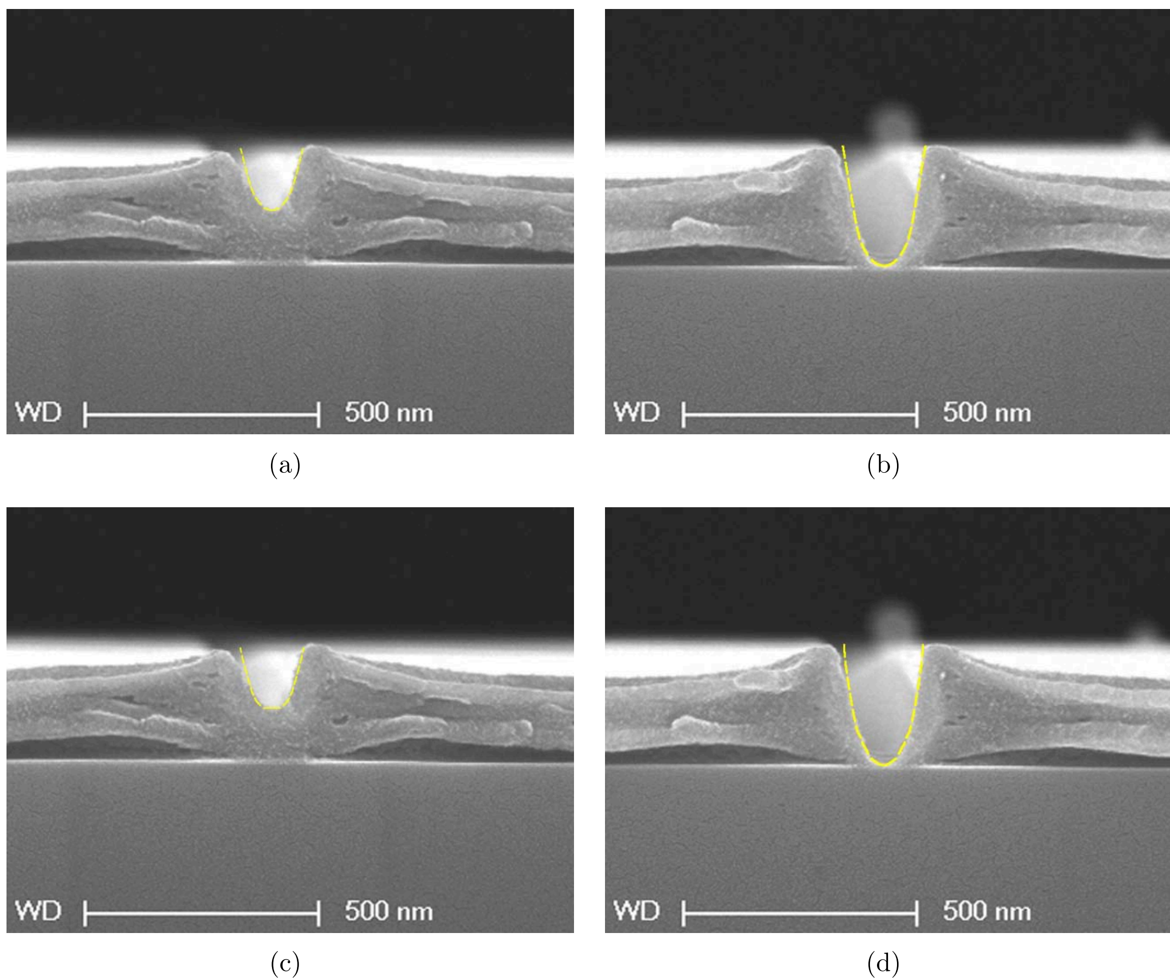

(a) (b) (c) (d)

Figure 3.14: Experimental results of (a) resist profile of set I measured from the SEM image; (b) resist profile of set II measured from the SEM image; (c) resist profile of set I estimated from that of set II; (d) resist profile of set II estimated from that of set I.

The resist profiles of each set are measured from the cross-section SEM image, which are provided in Fig. 3.14(a) (denoted by set I) and Fig. 3.14(b) (denoted by set II). Using the resist profile of one set as the source, that of the other is estimated through the proposed method, which are provided in Fig. 3.14(c) and Fig. 3.14(d). The average percent depth errors between the measured and estimated resist profiles of set I and set II are 5.25% and 3.81%, respectively, demonstrating high accuracy of the proposed estimation method.

3.6 Summary

In this chapter, a method for estimation of remaining resist profiles of line/space patterns, which does not require exposure calculation and resist development simulation, is proposed. By analyzing the simulation results from a set of base patterns on different substrate systems, a layer-based model is formulated. An adaptive procedure is employed in estimation of the lateral development in remaining resist profiles. Through simulation and also experiments, it is shown that the proposed method estimates almost the same resist profiles as those by a typical conventional method like the Exp-Dev method in most cases, and outperforms the 2-D Mod method by further reducing the estimation error. Therefore, the proposed method has a good potential to provide an alternative way for estimation of resist profiles where the conventional methods are not applicable and/or are too time-consuming.

Chapter 4

Critical Dimension Control for Large-scale Uniform Patterns

4.1 Introduction

For circuit patterns with nanoscale features, it is not unusual that the actual written pattern is substantially different from the written pattern estimated by a 2-D PEC method. One of the reasons for this deviation is that the 2-D model ignores the exposure variation along the resist depth dimension. In an earlier study [94], it was shown that the remaining resist profile estimated using a 2-D model can be significantly different from the one based on a 3-D model which considers the depth-dependent exposure variation. Another reason is that the actual resist profile cannot be derived directly from the exposure distribution, e.g., the developing rate is not linearly proportional to the exposure at a given point. Therefore, the PEC methods which consider the exposure only may suffer from substantial CD errors or deviation from the target resist profile in general. In addition, with a 2-D model, it is not possible to consider the lateral development of resist which affects the resist profile, in particular the sidewall shape, significantly.

In the previous work [94, 95, 96], the limitations of 2-D PEC were analyzed and the need for 3-D PEC was well demonstrated for circuit patterns with nanoscale features. In [95], the idea of true 3-D PEC was proposed and its first implementation for a single line and a small number of lines was reported. In this implementation, the resist profile estimated through simulation of resist development process was employed instead of the exposure distribution, in order to obtain more realistic results.

In this chapter, an extension of the 3-D PEC method for large-scale uniform patterns is described. A challenge is that a 3-D PEC method requires a tremendous amount of computation due to the increased dimensionality and resist development simulation. The

feature-by-feature correction procedure would be too time-consuming to be practical. Hence, a new 3-D PEC method has been developed which cuts down the required computation greatly and still achieves the resist profile closely matched to the target one. It explicitly corrects the features only at the critical locations in a circuit pattern and employs a fast correction procedure for other features exploiting the uniformity of feature distribution. A distinct aspect of the method is that it attempts to adjust the exposures cross (inside and outside) the feature boundary in order to control the location and shape of sidewall in the resist profile.

The rest of the chapter is organized as follows. The large-scale uniform patterns are described in Section 4.2. The 2-D and 3-D correction methods are briefly reviewed in Section 4.3. The proposed 3-D correction procedure is presented in detail in Section 4.4. Simulation results are discussed in Section 4.5, followed by a summary in Section 4.6.

4.2 Large-scale Uniform Patterns

A large-scale uniform pattern consists of a large number of same features (line, square, etc.) which is replicated uniformly throughout the pattern. One practical issue for this kind of patterns is that the proximity effect is considerable due to a very high pattern density. Especially, compared to the corner and edge of the pattern, the center of the pattern suffers from much higher proximity effect which results in a severe deviation of resist profiles at different locations (refer to Fig. 4.1).

4.3 Correction Methods

Let's assume that a target written pattern is specified by the corresponding resist profile (e.g., line widths at the top, middle and bottom layers) and the cross-section of resist profile is in the X-Z plane (refer to Fig. 2.4). During correction, at each location (x, y) in a circuit pattern, the cross-section of resist profile needs to be examined. Then, $e(x, y, z)$ and $r(x, y, z)$ can be replaced by $e(x, z)$ and $r(x, z)$, respectively.

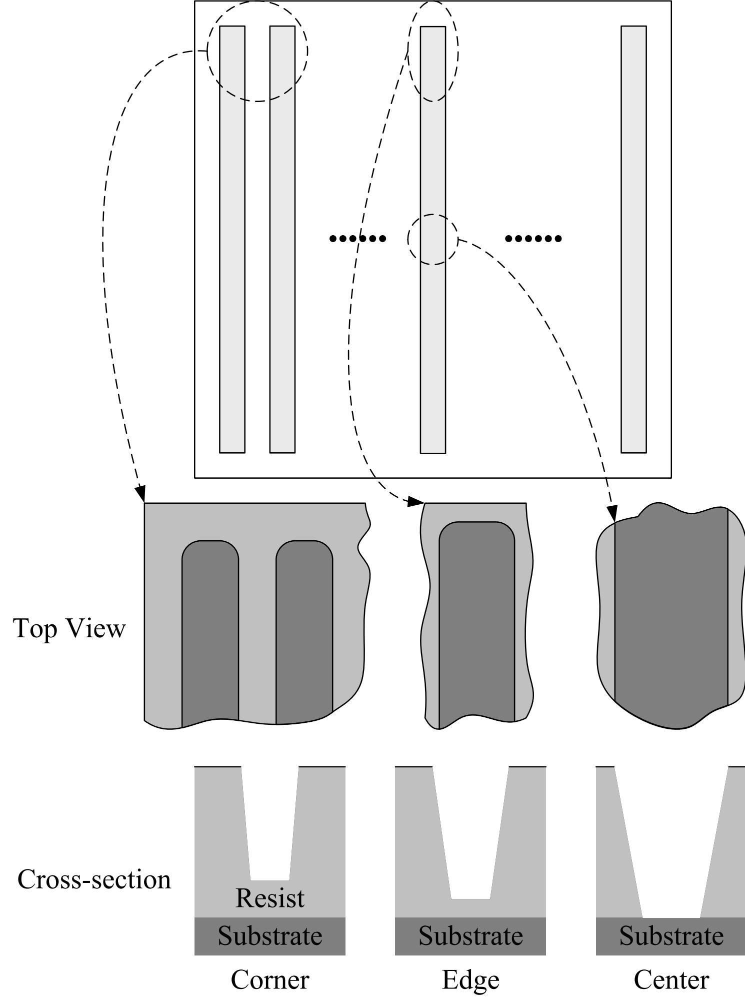

Figure 4.1: The deviation of resist profiles at corner, edge and center of a large-scale uniform pattern without PEC.

4.3.1 2-D Exposure Correction (2-D PEC)

In the 2-D exposure model, the exposure is assumed not to vary along the resist depth dimension (Z-dimension), i.e., $e(x, z)$ in the cross-section is averaged over $0 \leq z \leq H$ (refer to Fig. 2.4), resulting in $e(x)$. Let $h(x)$ represent the depth distribution (i.e., depth at x) in the target resist profile. A target exposure distribution $E_t(x)$ is derived from $h(x)$ by:

$$E_t(x) = F^{-1}[\frac{h(x)}{T}], \tag{4.1}$$

where T is the developing time.

The exposure $E_t(x)$ can be considered as a threshold for a certain point to be fully developed (refer to Fig. 4.2).

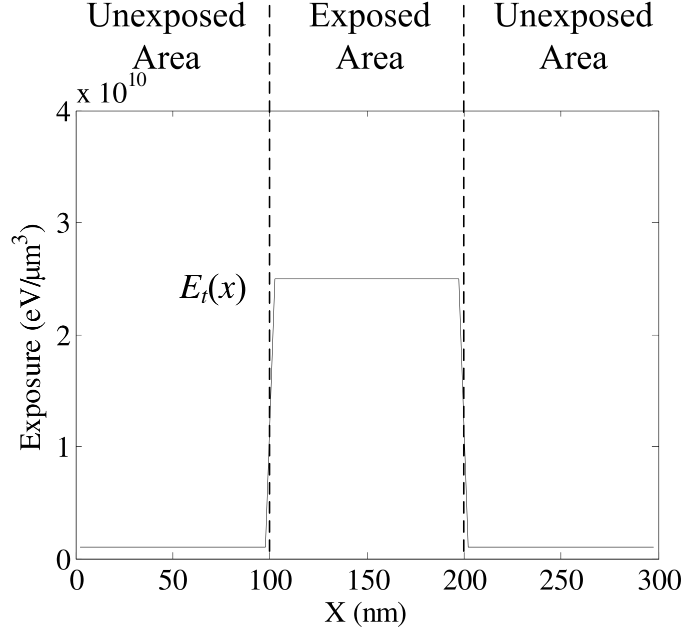

Figure 4.2: The target 2-D exposure distribution is illustrated for a line feature.

Then, the dose distribution $d(x)$ required to achieve the target resist profile (depth distribution) $h(x)$ may be determined iteratively by minimizing the following error:

$$Error = \sum_x |e(x) - E_t(x)|. \tag{4.2}$$

In each iteration, $e(x)$ is computed from $d(x)$ according to Eq. 2.3. The objective of this 2-D correction scheme is to control the dose distribution $d(x)$ such that $e(x)$ is as high as the threshold $E_t(x)$ in the exposed area, and as low as possible in the unexposed area.

4.3.2 3-D Resist Profile Correction (3-D PEC)

Unlike the above 2-D exposure correction, this 3-D correction incorporates the estimation of remaining resist profile into the correction procedure and utilizes the resist profile to determine the dose distribution based on a 3-D model. The overall correction procedure is very similar to that of the 2-D correction. However, the error, which is to be minimized

determining the corrected dose distribution, is computed based on the estimated remaining resist profile rather than the exposure distribution, and is given by:

$$Error = \max_{j} |p(j) - q(j)|, \tag{4.3}$$

where $p(j)$ and $q(j)$ denote the width distribution of the estimated remaining resist profile and that of the target resist profile, respectively (refer to Fig. 4.3).

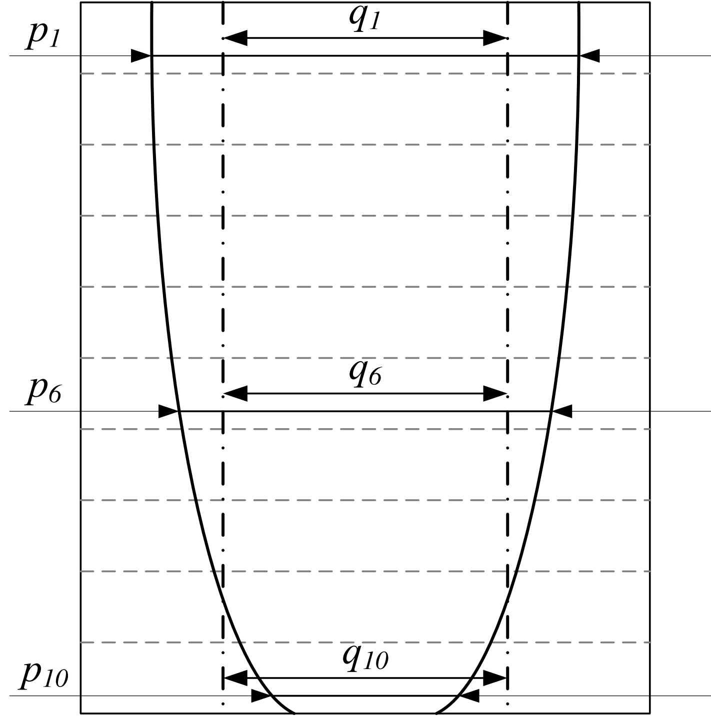

Figure 4.3: The cross-section of resist profile is illustrated for a line feature where p_j and q_j are the actual and target widths at the j-th layer, respectively, where the resist is modeled by 10 layers.

4.4 Proposed Correction Procedure

The proposed 3-D PEC method minimizes the deviation of resist profile from the target one, avoiding the feature-by-feature correction without sacrificing the correction quality. It consists of three steps: correcting a single feature in isolation, global adjustment of feature-wise dose, and intra-feature dose control at critical locations.

4.4.1 Correction of a Single Feature

In the first step of the proposed approach, a single instance of the repeated feature in the pattern is corrected in isolation. The feature is partitioned into regions for each of which a dose is determined using the 3-D resist profile correction (refer to Section 4.3.2).

The cost function to determine the dose distribution is given by (also refer to Fig. 4.3):

$$Error = \max_{j=1,5,10} |p(j) - q(j)|, \tag{4.4}$$

where j is the layer index (Z-dimension) from 1 to 10. $p(j)$ and $q(j)$ are considered as $p(z)$ and $q(z)$ (refer to Section 4.3.2) sampling at j-th layer.

In the current implementation, the error defined in Eq. 4.3 is computed only considering the top, middle and bottom layers of resist. The maximum of the three errors is minimized such that the profile as close to the target resist profile as possible is obtained. The region-wise dose distributions along with the resist profiles before and after correction are illustrated for a line feature partitioned into 5 regions in Fig. 4.4.

The dose distribution within the feature is denoted by $d(i)$ and the corresponding exposure distribution by $e(i)$ where i is the region index (refer to Fig. 4.4). The spatial averages of $d(i)$ and $e(i)$ are denoted by D and E, respectively, i.e., $D = \frac{1}{R}\sum_{i=1}^{R} d(i)$ and $E = \frac{1}{R}\sum_{i=1}^{R} e(i)$, where R is the number of regions. Note that all of the notations, $d(i)$, $e(i)$, D and E (i.e., without subscripts) are for a single feature in isolation.

4.4.2 Feature-wise Global Adjustment

In the second step, the global distribution of feature-wise dose throughout the pattern is derived by the following deconvolution:

$$A = E_t \circledast^{-1} psf, \tag{4.5}$$

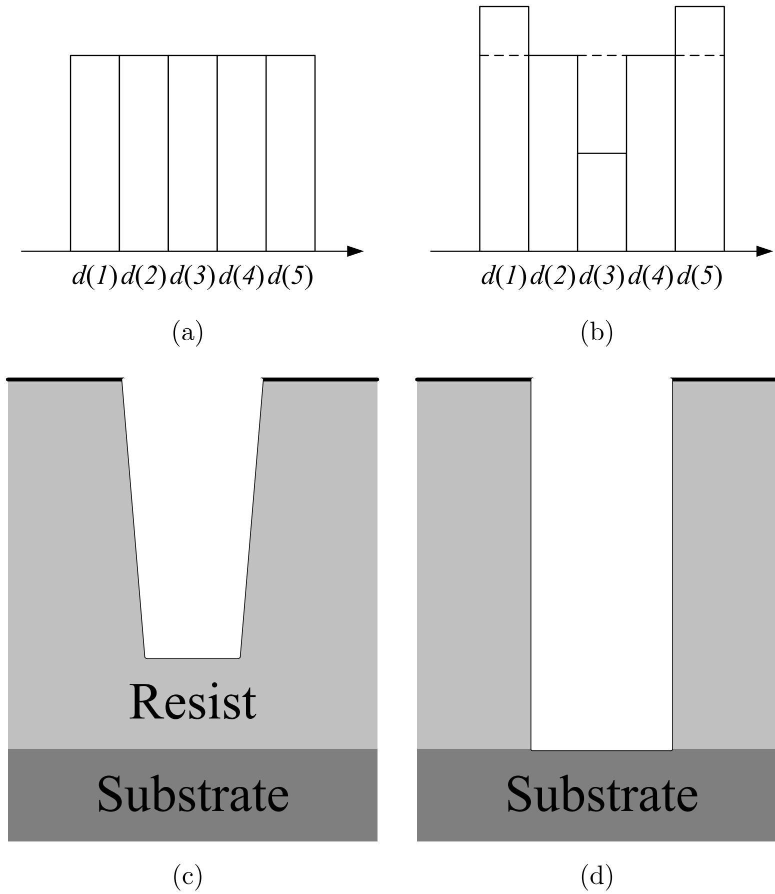

Figure 4.4: Illustration of (a) the region-wise dose distribution within the feature before correction, (b) the region-wise dose distribution within the feature after correction, (c) the corresponding resist profile before correction, and (d) the corresponding resist profile after correction.

where $E_t(m, n)$ is the target (average) exposure for the m, n-th location of the feature and is assigned the value of E (refer to Section 4.4.1), and psf is the normalized PSF (refer to Section 2.2) sampled at the feature interval.

The output of the deconvolution, i.e., matrix A, which specifies the (average) feature-wise dose distribution required to achieve E at all locations of the feature, is referred to as deconvolution surface. This deconvolution is not computationally intensive since the spatial resolution involved is coarse (feature size). For the m, n-th location of the pattern, $d(i)$ is weighted (scalar multiplication) by the deconvolution surface A to results in (refer to Fig. 4.5):

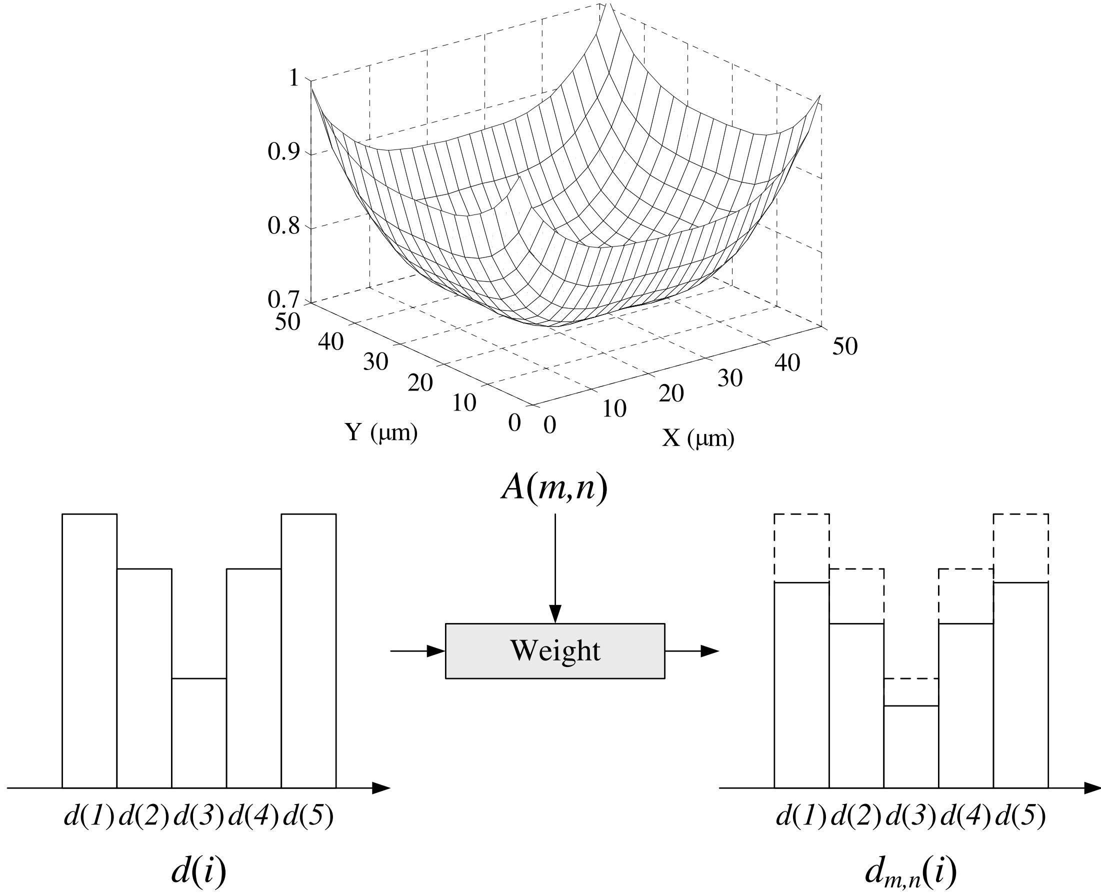

Figure 4.5: For each location (m, n) of the feature (line segment), $d(i)$ is weighted by the deconvolution surface $A(m, n,)$.

$$d_{m,n}(i) = d(i) \cdot A(m, n). \tag{4.6}$$

The spatial average of $d_{m,n}(i)$ is denoted by $D_{m,n}$. Now, $e_{m,n}(i)$, corresponding to $d_{m,n}(i)$, is well balanced to be E throughout the pattern, but the exposure in the unexposed area (referred to as background exposure) may vary with location (refer to Fig. 4.6). Then, as illustrated in Fig. 4.7, the resist profiles at different locations would be different. This variation is due to the difference in the background exposure even though the internal exposure is equalized by the deconvolution surface. In order to achieve the resist profile throughout

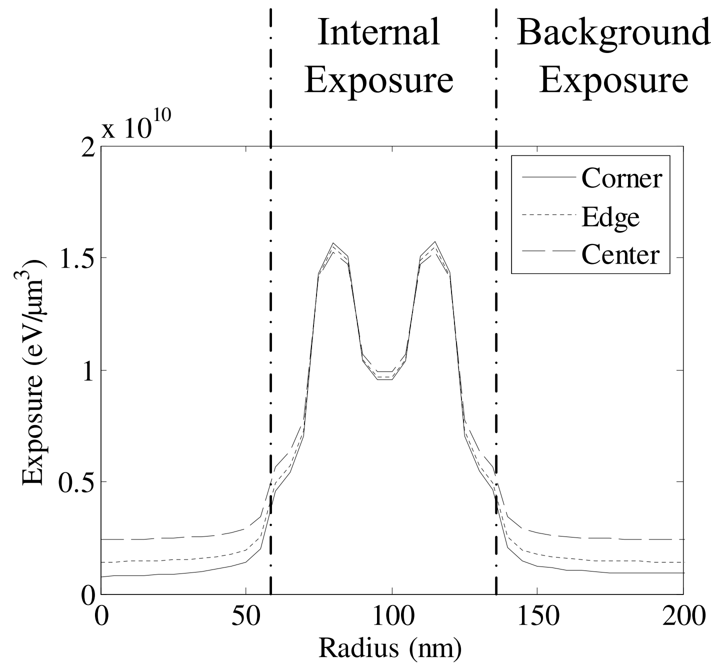

Figure 4.6: The exposure distributions obtained using the global (weighted) dose distribution.

the pattern, one may further adjust the internal exposure to compensate for the difference in the background exposure among locations.

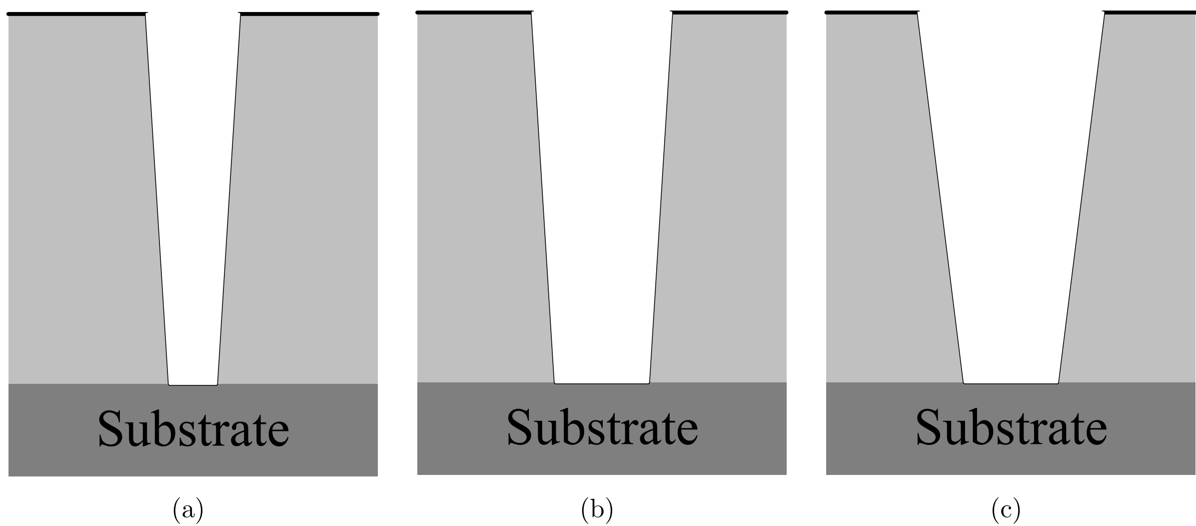

(a) (b) (c)

Figure 4.7: The corresponding resist profiles at (a) corner, (b) edge, and (c) center of the pattern from the exposure distributions obtained using the global (weighted) dose distribution.

4.4.3 Critical-location-based Dose Control

In a large-scale uniform pattern, the same feature such as line, square, etc., is replicated uniformly throughout the pattern. Then, the global spatial distribution of exposure is smooth, and in turn the global distribution of feature-wise dose required for correction must be smooth, which is indicated by the deconvolution surface (refer to Section 4.4.2). Therefore, it is sufficient to consider only the features at the critical locations, e.g., corner, edge and center (refer to Fig. 4.8) instead of a feature-by-feature correction.

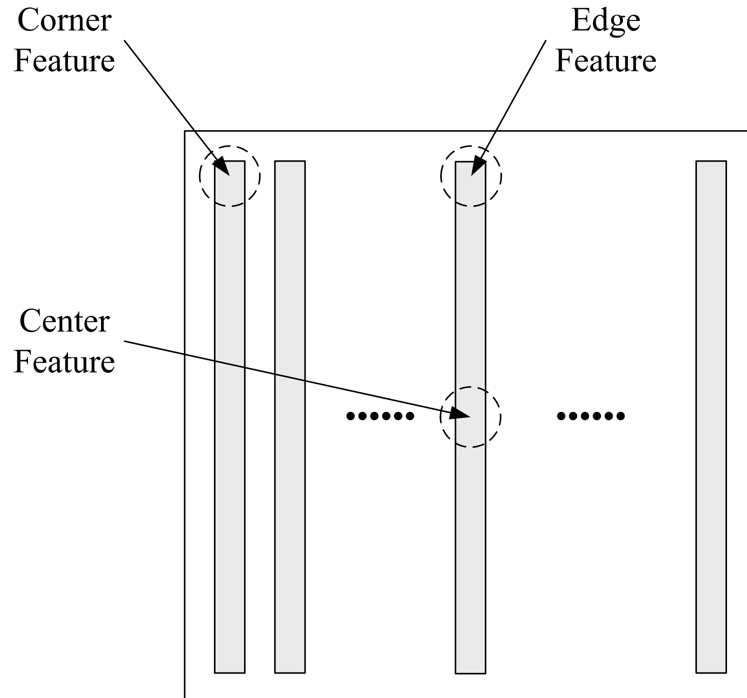

Figure 4.8: Line segments only at the critical locations of the pattern are corrected individually.

Therefore, in the third step, $d_{m,n}(i)$ at each of the three critical locations is adjusted based on the same scheme in Section 4.4.1. One difference is that the background exposure at each critical location, which is computed using the deconvolution surface (refer to Section 4.4.2), should be considered in the iterative correction. For each critical location, the total exposure is the sum of the base exposure and the background exposure, where the base exposure depends on $d_{m,n}(i)$ within each iteration, and the background exposure only

depends on $D_{m,n}$, i.e., constant among iterations. Since the resist profile after the second step is already close to the target one, $d_{m,n}(i)$ can be used as an initial distribution in order to minimize the number of iterations.

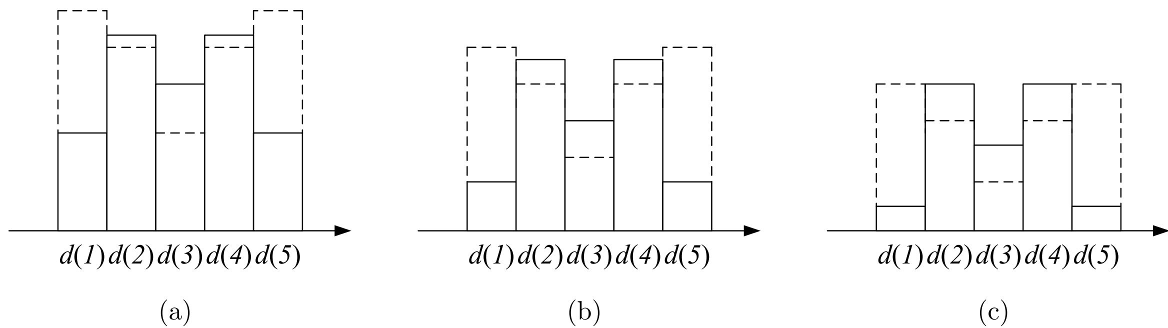

Figure 4.9: The adjusted dose distributions for (a) corner, (b) edge, and (c) center of the pattern.

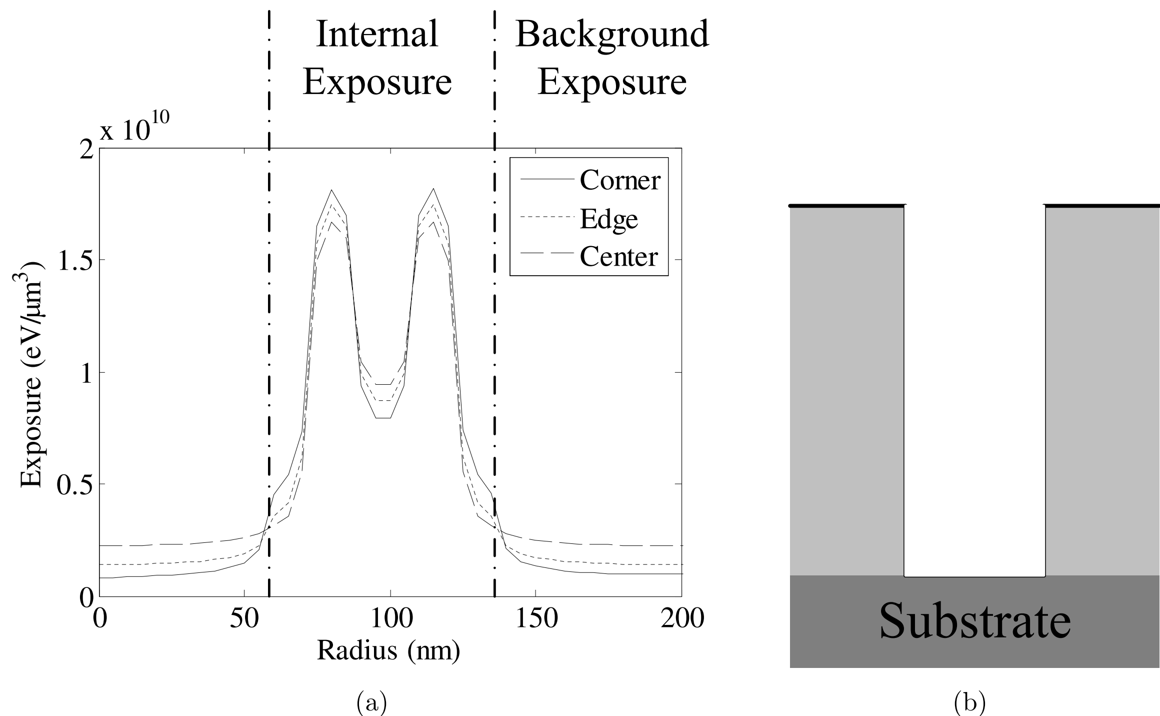

Figure 4.10: (a) The corresponding exposure distributions and (b) the corrected resist profile using the adjusted dose distributions.

The corrected dose distributions at the critical locations are illustrated in Fig. 4.9 and the corresponding exposure distributions in Fig. 4.10(a). Achieving the identical exposure distribution at all locations in a large pattern, which is attempted by most of the conventional

PEC methods, would be extremely difficult if not impossible. The proposed correction method lets the difference in the internal exposure compensate for that in the background exposure such that the deviation from the target resist profile is minimized at the critical locations (refer to Fig. 4.10(b)). After the final $d_{m,n}(i)$ is obtained at each critical location, a 2-D global interpolation is employed to compute the $d_{m,n}(i)$ at all other locations based on the deconvolution surface.

Through the above correction procedure (also refer to the flowchart in Fig. 4.11), the dose distribution is well adjusted throughout the pattern with accuracy and efficiency.

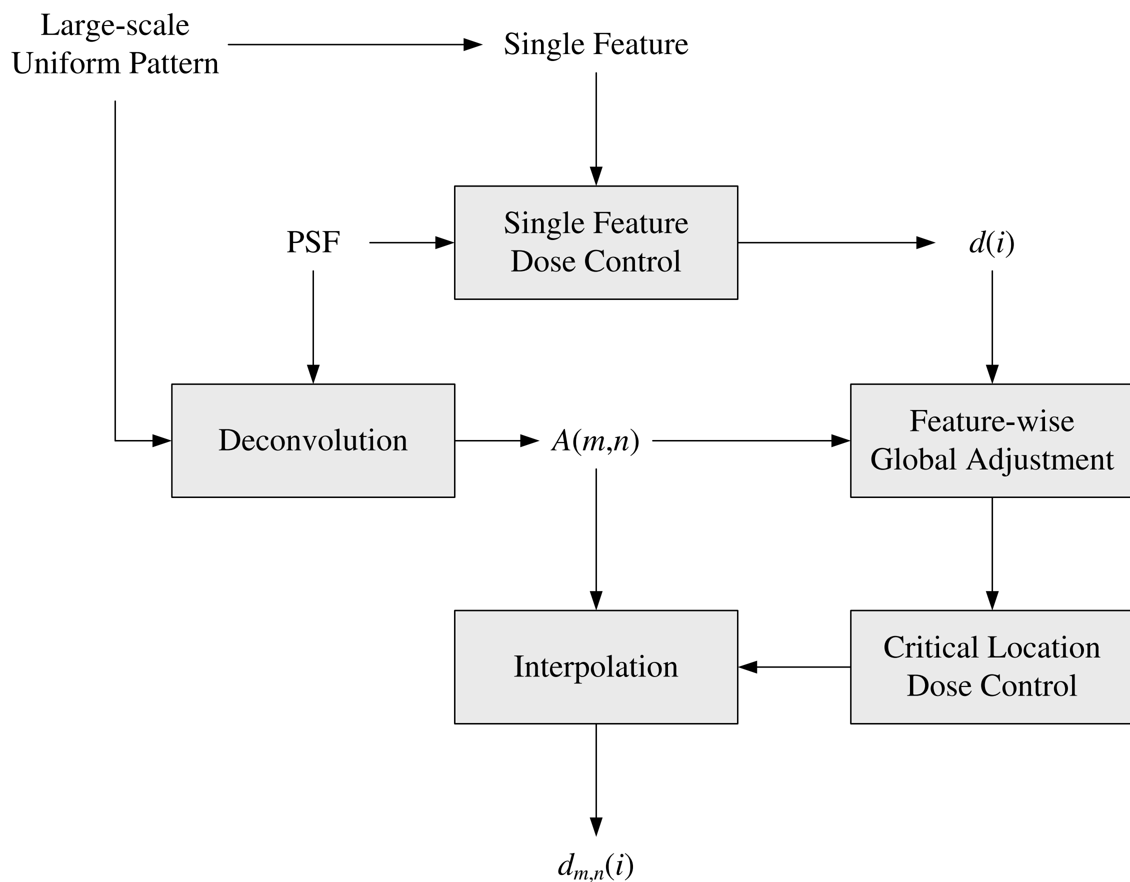

Figure 4.11: Flowchart of the proposed correction procedure.

4.5 Results and Discussion

4.5.1 Test Patterns

The proposed approach to 3-D PEC for large-scale uniform patterns has been implemented and its performance has been analyzed through simulation. Two kinds of the uniform pattern consisting of lines shown in Fig. 4.12 are employed for performance analysis. In the one, to be referred to as Pattern I, each line is 51 μm long and 50 nm wide, and the gap between lines is 50 nm. In the other pattern, to be referred to as Pattern II, each line is 51 μm long and 100 nm wide, and the gap between lines is 100 nm. Both patterns cover the full range of electron scattering (for 50 KeV). The correction program partitions each line into segments of 3 μm for dose control. The three critical and three test locations are shown in Fig. 4.12.

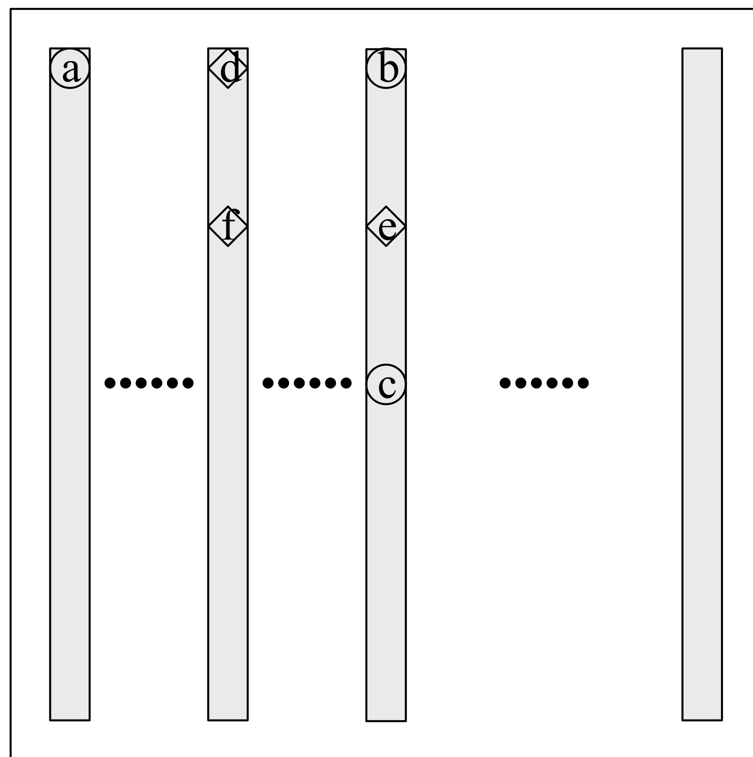

Figure 4.12: Critical locations (marked by $\circ$) and test locations (marked by $\diamond$) in a test pattern.

4.5.2 Simulation Results

The PSFs employed in the simulation are generated by a Monte Carlo simulation method, SEEL [111]. The substrate systems employed in the simulation are composed of PMMA on Si where the three different PMMA thicknesses, 100 nm, 300 nm, and 500 nm, are considered. The beam energy is set to 50 KeV with the beam diameter of 5 nm. These three substrate systems along with the two patterns provide six different combinations so that the proposed approach can be thoroughly tested.

The patterns are corrected by the 2-D PEC method (refer to Section 4.3.1) and the proposed 3-D PEC method for the target resist profile of vertical sidewall. No correction (a uniform dose for all features), the 2-D PEC method, and the 3-D PEC method are compared with a constraint that the total dose for a pattern must be the same for all the methods. Also in all cases, only 80% of the line width is exposed in order to compensate the high pattern density (50%). The results (cross-section resist profiles) of Pattern I for 300 nm PMMA on Si are provided in Figs. 4.13, 4.14, and 4.15.

From the profiles obtained without correction (Fig. 4.13), it can be seen that the resist profile significantly varies with location. The line width is not uniform and the sidewall is clearly overcut. A distinct aspect of the 3-D PEC method is that it explicitly equalizes the resist profile (rather than the exposure) of a feature throughout a pattern. Though the resist profiles (Fig. 4.14) obtained by the 2-D PEC method are better than those without correction, the variation of resist profile among locations is still substantial. However, as can be seen in Fig. 4.15, the proposed 3-D PEC method greatly improves the uniformity of resist profile among not only the critical locations but also the test locations, and also achieves the resist profiles much closer to the target one in terms of CD error and sidewall shape (vertical).

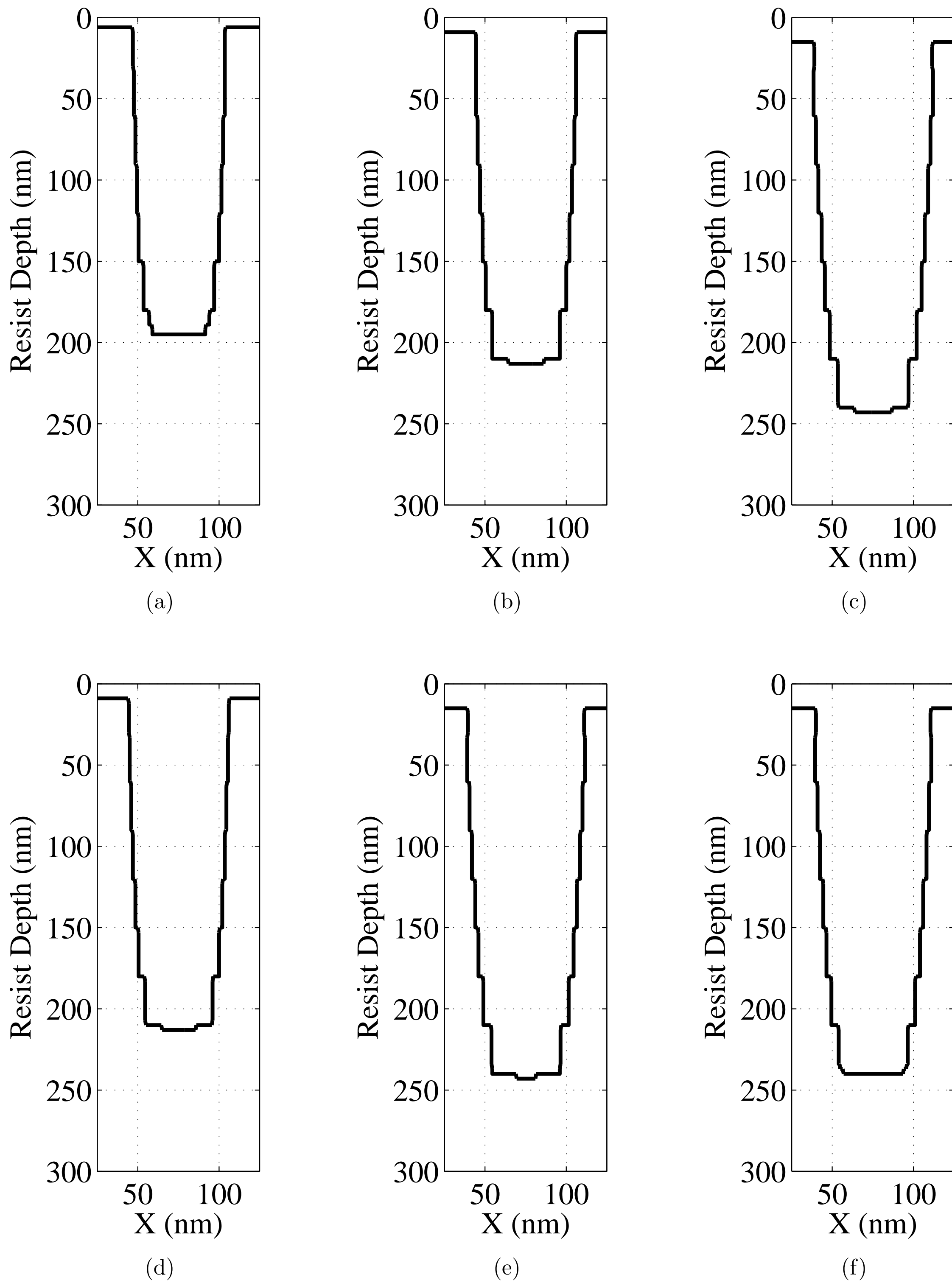

Figure 4.13: Cross-section resist profiles without correction (i.e., uniform dose) at the critical locations ((a) corner, (b) edge and (c) center; refer to Fig. 4.12) and the test locations ((d), (e) and (f); refer to Fig. 4.12).

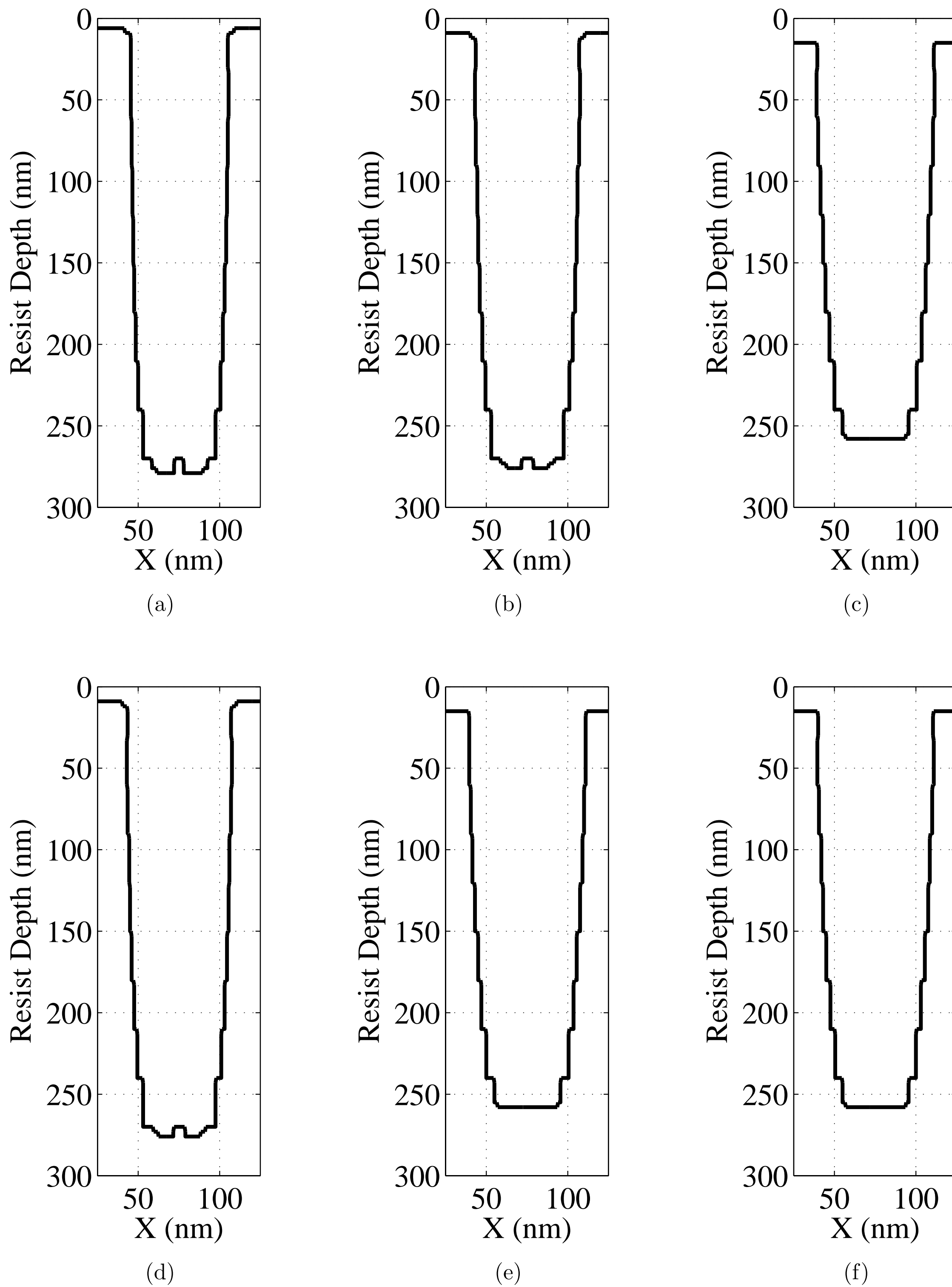

Figure 4.14: Cross-section resist profiles achieved by 2-D PEC method at the critical locations ((a) corner, (b) edge and (c) center; refer to Fig. 4.12) and the test locations ((d), (e) and (f); refer to Fig. 4.12).

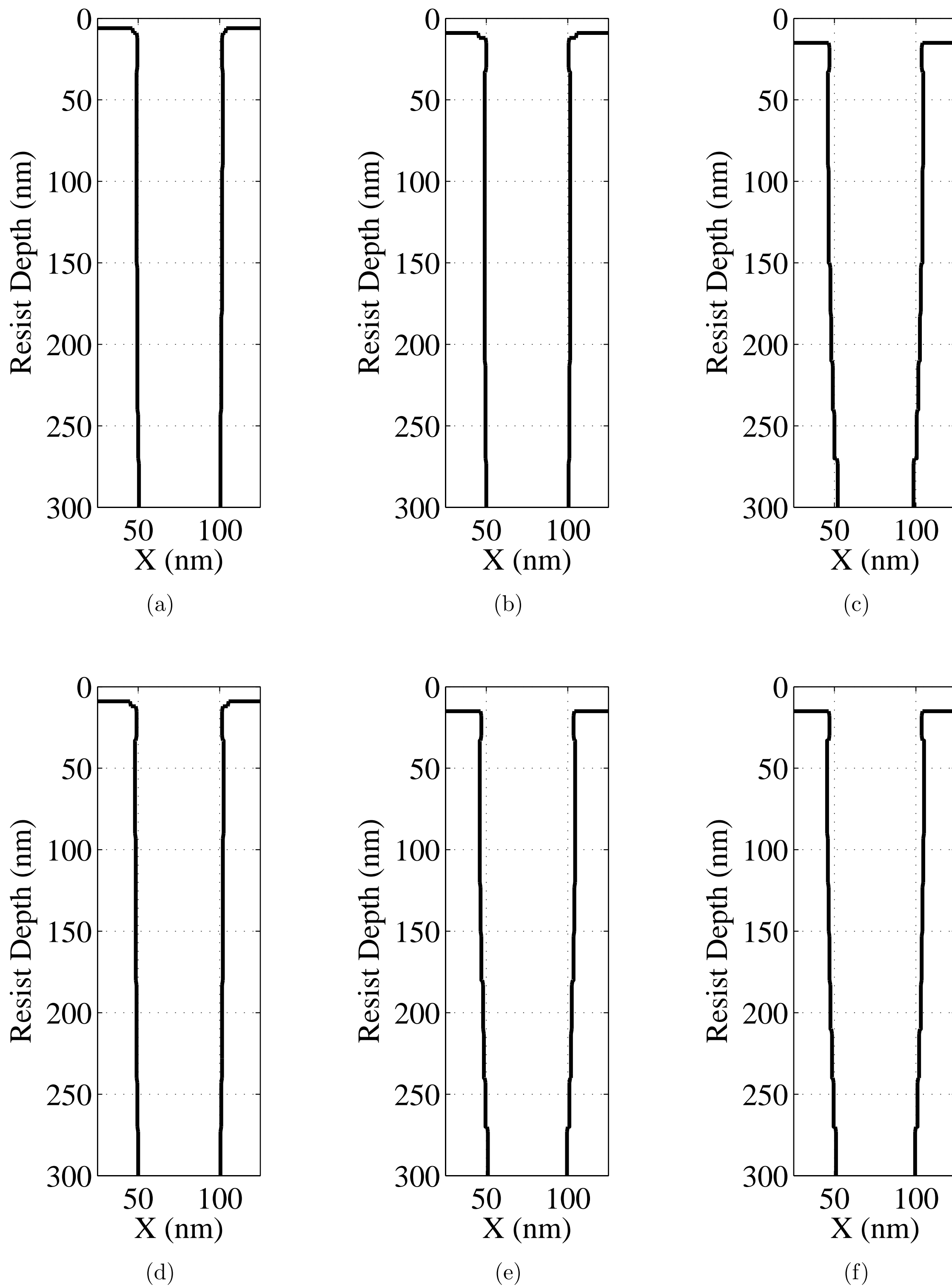

Figure 4.15: Cross-section resist profiles achieved by 3-D PEC method at the critical locations ((a) corner, (b) edge and (c) center; refer to Fig. 4.12) and the test locations ((d), (e) and (f); refer to Fig. 4.12).

4.5.3 Performance Comparison

The correction methods are also compared quantitatively in terms of the percent width errors (refer to Section 4.3.2):

$$Average\ Percent\ Width\ Error = \frac{1}{n}\sum_{j=1}^{n}\frac{|p'(j) - q(j)|}{q(j)} \times 100\%, \tag{4.7}$$

and

$$Max\ Percent\ Width\ Error = \max_{j=1}^{n}\frac{|p'(j) - q(j)|}{q(j)} \times 100\%, \tag{4.8}$$

where $p'(j)$ is the width of j-th layer in the final resist profile after correction, $q(j)$ is the target resist profile as defined in Section 4.4.1, and n is the number of resist layers.

The average and maximum percent width errors for Pattern I and Pattern II are provided in Table 4.1 and Table 4.2, respectively. Note that the maximum error reaches 100% in some cases, due to the underdevelopment in resist profiles (e.g., the bottom layer is not developed at all, leading to a zero width). The results show that the errors for the 2-D PEC method are significantly smaller than those when no correction is done (i.e., a uniform dose). More importantly, compared to the 2-D PEC method, the proposed 3-D PEC method further reduces both average and maximum errors greatly.

PMMA Thickness (nm)	No Correction		2-D PEC Method		3-D PEC Method	
	Average (%)	Maximum (%)	Average (%)	Maximum (%)	Average (%)	Maximum (%)
100	5.20	12.33	4.40	8.33	2.33	4.33
300	44.39	100.00	36.07	94.33	8.70	13.17
500	69.08	100.00	65.45	100.00	41.30	60.33

Table 4.1: Average and maximum percent width errors in resist profiles of Pattern I for no correction, 2-D PEC method and 3-D PEC method.

PMMA Thickness (nm)	No Correction		2-D PEC Method		3-D PEC Method	
	Average (%)	Maximum (%)	Average (%)	Maximum (%)	Average (%)	Maximum (%)
100	1.12	1.67	0.50	1.08	0.32	1.00
300	13.90	32.27	10.00	17.00	2.57	4.42
500	45.85	100.00	33.88	100.00	9.50	13.58

Table 4.2: Average and maximum percent width errors in resist profiles of Pattern II for no correction, 2-D PEC method and 3-D PEC method.

From the above tables of errors, it is observed that as the resist thickness increases, the improvement (reduction in the total percent errors) by the proposed method becomes larger. For a thicker resist, the exposure variation along the resist depth dimension is larger, which makes the 2-D PEC method suffer from larger errors since it ignores the variation. Also, the increase of exposure variation makes the resist profile more sensitive to the dose distribution. Therefore, incorporating the estimation of remaining resist profile into the correction procedure can achieve a more realistic correction, which lacks in the 2-D PEC method. When the feature size decreases, the improvement by the proposed method tends to be larger (except for the resist thickness of 500 nm). For the same substrate system, a smaller feature is affected relatively more by the proximity effect and the development process, therefore has a larger room for improvement. However, for a very thick resist, the PEC itself becomes harder for a smaller feature.

4.6 Summary

A new practical method for true 3-D PEC, which can handle large-scale uniform patterns efficiently, has been developed. It performs true 3-D PEC by taking into account the exposure variation along the resist depth dimension (in addition to the lateral dimensions). The cost (error) function employed in correction is not the conventional (2-D) CD error, but the 3-D CD error, i.e., the CD errors at multiple layers of resist are considered. Also, the method incorporates the resist development simulation into the correction procedure to

achieve realistic results. In order to alleviate the computational requirement for large-scale patterns, a critical-location-based correction approach is taken along with the deconvolution surface for deriving the corrected doses for other locations. Through an extensive simulation, it has been shown that the proposed 3-D PEC method can significantly improve correction results, compared to the 2-D PEC method, in terms of resist profile, i.e., not only CD error but also sidewall shape.

Chapter 5

Sidewall Shape Control: Vertical Sidewall

5.1 Introduction

For the most common sidewall shape, i.e., the vertical sidewall, a typical 2-D target exposure distribution is constant within and zero outside a feature. Then the required dose distribution obtained by the deconvolution is of "V-shape," i.e., the dose is highest at the edge and gradually decreases toward the center of a feature. However, our earlier studies have shown that such 2-D PEC does not lead to realistic results especially for nanoscale features and therefore true 3-D PEC is needed [94, 95, 96].

In 3-D PEC, the resist profile estimated through simulation of resist development was employed instead of the exposure distribution, in order to obtain more realistic results. Moreover, it has been demonstrated that in order to minimize any deviation from a target resist profile, a 3-D PEC scheme must check the estimated resist profile during the dose optimization procedure [95]. One practical issue of such an approach to 3-D PEC is that a time-consuming resist development simulation needs to be carried out in each iteration of the dose optimization. Also, it is shown that the dose distribution of "V-shape" is not optimal for realizing a vertical sidewall of the resist profile, especially when the total dose is to be minimized. Note that a higher total dose worsens the charging effect and lengthens the exposing time.

In this chapter, an efficient dose optimization scheme which does not require a direct resist development simulation while achieving a target 3-D resist profile has been developed. The systematic dose updating procedure coupled with the fast resist development simulation makes the dose optimization scheme fast and effective. Besides, an adaptive scheme has been developed which determines the optimal dose distribution type and the minimum of

required total dose based on a given circuit pattern and substrate system settings. The most noteworthy result from this study is that in order to achieve a vertical sidewall of nanoscale feature with the minimum total dose, one has to employ a dose distribution different from the conventional one of "V-shape." Based on our 3-D exposure model and 3-D PEC method, the new dose distributions of "M-shape" and "A-shape" have been derived for achieving the target resist profile of vertical sidewall minimizing the total dose. Through an extensive simulation, they are compared with other distributions, uniform and "V-shape," in terms of deviation from the target resist profile of vertical sidewall.

The rest of the chapter is organized as follows. Details of the conventional and proposed dose distribution types are presented in Section 5.2. The proposed dose optimization scheme and dose determination scheme for single features are described in Section 5.3 and Section 5.4, respectively. The complete correction procedures of sidewall shape control for large-scale uniform patterns and large-scale nonuniform patterns are presented in Section 5.5 and Section 5.6, respectively. Simulation results are discussed in Section 5.7, followed by a summary in Section 5.8.

5.2 Dose Distribution Types

In this chapter, only a single feature of line is considered for simplicity. Suppose that a target written feature is specified by the corresponding resist profile (e.g., line widths at the top, middle and bottom layers) in 3-D PEC. In our simulation model, the line is sufficiently long in the Y-dimension such that the dimensional variation along the Y-dimension may be ignored. Then, one only needs to consider the cross-section of resist profile in the X-Z plane (refer to Fig. 2.5). During correction, at each location (x, y) in a circuit pattern, the cross-section of resist profile needs to be examined. Therefore, $e(x, y, z)$ and $r(x, y, z)$ can be replaced by $e(x, z)$ and $r(x, z)$, respectively.

In order to avoid a high complexity of the optimization procedure and also have a sufficient spatial control of dose distribution, the line feature is partitioned into 5 regions along its length dimension and a dose is determined for each region, as shown in Fig. 5.1.

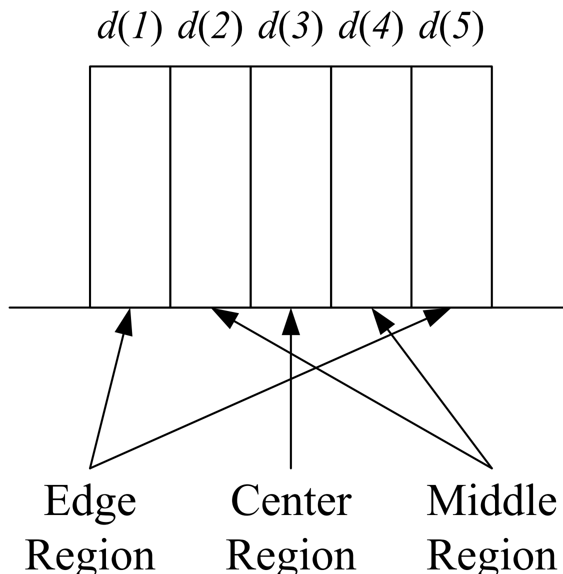

Figure 5.1: The region-wise feature partition with a uniform dose distribution.

The main goal of 3-D PEC is to adjust the spatial distribution of dose in order to minimize the deviation of resist profile from the target one. The focus of this study is on investigating the effectiveness of dose distribution type (shape) in achieving the target resist profile, in particular vertical sidewall.

5.2.1 Conventional Type

A typical shape of spatial dose distribution cross a line feature is such that the dose is highest in the edge regions and gradually decreases toward the center region (to be referred to as Type-V according to its shape). This type of dose distribution is usually obtained by an exposure-based correction where a target 2-D exposure distribution is specified (to be referred to as 2-D exposure correction [96]).

In the 2-D exposure model, the exposure is assumed not to vary along the resist depth dimension (Z-dimension), i.e., $e(x, z)$ in the cross-section is averaged over $0 \leq z \leq H$ (refer

to Fig. 2.4), resulting in $e(x)$. Let $h(x)$ represent the depth distribution (i.e., depth at x) in the target resist profile. A target exposure distribution $E_t(x)$ is derived from $h(x)$ by:

$$E_t(x) = F^{-1}[\frac{h(x)}{T}], \tag{5.1}$$

where T is the developing time.

The exposure $E_t(x)$ can be considered as a threshold for a certain point to be fully developed. Therefore, the objective of this 2-D exposure correction is to control the dose distribution $d(x)$ such that $e(x)$ is as high as the threshold $E_t(x)$ in the exposed area, and as low as possible in the unexposed area, i.e., ideally a rectangular window function with width of the feature size and height of $E_t(x)$ (refer to Fig. 5.2).

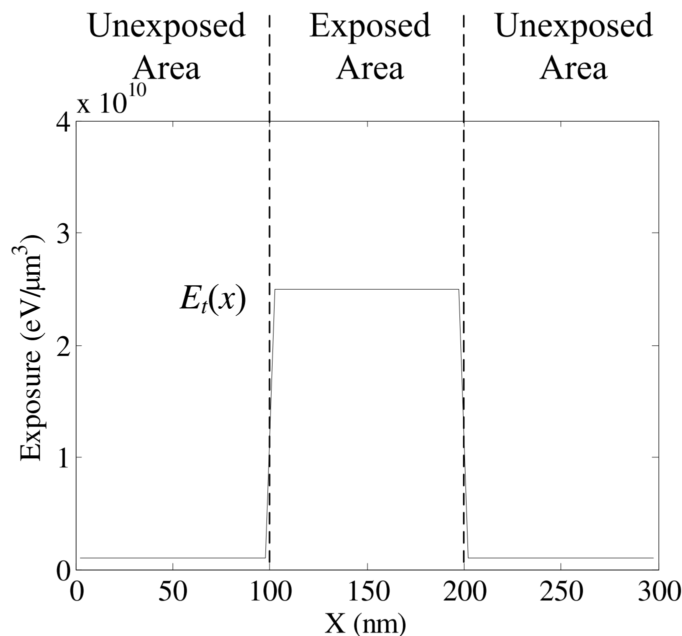

Figure 5.2: The target 2-D exposure distribution is illustrated for a line feature.

Then, the dose distribution $d(x)$ required to achieve this kind of $e(x)$ can be determined through iterations of dose adjustment, or equivalently deconvolution of $e(x)$ with the PSF. In general, $d(x)$ derived from deconvolution of a rectangular window function with the PSF is of Type-V.

The Type-V dose distribution seems quite reasonable according to the above analysis. However, when the feature size decreases into nanoscale, it usually results in an undesired 3-D resist profile in terms of CD error and sidewall shape, and requires a relatively higher total dose for full development (refer to Section 5.2.2 for more details).

This is mainly due to the drawbacks of the 2-D exposure correction. Most importantly, in the 2-D model, the exposure variation along the resist depth dimension is not taken into account while the resist profile depends on the variation to great extents. Also, the actual resist profile cannot be derived directly from the exposure distribution, e.g., the resist profile derived from the above-mentioned exposure distribution (a rectangular window function) cannot have a vertical sidewall. The 2-D exposure correction does not consider the resist development process and therefore is likely to end up with an unrealistic result. For example, the lateral development of resist, which significantly affects the resist profile in particular the sidewall shape of fine features, is not taken into account in the 2-D exposure correction.

5.2.2 Proposed Types

In order to overcome the drawbacks of the 2-D exposure correction, a resist-profile-based correction was developed along with a 3-D model (to be referred to as 3-D resist profile correction [96]). Unlike the above 2-D exposure correction, this 3-D correction incorporates the estimation of remaining resist profile into the correction procedure and utilizes the resist profile to determine the dose distribution based on a 3-D model. The overall correction procedure is similar to that of the 2-D correction. However, the error, which is to be minimized determining the corrected dose distribution, is computed based on the estimated remaining resist profile rather than the exposure distribution, and is given by:

$$Error = \max_{j} |p(j) - q(j)|, \tag{5.2}$$

where $p(j)$ and $q(j)$ denote the width distribution of the estimated remaining resist profile and that of the target resist profile, respectively (refer to Fig. 5.3).

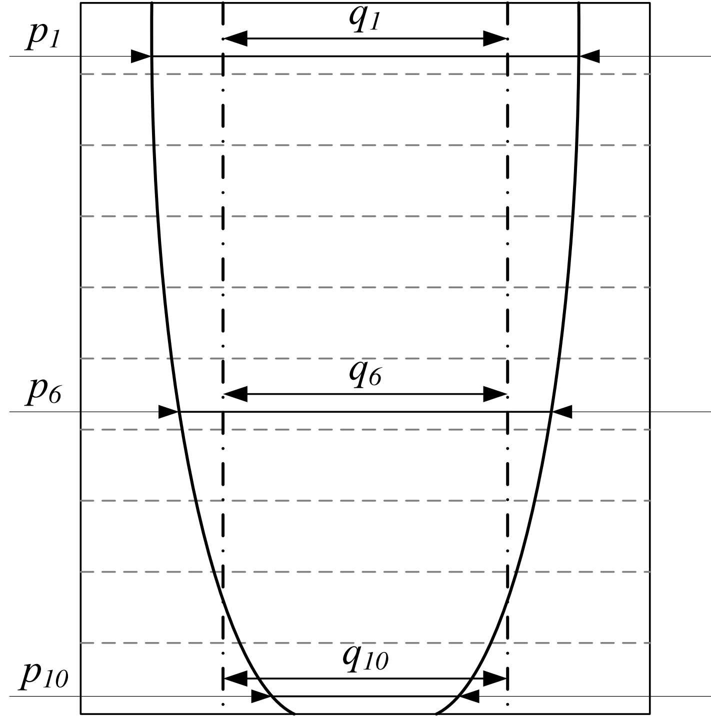

Figure 5.3: The cross-section of resist profile is illustrated for a line feature where p_j and q_j are the actual and target widths at the j-th layer, respectively, where the resist is modeled by 10 layers.

Based on the 3-D resist profile correction, two other types of dose distributions are proposed and analyzed in order to achieve a target resist profile with the minimal total dose. The two new dose distribution types are one with the highest dose in the two middle regions (to be referred to as Type-M according to its shape) and the other with the highest dose in the center region and monotonically decreasing toward the edge regions (to be referred to as Type-A according to its shape).

The effectiveness of the Type-M and Type-A dose distributions in achieving a vertical sidewall stems from the 3-D distributions of exposure that they result in. In Section 3.3.3, it was noticed that the distribution of exposure along the resist depth dimension behaves quite differently between the exposed area and the unexposed area, as shown in Fig. 5.4(a) and Fig. 5.4(b). For the exposed area, the exposure usually decreases along the resist depth dimension, while it changes abruptly to an increasing behavior in the unexposed area.

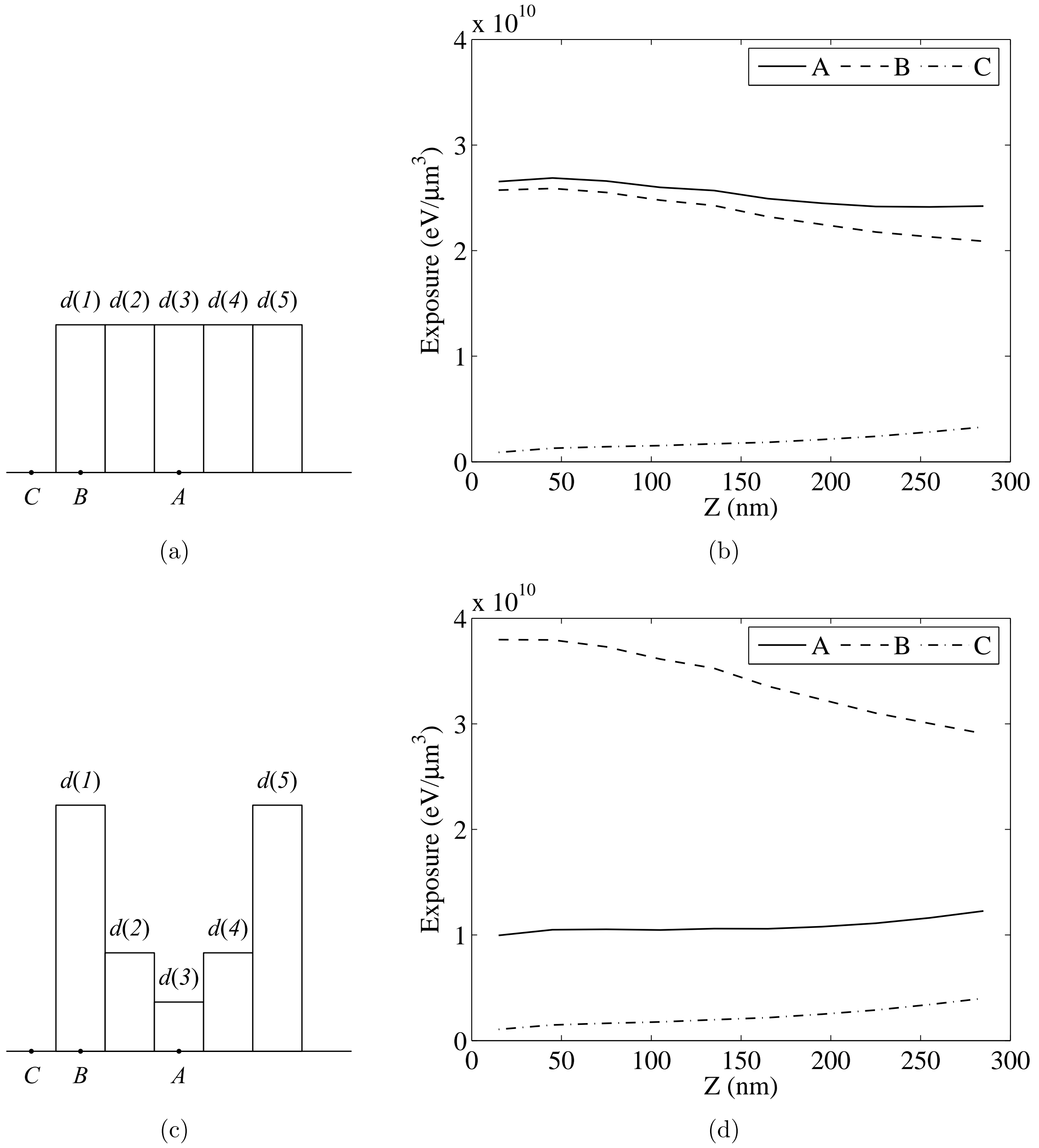

Figure 5.4: Comparison of (a) the uniform dose distribution and (b) the corresponding distribution curves of 3-D exposure along Z-dimension (resist depth), with (c) a non-uniform dose distribution and (d) the corresponding distribution curves of 3-D exposure along Z-dimension (resist depth) at three points (A, B, and C) on the substrate system of 300 nm PMMA on Si.

For a given point x_i, the distribution of its self-exposure (denoted as $e_s(x_i, z)$) decreases along the resist depth dimension. But the distribution of the sum of exposure contributions from its neighboring points (denoted as $e_o(x_i, z)$) increases along the resist depth dimension.

It is obvious that the overall behavior of exposure distribution for that point, i.e., $e(x_i, z) = e_s(x_i, z) + e_o(x_i, z)$, depends on the dose distribution. If the region which the point belongs to has a relatively lower dose while its neighboring regions have high doses, then $e_o(x_i, z)$ becomes the dominant component and $e(x_i, z)$ tends to increase with z, and vice versa (refer to Fig. 5.4(c) and Fig. 5.4(d)).

Based on this observation, the resist developing behaviors of different dose types can be analyzed, which are shown in Figs. 5.5, 5.6, and 5.7 where a thicker arrow corresponds to a higher developing rate. The developing time is given by T, while T_1 and T_2 are two intermediate points in time with $T_1 < T_2 < T$.

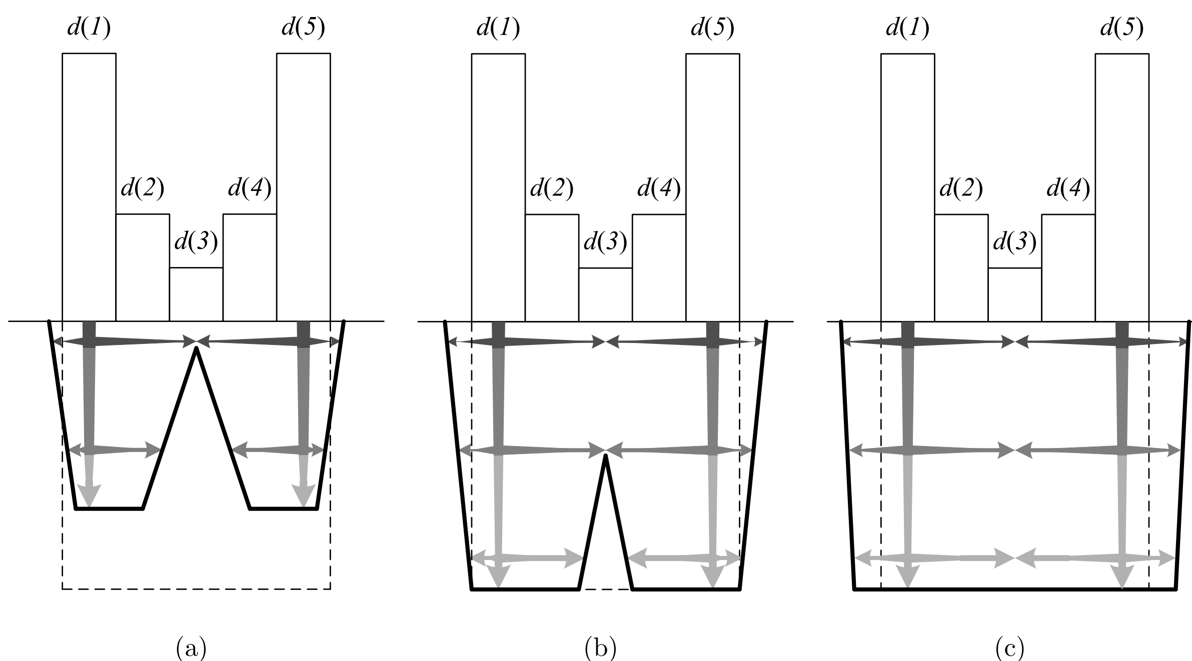

Figure 5.5: The resist profile during development process (a) at time T_1, (b) at time T_2, and (c) at time T for Type-V case, respectively, where $T_1 < T_2 < T$.

For the vertical sidewall shape, take the Type-A dose distribution for an example (also refer to Fig. 5.7). The top layer of resist develops earlier than the bottom layer of resist in the center region. However, the exposure distribution of the edge and middle regions increases in the Type-A. As a result, the developing rate of the bottom layer of resist is higher than that of the top layer for the edge and middle regions. Therefore, when the developer reaches

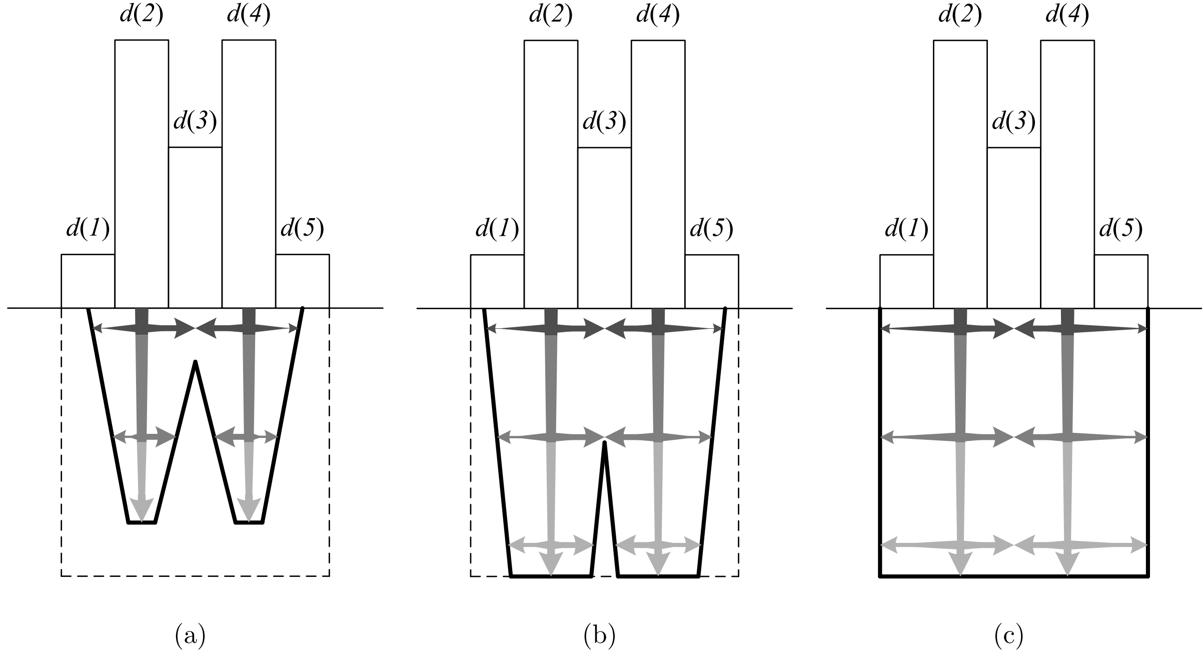

Figure 5.6: The resist profile during development process (a) at time T_1, (b) at time T_2, and (c) at time T for Type-M case, respectively, where $T_1 < T_2 < T$.

the bottom layer of resist and begins to develop laterally from the center region toward the edge regions, it finally catches up with the developing process of the top layer of resist at the boundaries of the feature (the boundaries between the exposed area and the unexposed area) and achieves a vertical sidewall. Note that the exposure distribution in the top layer has a larger contrast over the feature boundaries.

From Fig. 5.5, it is also seen that the Type-V cannot achieve the target vertical sidewall. In the Type-V, the top layer of resist always develops earlier than the bottom layer of resist within the edge regions. As a result, the developing process of the bottom layer of resist can never catch up with that of the top layer before reaching the boundaries, thus resulting in an overcut sidewall. This problem may be solved by introducing shape correction, i.e., exposing an area smaller than the feature. However, in that way, the Type-V becomes an implicit version of the Type-M. Another solution is to give a higher total dose for the Type-V case to let the bottom layer develop longer, which however requires a higher total dose and tends to make the width of written feature greater than the target width.

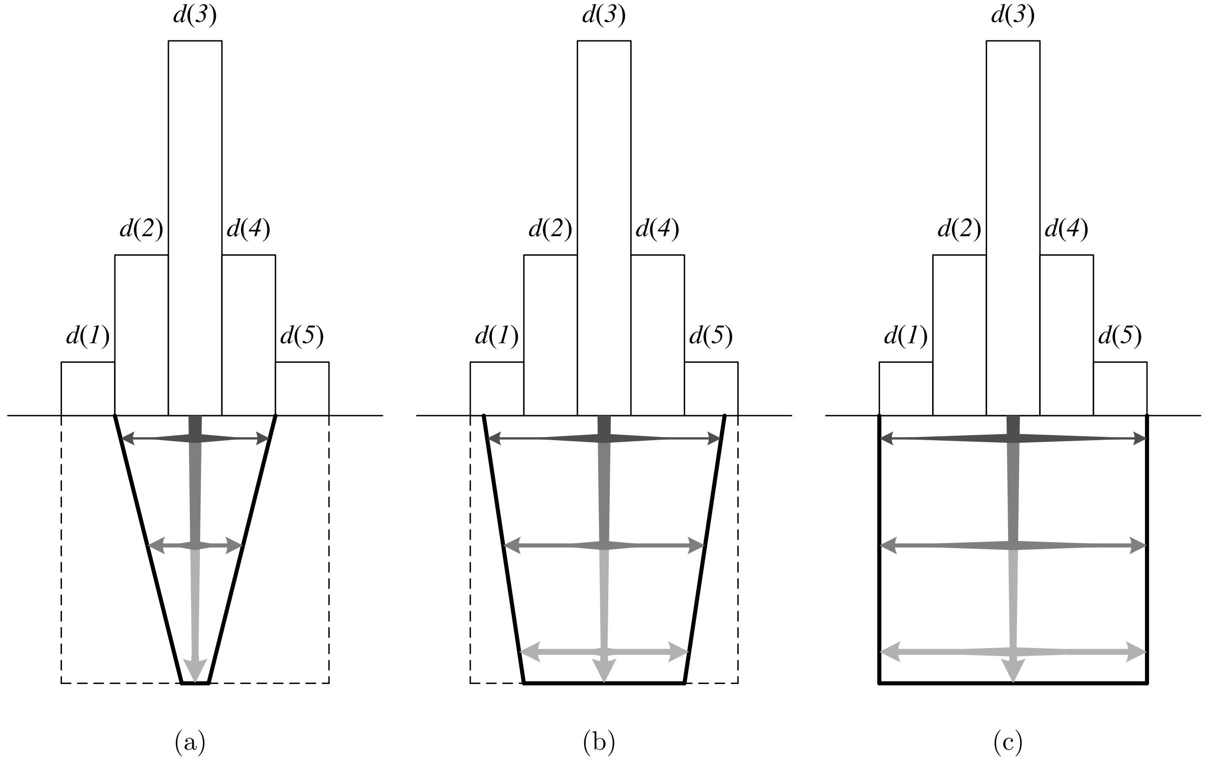

Figure 5.7: The resist profile during development process (a) at time T_1, (b) at time T_2, and (c) at time T for Type-A case, respectively, where $T_1 < T_2 < T$.

Note that the new finding of Type-M and Type-A dose distributions would not have been possible without using our 3-D exposure model and 3-D PEC method.

5.3 Dose Optimization Scheme

An efficient iterative optimization scheme has been developed which derives the dose distribution of each type minimizing the deviation from the target resist profile, i.e., vertical sidewall, and total dose. Each iteration consists of three steps: fast exposure computation, critical-path-based resist development simulation, and type-based dose updating.

5.3.1 Fast Exposure Computation

In the first step, the three base exposures (region-wise) $(e_i(x, z) \mid i = 1, 2, 3)$ are precalculated using the 3-D exposure model (refer to Section 2.3).

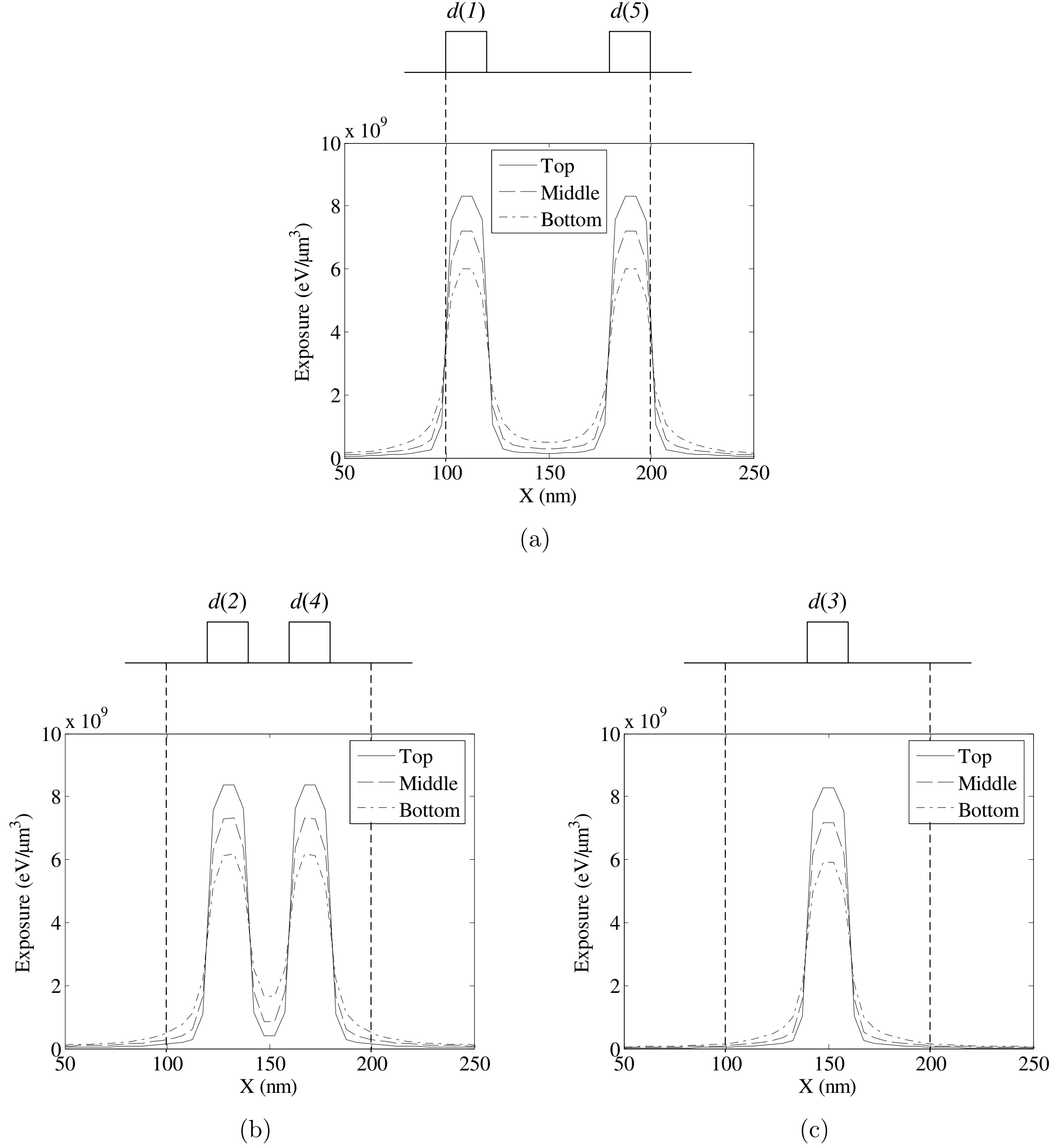

Figure 5.8: The exposure distribution of the top, middle and bottom layers of resist when only (a) the two edge regions, (b) the two middle regions, and (c) the center region are exposed with a unit dose.

Note that $e_i(x, z)$ is the exposure when a unit dose is given only to the i-th and $(6-i)$-th regions, i.e., $d(i) = 1.0$ and $d(6 - i) = 1.0$ while the other regions are not exposed (refer to Fig. 5.8).

The total exposure $e(x, z)$ can be computed by:

$$e(x, z) = \sum_{i=1}^{3} d(i) \cdot e_i(x, z), \tag{5.3}$$

where $d(i)$ is the actual dose distribution given to the the i-th region. The exposure is then converted into developing rate through Eq. 2.4.

5.3.2 Critical-path-based Resist Development Simulation

The main goal is to achieve the minimal deviations from the target 3-D resist profile at the top, middle and bottom layers of resist. Therefore, in the second step, the simulation of resist development process is employed to generate the resist profile.

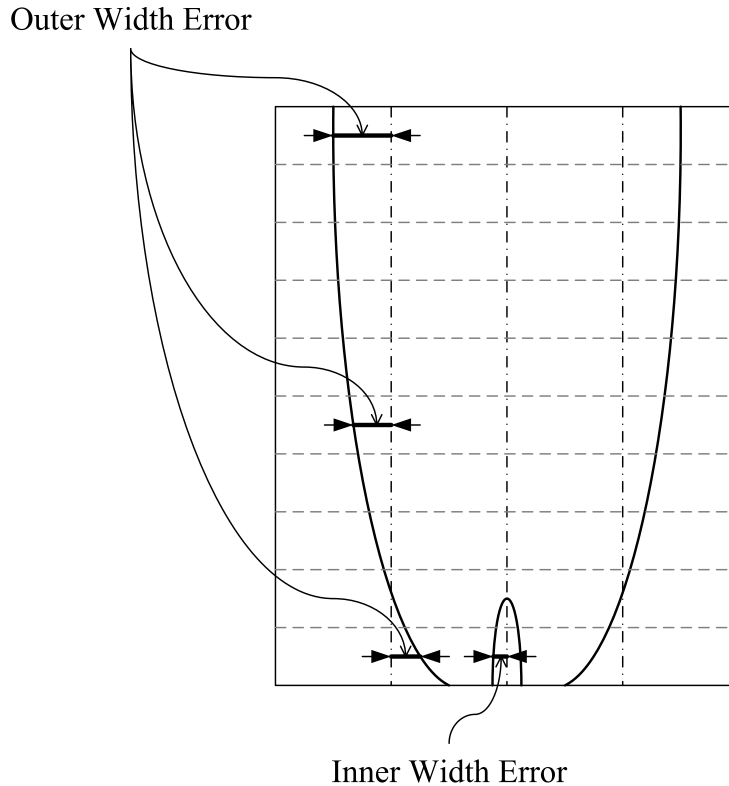

Figure 5.9: The outer width errors and the inner width errors defined at the cross-section of resist profile.

For this stage, it is not required to run the whole simulation to get a complete resist profile since only the widths at the top, middle and bottom layers of resist need to be considered. Therefore, our path-based method (refer to Section 2.4) is further simplified by

tracing the developing process along several critical paths required to obtain those desired widths only.

Note that the critical paths are not fixed but depend on the specific dose distribution type (refer to Figs. 5.5, 5.6, and 5.7).

Then, the width information derived are used for computing width errors. The width errors are defined at the top, middle and bottom layers of resist (refer to Fig. 5.3). One improvement is that, besides the outer width error (deviation from the feature boundary), now the inner width error (deviation from the feature centerline) is also defined, as shown in Fig. 5.9. These errors are measured for each layer in order to guarantee not only CD error and sidewall shape but also fully-developed condition.

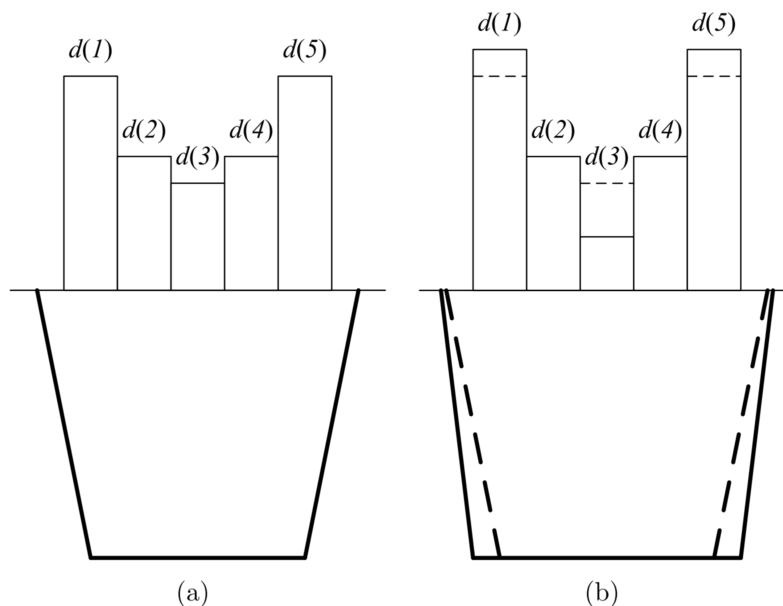

Figure 5.10: The resist profile (a) before dose updating and (b) after dose updating for Type-V case, respectively.

5.3.3 Type-based Dose Updating

In the third step, the dose of each region is updated based on the current resist profile. Depending on the relationship among the width errors (positive or negative, larger or smaller, etc.), the dose either increases or decreases. The overall dose updating mechanism is common

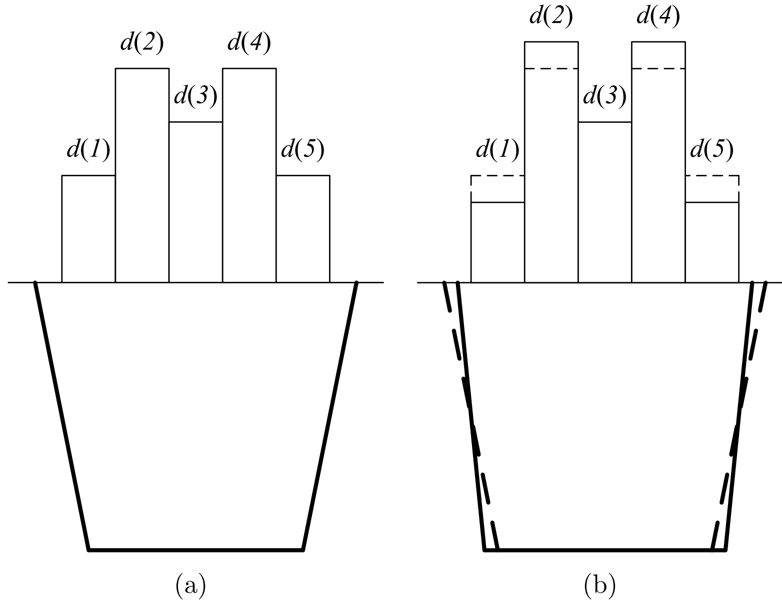

Figure 5.11: The resist profile (a) before dose updating and (b) after dose updating for Type-M case, respectively.

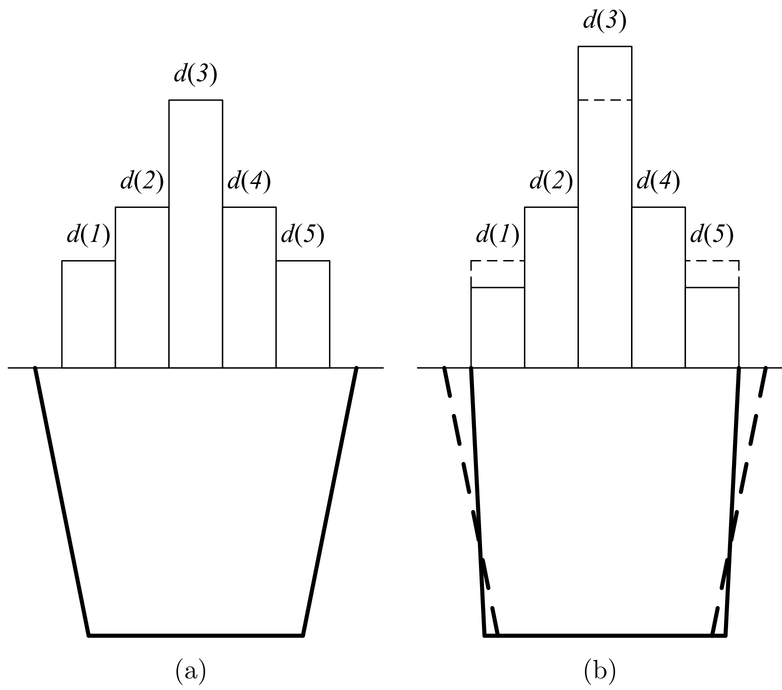

Figure 5.12: The resist profile (a) before dose updating and (b) after dose updating for Type-A case, respectively.

for different dose distribution types (Type-V, Type-M, Type-A), but the details are different.

The dose distribution is adjusted such that it is guided toward a given type and the maximum of the width errors is minimized.

For example, if the current resist profile has a positive outer width error in the top layer but a negative outer width error in the bottom layer (refer to Fig. 5.9), i.e., an overcut sidewall, and intersects with the feature boundary, the dose of the two edge regions increases in the Type-V while it decreases in the Type-M or Type-A (refer to Figs. 5.10, 5.11, and 5.12). In this way, the dose distribution can be guided toward the preset dose distribution type. The procedure goes back to the first step and continues through iterations until the maximum of the width errors is smaller than a certain threshold.

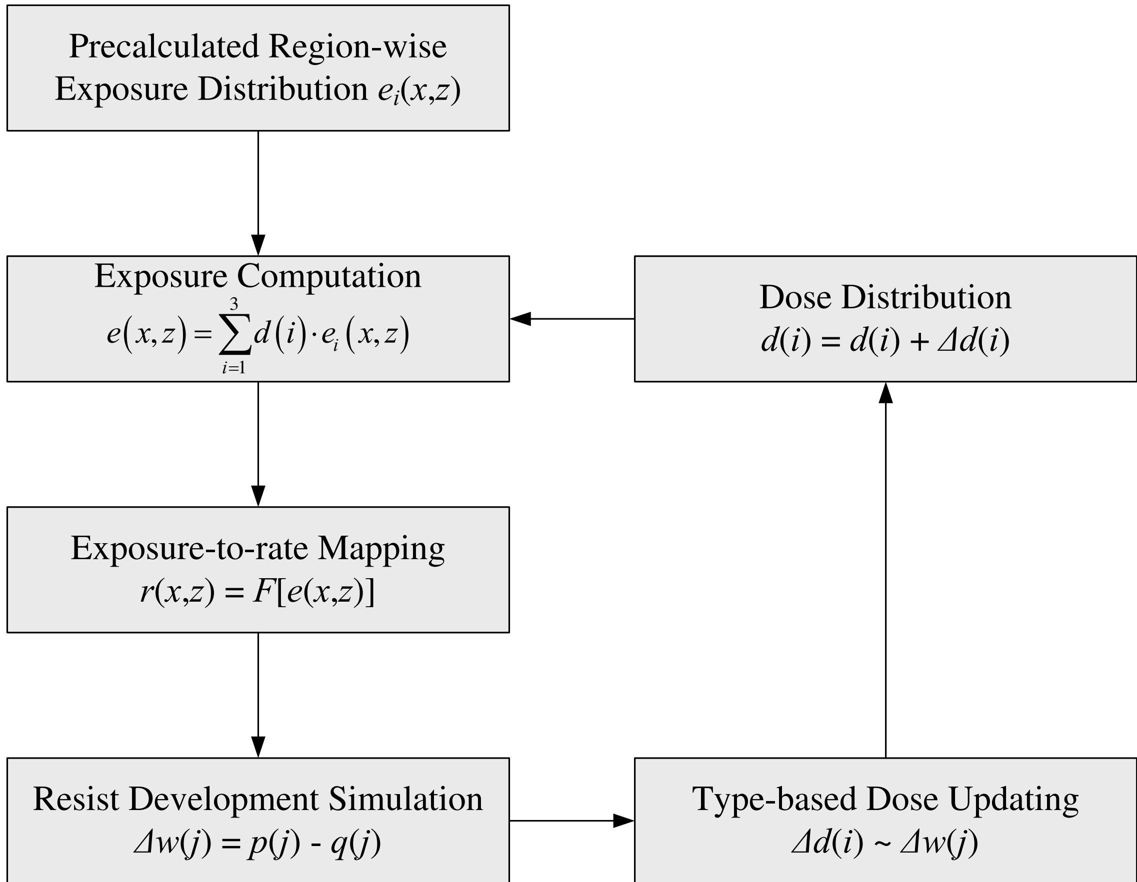

Figure 5.13: Flowchart of the proposed dose optimization scheme.

Note that since the base exposures are precalculated, the cost for exposure computation in the first step during iterations can be greatly reduced. Also, the critical-path-based

method in the second step saves a lot of simulation time for the resist development process. These improvements make the proposed dose optimization scheme (also refer to the flowchart in Fig. 5.13) an effective and efficient alternative to the conventional PEC approach.

5.4 Dose Determination Scheme

An adaptive scheme has been developed which determines the optimal dose distribution type (Type-V, Type-M, Type-A) and the minimum of required total dose based on a given circuit pattern and substrate system settings. The proposed scheme utilizes the concept of critical path in dose determination.

First, a preset region-wise dose ratio $q(i)$, i.e., $d(1) : d(2) : d(3) : d(4) : d(5)$, is employed for each dose distribution type, which is set to $4 : 2 : 1 : 2 : 4$ for Type-V, $1 : 5 : 1 : 5 : 1$ for Type-M, and $1 : 2 : 7 : 2 : 1$ for Type-A.

Note that this dose ratio is only used to determine the best dose distribution type and minimum total dose, but not the actual dose distribution (actual dose ratio) for correction which is determined by the proposed dose optimization scheme.

The total exposure $e(x, z)$ can be computed by:

$$e(x,z) = \frac{D \cdot \sum_{i=1}^{3} q(i) \cdot e_i(x,z)}{\sum_{i=1}^{5} q(i)}, \tag{5.4}$$

where $e_i(x, z)$ are the base exposures (refer to Section 5.3.1) and D is an initial total dose. The exposure is then converted into developing rate through Eq. 2.4.

Then, those developing rates along a specific critical path are used to compute the required developing time. The critical path is defined as the developing path in the resist development process which plays the most important role in determining the resist profile, as illustrated in Fig. 5.14.

Note that the critical path is different for each dose distribution type (Type-V, Type-M, Type-A). For example, in the Type-V case, the critical path starts from one of the edge regions at the top layer of resist, then goes vertically down to the bottom layer of resist, then goes laterally toward the center and stops at the center point of the exposed area (also refer to Fig. 5.14(a)). But in the Type-A case, the critical path starts from the center region at the top layer of resist, then goes vertically down to the bottom layer of resist, then goes laterally toward the left (right) and stops at the boundary between the exposed area and unexposed area (also refer to Fig. 5.14(c)).

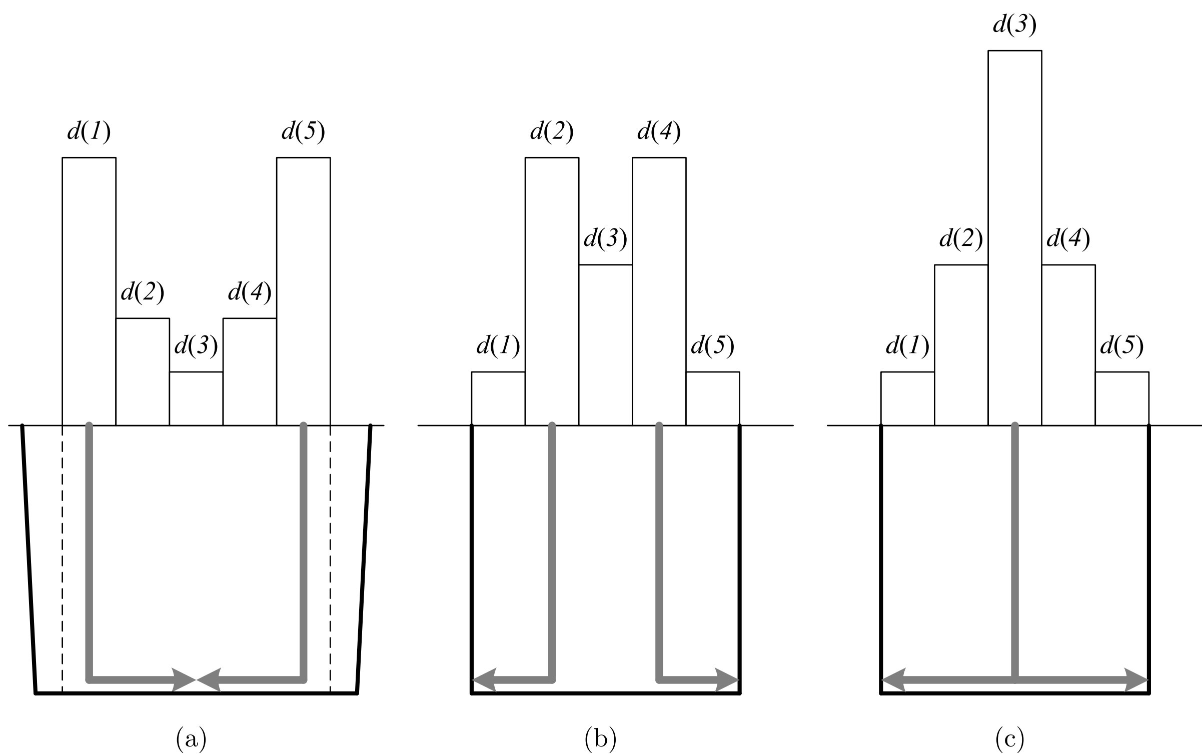

Figure 5.14: The critical path for (a) Type-V case, (b) Type-M case, and (c) Type-A case, respectively.

The total dose D is updated such that the required developing time T spent on the critical path in the resist is no larger than the given developing time T_0 (the one specified for correction). The solved total dose which satisfies this developing time condition is the minimum of required total dose for a specific dose distribution type.

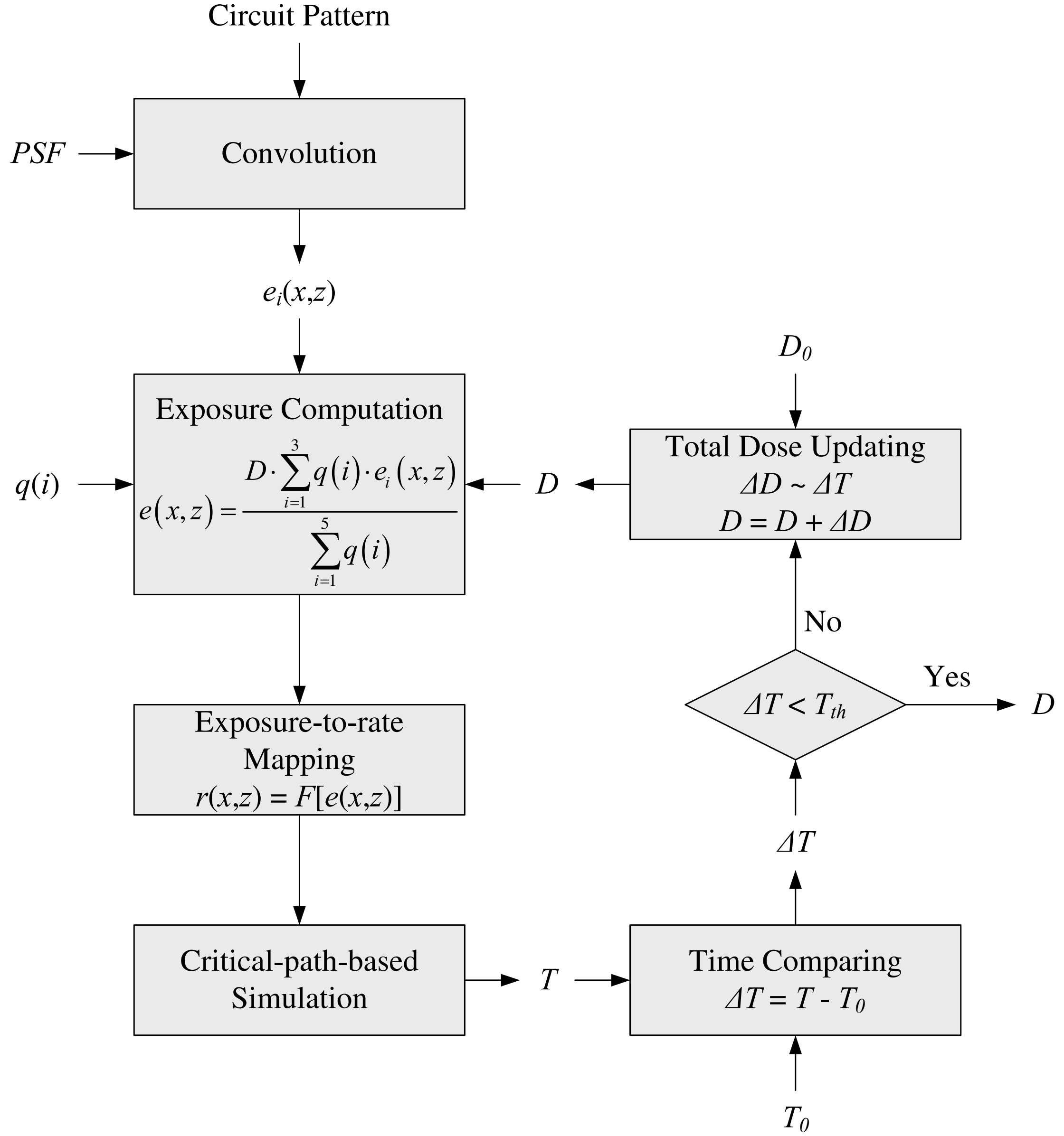

Figure 5.15: Flowchart of the proposed dose determination scheme for a specific dose distribution type.

The complete determination procedure for a specific dose distribution type is depicted below (also refer to the flowchart in Fig. 5.15).

Step 1: Calculate the three region-wise base exposures $e_i(x, z)$, and set an initial value D_0 for the total dose D.

Step 2: Compute the total exposure $e(x, z)$ using the total dose D, the region-wise base exposures $e_i(x, z)$, and the preset region-wise dose ratio $q(i)$.

Step 3: Convert the total exposure $e(x, z)$ into developing rate $r(x, z)$ through the conversion formula in Eq. 2.4.

Step 4: Perform the critical-path-based simulation to derive the required developing time T.

Step 5: Compare the required developing time T with the given developing time T_0 to obtain ΔT by $\Delta T = T - T_0$.

Step 6: If ΔT is smaller than a certain threshold T_{th}, proceed to Step 7. Otherwise, update the total dose D by $D = D + \Delta D$ where ΔD is qualitatively based on ΔT, then go back to Step 2.

Step 7: Output the total dose D as the minimum of required total dose.

Finally, the minimum of required total dose from each of the three dose distribution types are compared and the type which requires the lowest of minimum total dose is determined to be the best type.

Note that the output of this dose determination scheme is the best dose distribution type with its minimum of required total dose, which can be used for the proposed dose optimization scheme, thus makes the whole scheme more adaptive and efficient (also refer to the flowchart in Fig. 5.16) and provides an alternative way to the conventional time-consuming trial-and-error scheme.

5.5 Sidewall Shape Control for Large-scale Uniform Patterns

For a large-scale uniform pattern, the proximity effect is significant due to a very high pattern density. Therefore, it is necessary to develop a correction procedure by considering each dose distribution type to handle the increased background exposure. The proposed

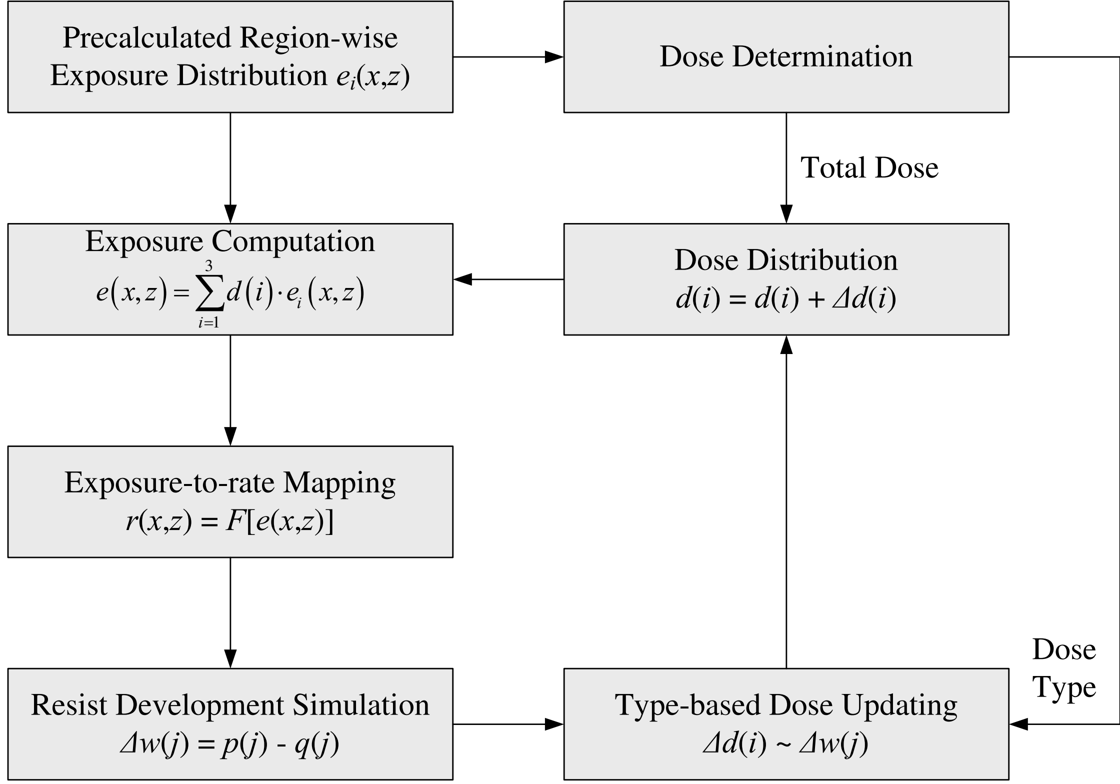

Figure 5.16: Flowchart of the improved dose optimization scheme with the proposed dose determination scheme.

dose optimization scheme is incorporated into the critical-location-based 3-D PEC method (refer to Section 4.4).

The complete correction procedure is depicted below (also refer to the flowchart in Fig. 5.17).

Step 1: A single instance of the repeated feature in the pattern is corrected in isolation (refer to Section 4.4.1). The feature is partitioned into regions where the region-wise dose distribution $d(i)$ is determined using the proposed dose optimization scheme (refer to Section 5.3).

Step 2: The global distribution of feature-wise dose throughout the pattern (deconvolution surface $A(m,n)$) is derived by a 2-D deconvolution of the target exposure distribution $E_t(m,n)$ with the normalized PSF (refer to Section 4.4.2).

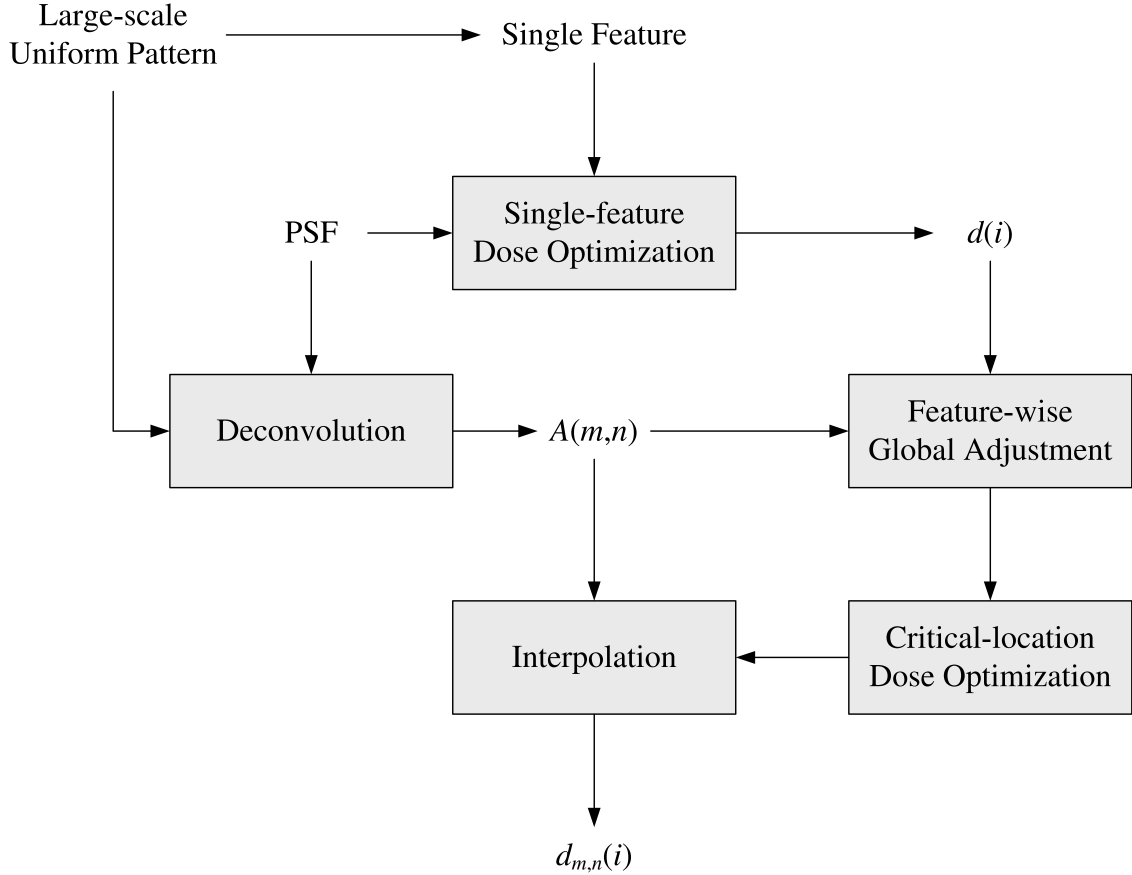

Figure 5.17: Flowchart of the correction procedure for large-scale uniform patterns.

Step 3: For the m, n-th location of the pattern, $d(i)$ is weighted (scalar multiplication) by the deconvolution surface $A(m, n)$, i.e., $d_{m,n}(i) = d(i) \cdot A(m, n)$ (refer to Section 4.4.2).

Step 4: A critical-location-based correction is performed at the corner, edge, and center locations of the pattern (refer to Section 4.4.3). The region-wise dose distribution $d_{m,n}(i)$ at each of the three critical locations is adjusted using the proposed dose optimization scheme (refer to Section 5.3).

Step 5: A 2-D global interpolation is employed to compute the $d_{m,n}(i)$ at all other locations based on the deconvolution surface $A(m, n)$ (refer to Section 4.4.3).

5.6 Sidewall Shape Control for Large-scale Nonuniform Patterns

For a large-scale nonuniform pattern, the correction is more difficult than the uniform pattern case. One issue is that there is more than one type of features in a nonuniform pattern. Another issue is that the pattern density varies through a nonuniform pattern, which makes the global distribution of feature-wise dose required for correction not as smooth as in the uniform pattern case.

In order to address the above issues, the proposed 3-D PEC method (refer to Section 4.4) is extended to correction of large-scale nonuniform patterns. The major modification is that the conventional feature-by-feature correction procedure have to be employed instead of the proposed critical-location-based correction procedure. However, the same kind of dose adjustment procedure can still be maintained for the nonuniform pattern case, i.e., adjusting dose distribution to make the difference in the internal exposure compensate for that in the background exposure such that the deviation from the target resist profile is minimized for all the features (refer to Section 4.4.3). Our 3-D PEC program is also improved such that it can correct both X-dimension and Y-dimension of each feature using 1-D region-wise dose control. Then the final 2-D region-wise dose distribution is mathematically interpolated from the two 1-D region-wise dose distributions for X-dimension and Y-dimension.

The complete correction procedure is depicted below (also refer to the flowchart in Fig. 5.18).

Step 1: The global distribution of feature-wise dose throughout the pattern (deconvolution surface $A(m,n)$) is derived by a 2-D deconvolution of the target exposure distribution $E_t(m,n)$ with the normalized PSF (refer to Section 4.4.2).

Step 2: For the m,n-th location of the pattern, a given total dose D is weighted (scalar multiplication) by the deconvolution surface $A(m,n)$, i.e., $D(m,n) = D \cdot A(m,n)$.

Step 3: A feature-by-feature correction is performed at each location. The region-wise dose distribution in X-dimension and Y-dimension, i.e., $d_{m,n}(x)$ and $d_{m,n}(y)$, are adjusted

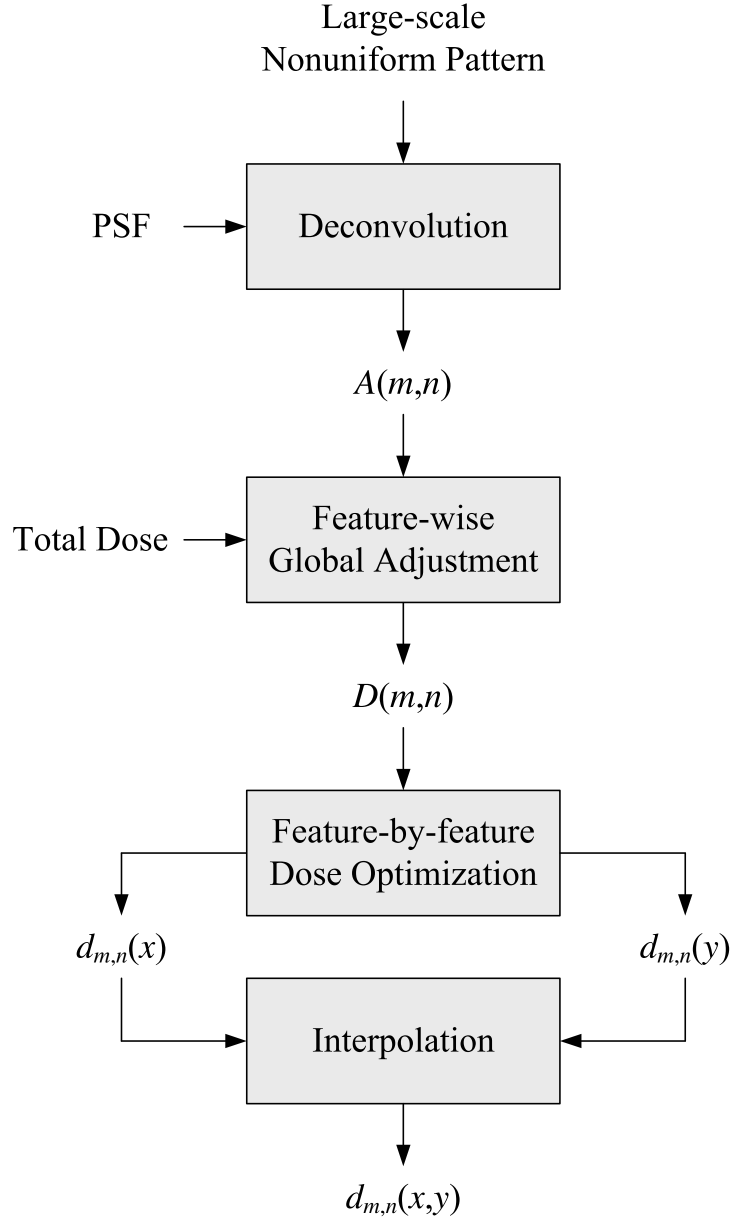

Figure 5.18: Flowchart of the correction procedure for large-scale nonuniform patterns.

independently using the proposed dose optimization scheme (refer to Section 5.3 and Fig. 5.19). Note that $\sum_{x=1}^{R} d_{m,n}(x) = \sum_{y=1}^{R} d_{m,n}(y) = D(m,n)$.

Step 4: A 2-D interpolation is employed to compute the 2-D region-wise dose distribution $d_{m,n}(x,y)$ at each location based on the two 1-D region-wise dose distributions $d_{m,n}(x)$ and $d_{m,n}(y)$, which is given by (also refer to Fig. 5.20):

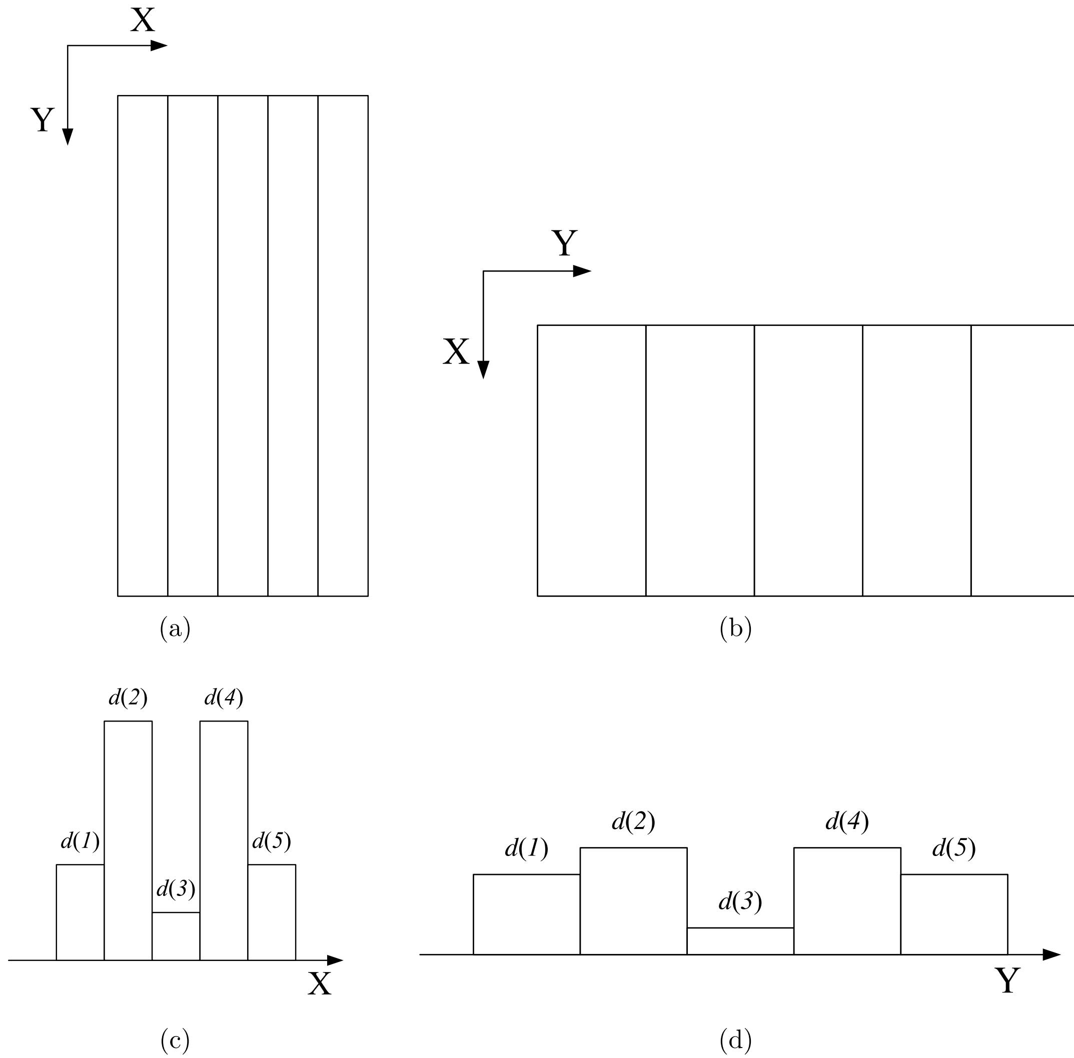

Figure 5.19: A feature is partitioned into 5 regions (a) along X-dimension and (b) along Y-dimension, respectively. The region-wise dose distribution (c) in X-dimension ($d_{m,n}(x)$) and (d) in Y-dimension ($d_{m,n}(y)$) after correction, respectively.

$$d_{m,n}(x,y) = \frac{d_{m,n}(x) \cdot d_{m,n}(y)}{D(m,n)}. \tag{5.5}$$

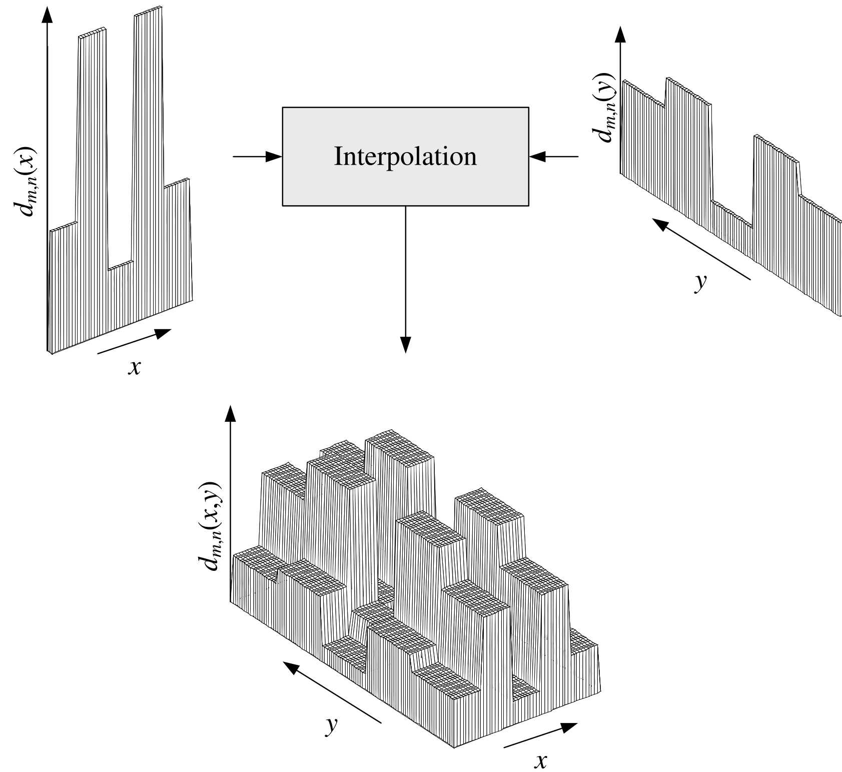

Figure 5.20: Illustration of the 2-D interpolation for computing the 2-D region-wise dose distribution $d_{m,n}(x, y)$.

5.7 Results and Discussion

5.7.1 Performance Comparison for Single Features

The effectiveness of different dose distribution types (Type-V, Type-M, Type-A) in achieving a vertical sidewall, using the proposed dose optimization scheme and dose determination scheme, have first been analyzed for single features. The PSFs used in the simulation are generated by a Monte Carlo simulation method, SEEL [111]. The substrate systems employed in the simulation are composed of PMMA on Si where the three different PMMA thicknesses, 100 nm, 300 nm, and 500 nm, are considered. The beam energy is set to 50 KeV with the beam diameter of 5 nm. Two different widths of a single-line feature are considered for performance analysis, i.e., 50 nm and 100 nm, and the length of line is fixed

to 3 μm. These three substrate systems along with the two feature sizes provide six different combinations so that the proposed scheme can be thoroughly tested.

The line features are corrected with the three dose distribution types, i.e., Type-V, Type-M, and Type-A, for the target resist profile of vertical sidewall. The simulation results for no correction (a uniform dose distribution) and correction using different dose distribution types are compared in terms of resist profile with a constraint that the total dose must be the same for all the cases. The results (cross-section resist profiles) for feature size of 100 nm are provided in Figs. 5.21, 5.22, and 5.23.

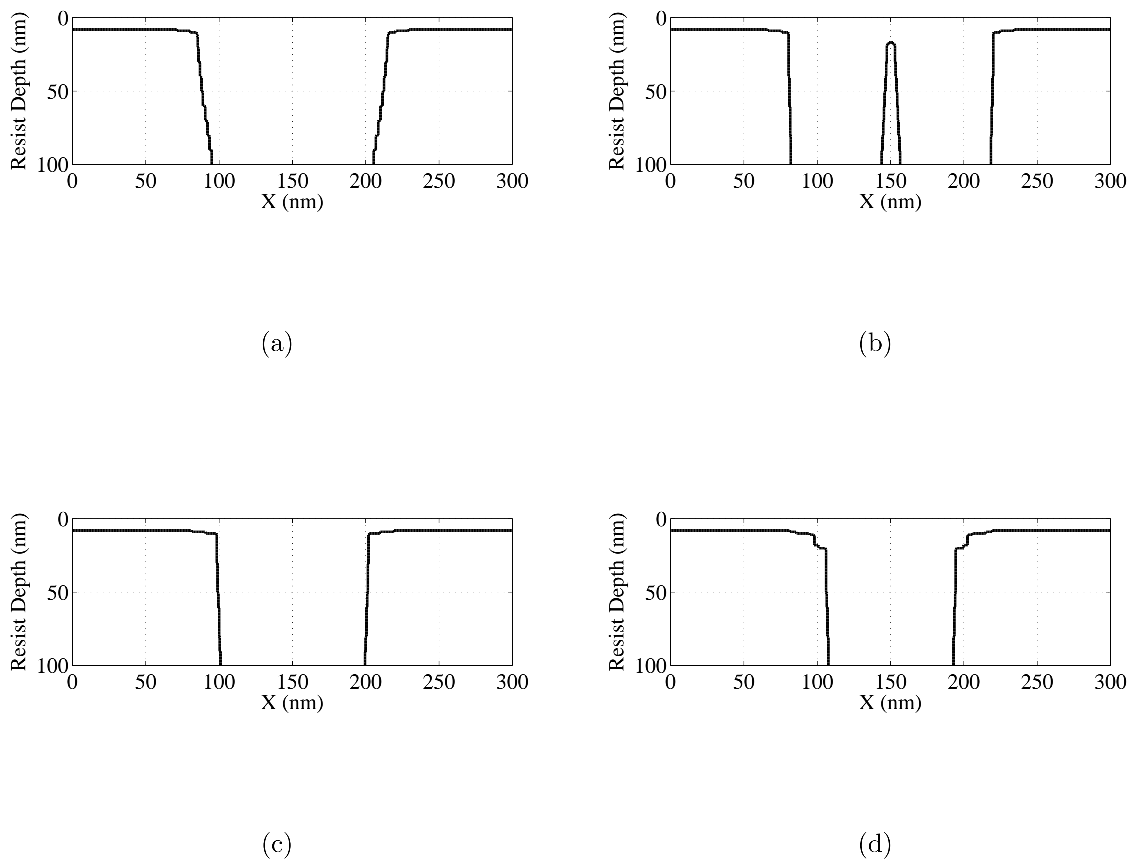

Figure 5.21: Cross-section resist profiles: (a) the uniform dose distribution, (b) the Type-V dose distribution, (c) the Type-M dose distribution, and (d) the Type-A dose distribution on the substrate system of 100 nm PMMA on Si.

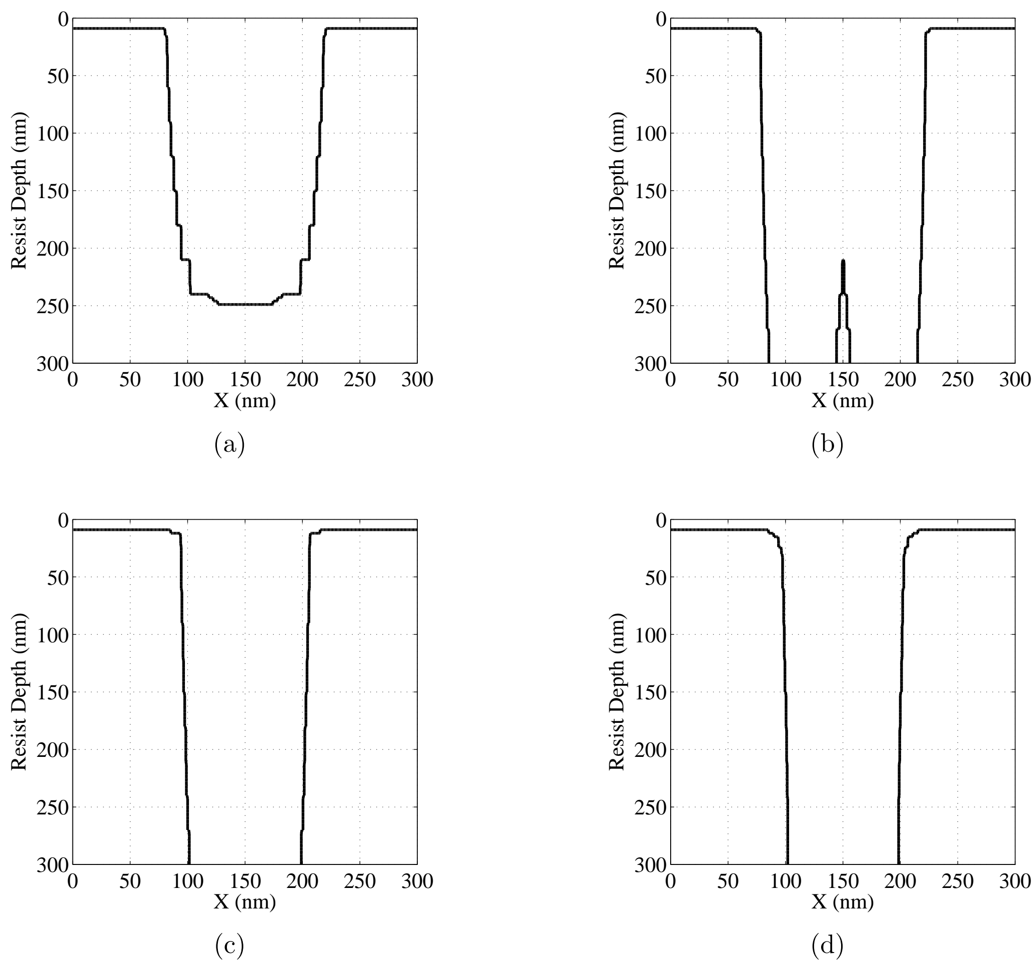

Figure 5.22: Cross-section resist profiles: (a) the uniform dose distribution, (b) the Type-V dose distribution, (c) the Type-M dose distribution, and (d) the Type-A dose distribution on the substrate system of 300 nm PMMA on Si.

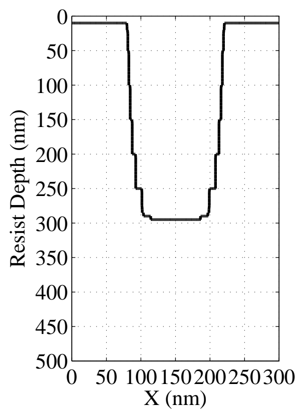

(a)

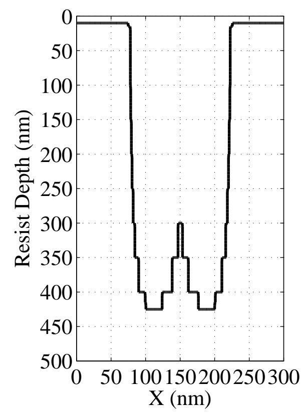

(b)

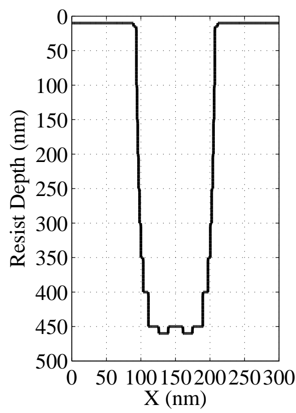

(c)

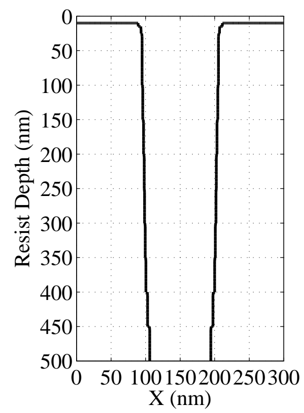

(d)

Figure 5.23: Cross-section resist profiles: (a) the uniform dose distribution, (b) the Type-V dose distribution, (c) the Type-M dose distribution, and (d) the Type-A dose distribution on the substrate system of 500 nm PMMA on Si.

From the profiles obtained by the uniform dose distribution (Fig. 5.21(a), Fig. 5.22(a), and Fig. 5.23(a)), it can be seen that the resist profile significantly deviates from the target one of vertical sidewall. The line width is much greater and the sidewall is clearly overcut. For the resist profiles (Fig. 5.21(b), Fig. 5.22(b), and Fig. 5.23(b)) obtained by the Type-V dose distribution, it can be seen that they are better than those by the uniform dose distribution, but the deviation from the target resist profile is still substantial. And they are even slightly worse than the uniform dose distribution results in a few cases. Also, the resist profiles are not always fully developed, which indicates that the Type-V dose distribution requires a higher total dose. The resist profiles obtained by the Type-M (Fig. 5.21(c), Fig. 5.22(c), and Fig. 5.23(c)) and Type-A (Fig. 5.21(d), Fig. 5.22(d), and Fig. 5.23(d)) dose distributions are much better, which achieve the resist profiles much closer to the target one in terms of CD error and sidewall shape.

In Fig. 5.24, the resist profiles achieved for feature size of 100 nm and total doses required by different dose distributions are provided. In this simulation, the lowest total dose to achieve a fully-developed resist profile as close to the target one of vertical sidewall as possible is found for each dose distribution type. It can be seen that the Type-A dose distribution requires the lowest total dose, which is 46.51% less than that of the uniform dose distribution. The Type-M dose distribution performs the second best, as achieving a total dose reduction of 41.86% compared to the uniform dose distribution, while the total dose reduction of the Type-V dose distribution is only 25.58%.

The correction methods are also compared quantitatively in terms of the percent width errors (refer to Section 5.2.2):

$$Average\ Percent\ Width\ Error = \frac{1}{n}\sum_{j=1}^{n}\frac{|p(j)-q(j)|}{q(j)} \times 100\%, \tag{5.6}$$

and

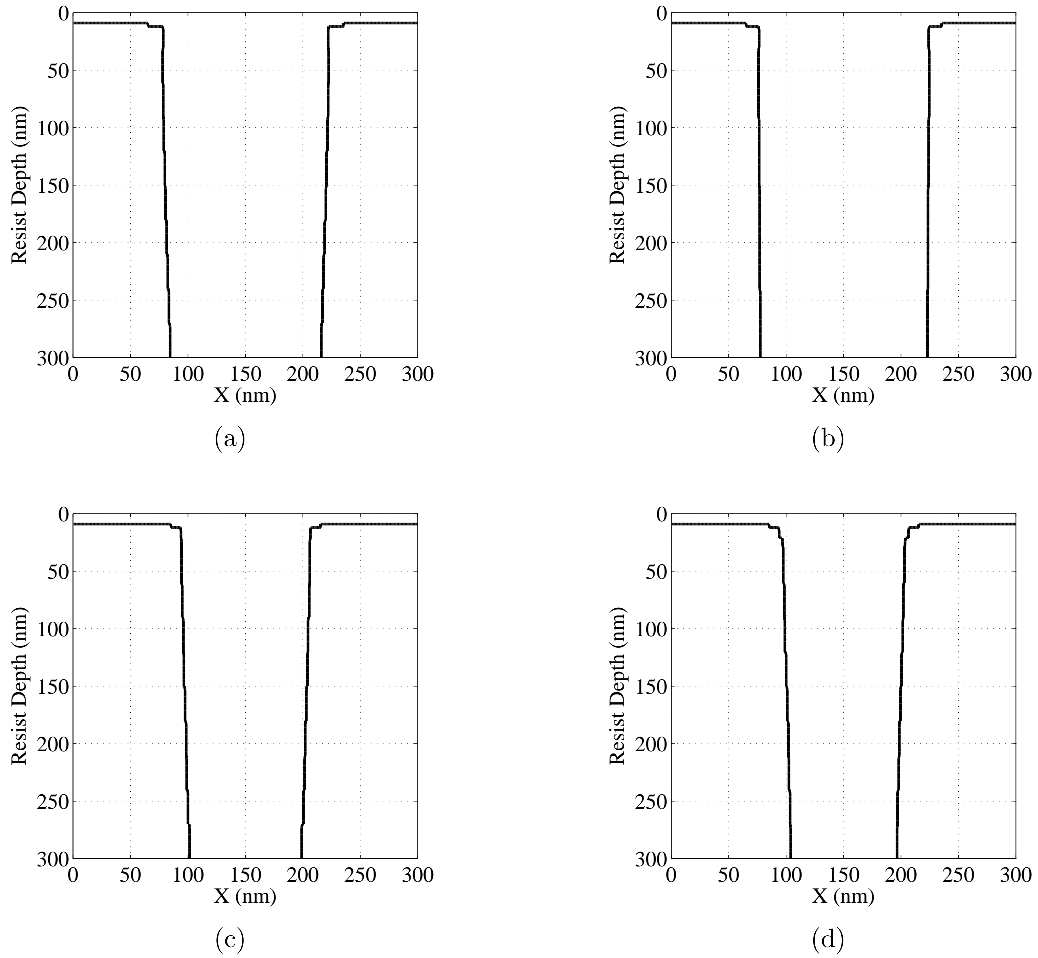

Figure 5.24: Cross-section resist profiles: (a) the uniform dose distribution (total dose $430\mu C/cm^2$), (b) the Type-V dose distribution (total dose $320\mu C/cm^2$), (c) the Type-M dose distribution (total dose $250\mu C/cm^2$), and (d) the Type-A dose distribution (total dose $230\mu C/cm^2$) on the substrate system of 300 nm PMMA on Si.

$$Max\ Percent\ Width\ Error = \max_{j=1}^{n} \frac{|p(j) - q(j)|}{q(j)} \times 100\%, \quad (5.7)$$

where $p(j)$ is the width of j-th layer in the final resist profile after correction, $q(j)$ is the target resist profile, and n is the number of resist layers (refer to Fig. 5.3).

The average and maximum percent width errors for feature size of 50 nm and 100 nm are provided in Table 5.1 and Table 5.2, respectively. Note that the maximum error reaches 100% in some cases, due to the underdevelopment in resist profiles (e.g., the bottom layer is not developed at all, leading to a zero width). The results show that the errors for the Type-M and Type-A dose distributions are significantly smaller than those for the Type-V dose distribution, as both average and maximum errors are greatly reduced.

PMMA Thickness (nm)	Uniform		Type-V		Type-M		Type-A	
	Avg (%)	Max (%)	Avg (%)	Max (%)	Avg (%)	Max (%)	Avg (%)	Max (%)
100	64.53	100.00	40.29	70.40	13.78	24.00	5.11	10.00
300	72.71	100.00	66.53	100.00	39.49	100.00	15.78	28.00
500	71.69	100.00	78.09	100.00	49.60	100.00	36.22	48.00

Table 5.1: Average and maximum percent width errors in resist profiles of 50 nm feature size for uniform, Type-V, Type-M and Type-A dose distributions.

PMMA Thickness (nm)	Uniform		Type-V		Type-M		Type-A	
	Avg (%)	Max (%)	Avg (%)	Max (%)	Avg (%)	Max (%)	Avg (%)	Max (%)
100	21.80	30.20	30.97	38.70	2.11	4.00	11.49	14.00
300	38.06	100.00	36.11	44.00	6.22	12.00	2.67	6.00
500	58.34	100.00	45.71	100.00	19.04	94.40	6.00	11.00

Table 5.2: Average and maximum percent width errors in resist profiles of 100 nm feature size for uniform, Type-V, Type-M and Type-A dose distributions.

In Table 5.3, the best dose distribution types with the minimum of required total dose under a variety of system parameters are derived using the proposed dose determination scheme (refer to Section 5.4). The results show that the Type-M and Type-A dose distributions outperform the conventional Type-V dose distribution in almost all cases.

Feature Size (nm)	PMMA Thickness (nm)	Beam Energy (KeV)	Beam Diameter (nm)	Minimum of Required Total Dose ($\mu C/cm^2$)			Best Type
				Type-V	Type-M	Type-A	
50	100	50	5	127	106	100	Type-A
50	300	50	5	282	248	205	Type-A
50	500	50	5	523	453	352	Type-A
100	100	50	5	141	122	147	Type-M
100	300	50	5	261	232	227	Type-A
100	500	50	5	437	369	318	Type-A
300	100	50	5	230	242	290	Type-V
300	300	50	5	336	326	372	Type-M
300	500	50	5	462	417	478	Type-M
100	500	5	5	96	87	95	Type-M
100	500	20	5	241	199	169	Type-A
100	500	50	5	437	369	318	Type-A
100	500	50	5	437	369	318	Type-A
100	500	50	10	467	394	334	Type-A
100	500	50	20	505	426	352	Type-A

Table 5.3: The best dose distribution type with the minimum of required total dose under a variety of system parameters.

From the above tables, it is observed that the Type-M dose distribution has the best result when the ratio of resist thickness to feature size is small, e.g., 1:1. However, as this ratio increases, the Type-A dose distribution tends to be the best one. On one hand, for a thicker resist, the exposure variation along the resist depth dimension is larger, i.e., the difference of developing rates between the top and the bottom layers becomes larger. On the other hand, for a smaller feature size, the path for the lateral development of the bottom layer of resist to catch up with that of the top layer of resist is shorter. Therefore, it is better to concentrate exposure, equivalently dose, at the center region in order to let the bottom

layer develop laterally relatively earlier. Therefore, the Type-A dose distribution is more suitable for fabrication of features in an extremely small scale.

5.7.2 Performance Comparison for Large-scale Uniform Patterns

The effectiveness of different dose distribution types (Type-V, Type-M, Type-A) in achieving a vertical sidewall have also been analyzed for large-scale uniform patterns. The substrate systems employed in the simulation are composed of PMMA on Si where the two different PMMA thicknesses, 300 nm and 100 nm, are considered. The beam energy is set to 50 KeV with the beam diameter of 5 nm. Two kinds of the uniform pattern consisting of lines were employed for performance analysis. In the one, to be referred to as Pattern I, each line is 51 μm long and 100 nm wide, and the gap between lines is 100 nm. In the other pattern, to be referred to as Pattern II, each line is 51 μm long and 50 nm wide, and the gap between lines is 50 nm. Both patterns cover the full range of electron scattering (for 50 KeV). The correction program partitions each line into segments of 3 μm for dose control.

First, the patterns are corrected by the proposed correction procedure (refer to Section 5.5) but without considering the variation of background exposure at different locations, i.e., the average background exposure of the entire pattern is used for correction. The three dose distribution types, i.e., Type-V, Type-M, and Type-A, are employed for the target resist profile of vertical sidewall. The simulation results for no correction (a uniform dose distribution) and correction using different dose distribution types are compared in terms of resist profile with a constraint that the total dose must be the same for all the cases. The results (cross-section resist profiles) at the corner, edge, and center locations of Pattern I for 300 nm PMMA on Si is provided in Figs. 5.25, 5.26, and 5.27.

The average and maximum percent width errors (refer to Eq. 5.6 and Eq. 5.7) at the corner, edge, and center locations of Pattern I for 300 nm PMMA on Si is provided in Table

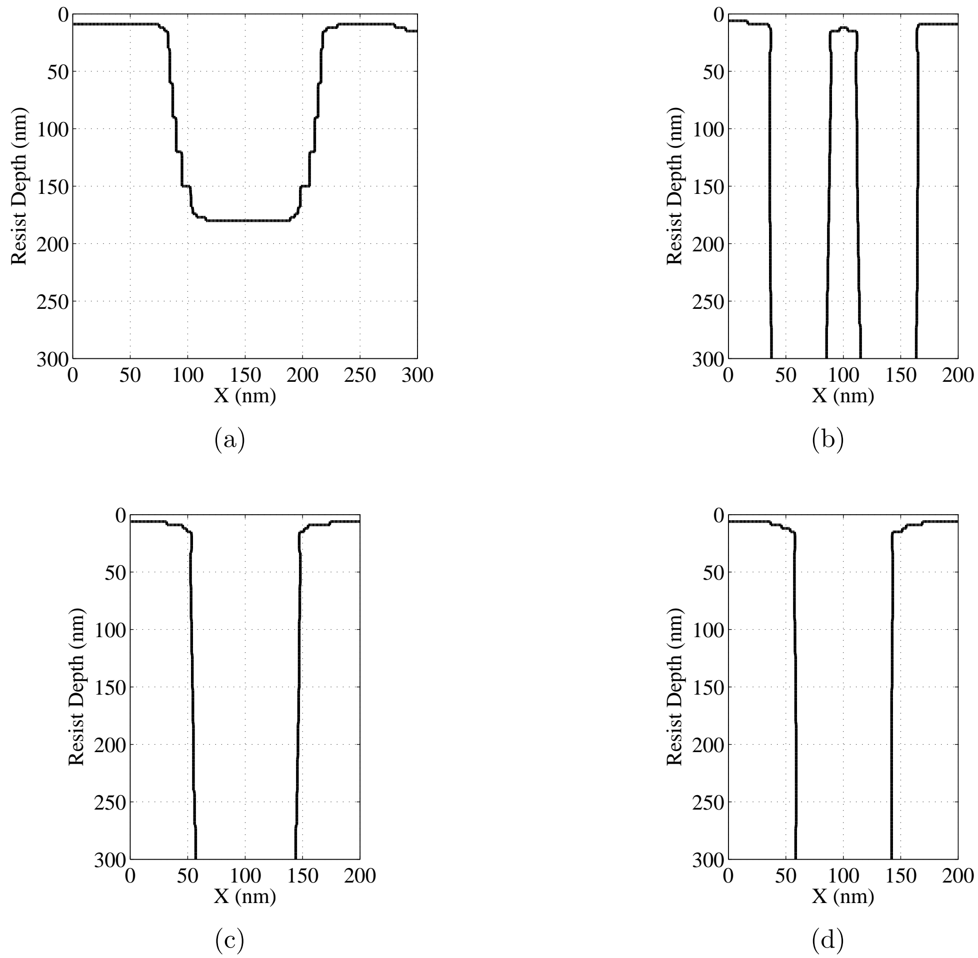

Figure 5.25: Cross-section resist profiles at the corner location of Pattern I: (a) the uniform dose distribution, (b) the Type-V dose distribution, (c) the Type-M dose distribution, and (d) the Type-A dose distribution on the substrate system of 300 nm PMMA on Si without considering the variation of background exposure.

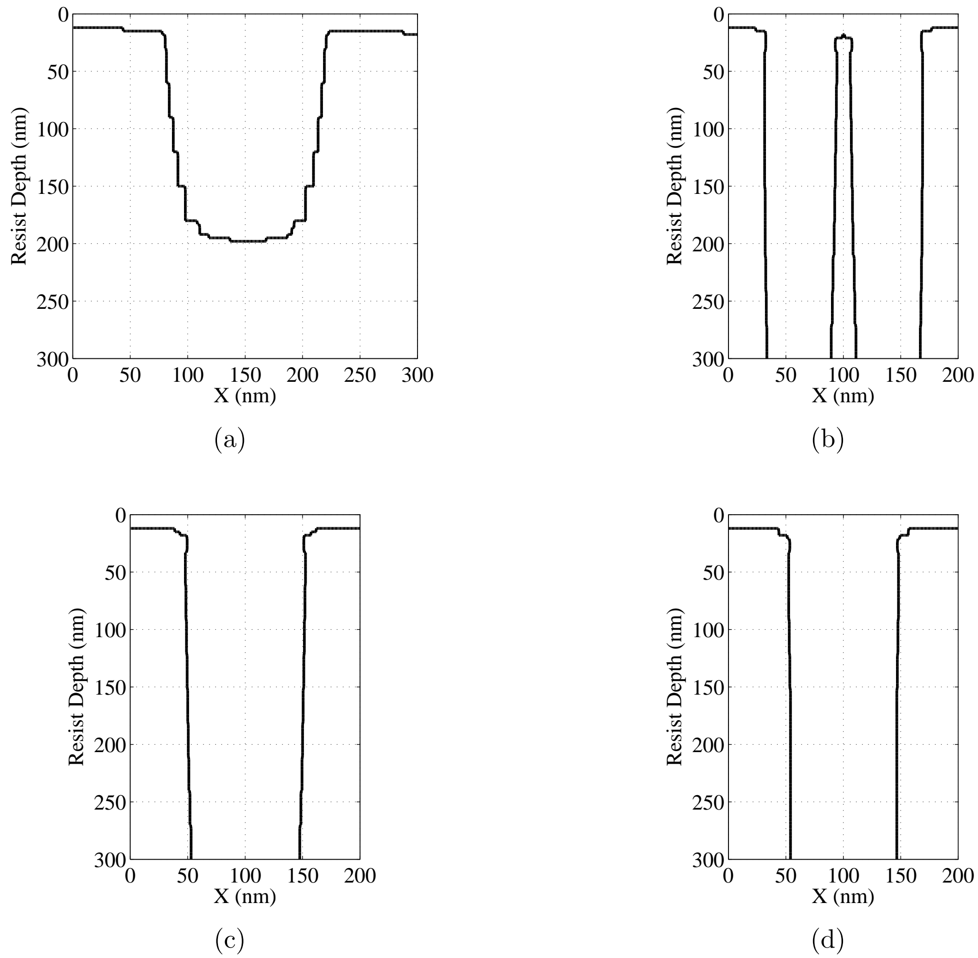

Figure 5.26: Cross-section resist profiles at the edge location of Pattern I: (a) the uniform dose distribution, (b) the Type-V dose distribution, (c) the Type-M dose distribution, and (d) the Type-A dose distribution on the substrate system of 300 nm PMMA on Si without considering the variation of background exposure.

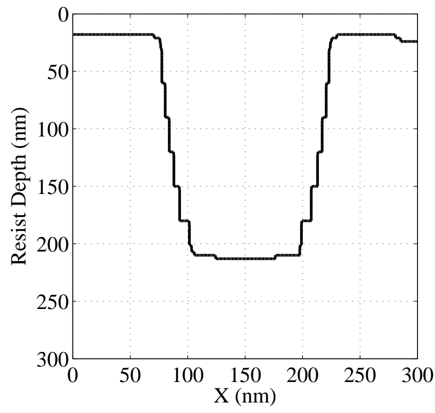

(a)

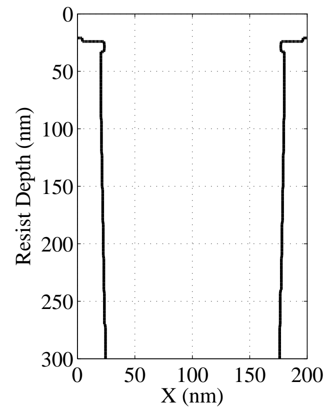

(b)

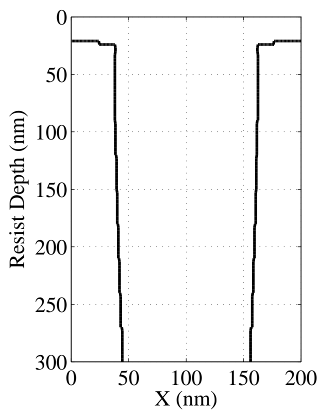

(c)

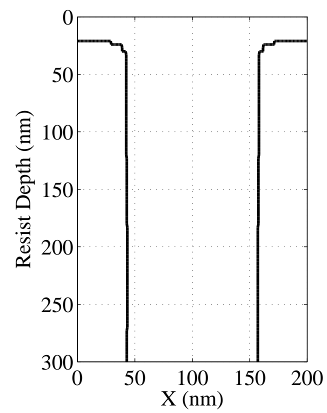

(d)

Figure 5.27: Cross-section resist profiles at the center location of Pattern I: (a) the uniform dose distribution, (b) the Type-V dose distribution, (c) the Type-M dose distribution, and (d) the Type-A dose distribution on the substrate system of 300 nm PMMA on Si without considering the variation of background exposure.

5.4. Note that the maximum error reaches 100% in some cases, due to the underdevelopment in resist profiles (e.g., the bottom layer is not developed at all, leading to a zero width).

Location	Uniform		Type-V		Type-M		Type-A	
	Avg (%)	Max (%)	Avg (%)	Max (%)	Avg (%)	Max (%)	Avg (%)	Max (%)
Corner	55.53	100.00	5.30	9.17	7.31	12.17	14.91	15.83
Edge	53.13	100.00	21.33	27.00	2.67	5.00	5.96	7.00
Center	50.96	100.00	56.74	60.00	20.00	25.00	15.02	16.33

Table 5.4: Average and maximum percent width errors in resist profiles of Pattern I on the substrate system of 300 nm PMMA on Si for uniform, Type-V, Type-M and Type-A dose distributions without considering the variation of background exposure.

From the above profiles and tables of errors, it can be seen that the resist profile significantly varies with location, i.e., the uniformity of resist profile among different locations is not achieved. Therefore, the necessity of taking the variation of background exposure into account in the proposed correction procedure has been proved in order to achieve better correction quality.

The patterns are corrected by the proposed correction procedure (refer to Section 5.5) with the three dose distribution types, i.e., Type-V, Type-M, and Type-A, for the target resist profile of vertical sidewall. The simulation results for no correction (a uniform dose distribution) and correction using different dose distribution types are compared in terms of resist profile with a constraint that the total dose must be the same for all the cases. The results (cross-section resist profiles) at the corner, edge, and center locations of Pattern I for 300 nm PMMA on Si and Pattern II for 100 nm PMMA on Si are provided in Figs. 5.28, 5.29, 5.30, 5.31, 5.32, and 5.33.

The average and maximum percent width errors (refer to Eq. 5.6 and Eq. 5.7) at the corner, edge, and center locations of Pattern I for 300 nm PMMA on Si and Pattern II for 100 nm PMMA on Si are provided in Table 5.5 and Table 5.6, respectively. Note that the

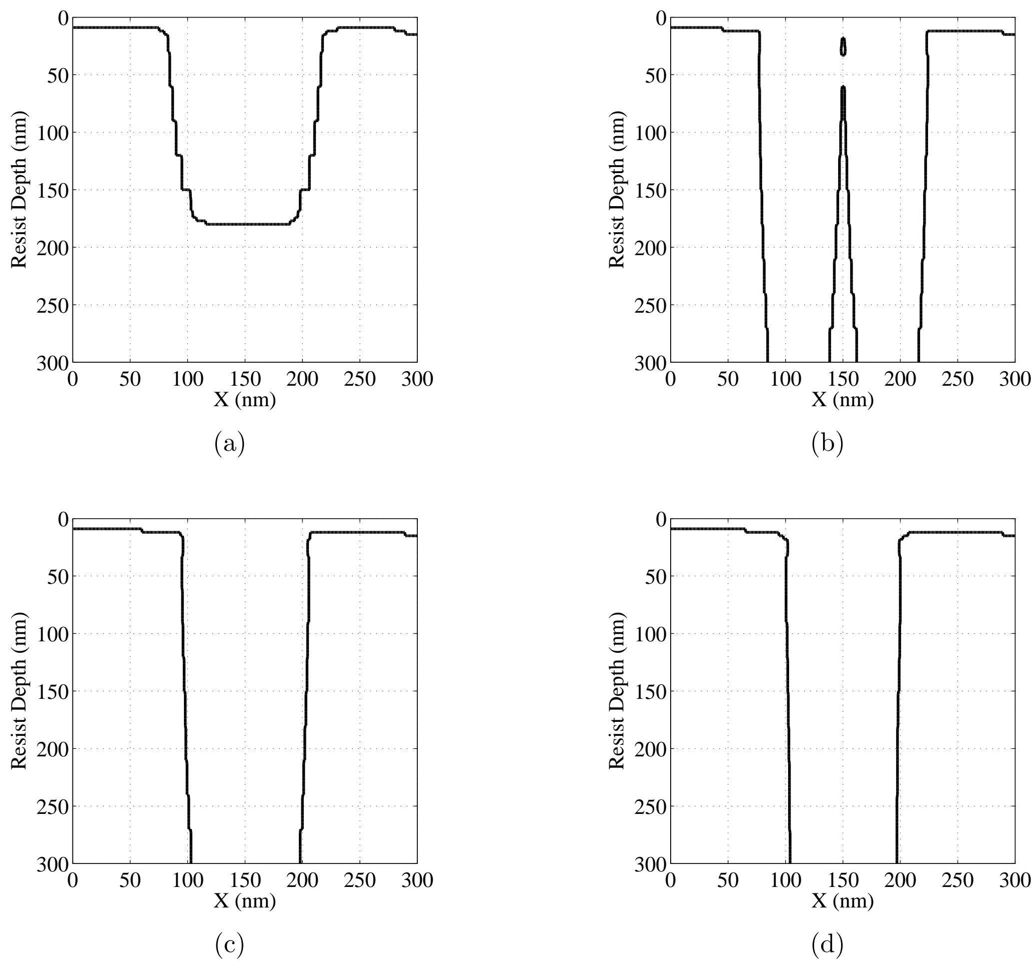

Figure 5.28: Cross-section resist profiles at the corner location of Pattern I: (a) the uniform dose distribution, (b) the Type-V dose distribution, (c) the Type-M dose distribution, and (d) the Type-A dose distribution on the substrate system of 300 nm PMMA on Si.

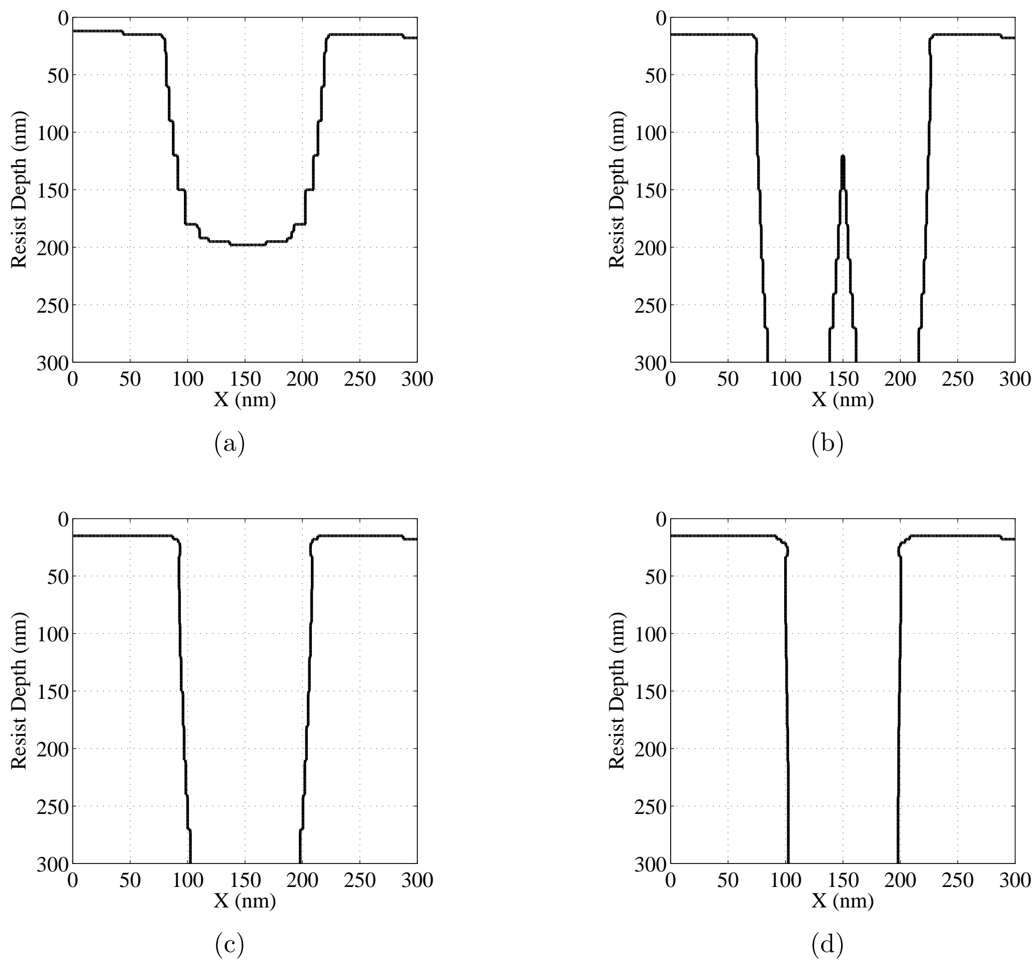

Figure 5.29: Cross-section resist profiles at the edge location of Pattern I: (a) the uniform dose distribution, (b) the Type-V dose distribution, (c) the Type-M dose distribution, and (d) the Type-A dose distribution on the substrate system of 300 nm PMMA on Si.

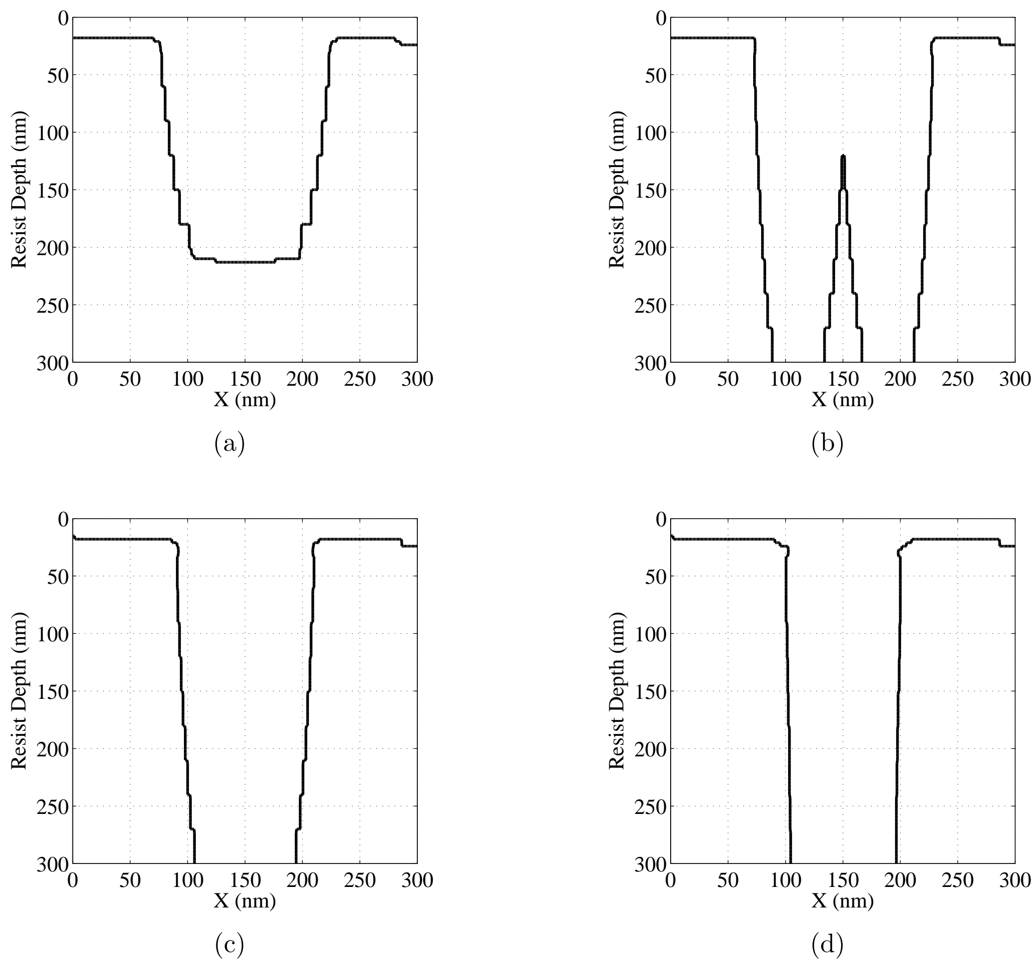

Figure 5.30: Cross-section resist profiles at the center location of Pattern I: (a) the uniform dose distribution, (b) the Type-V dose distribution, (c) the Type-M dose distribution, and (d) the Type-A dose distribution on the substrate system of 300 nm PMMA on Si.

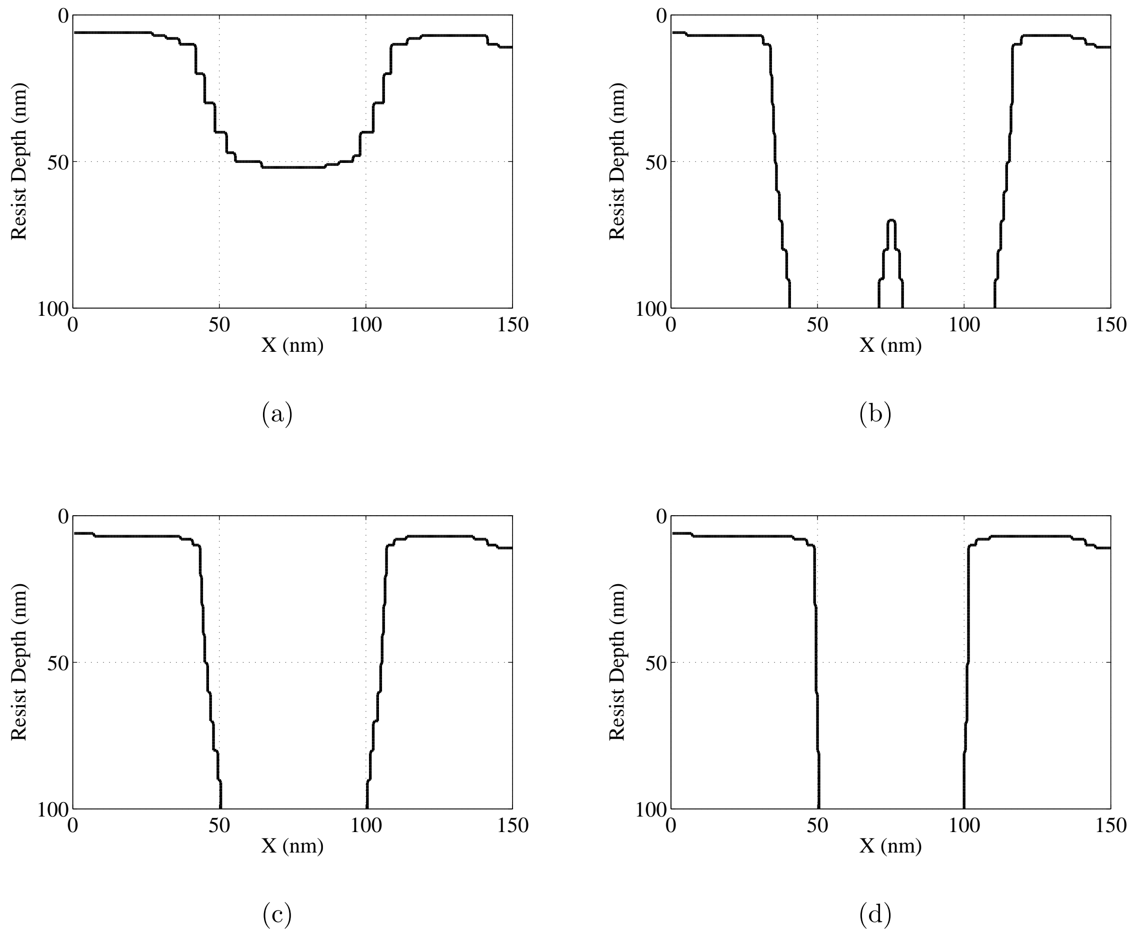

Figure 5.31: Cross-section resist profiles at the corner location of Pattern II: (a) the uniform dose distribution, (b) the Type-V dose distribution, (c) the Type-M dose distribution, and (d) the Type-A dose distribution on the substrate system of 100 nm PMMA on Si.

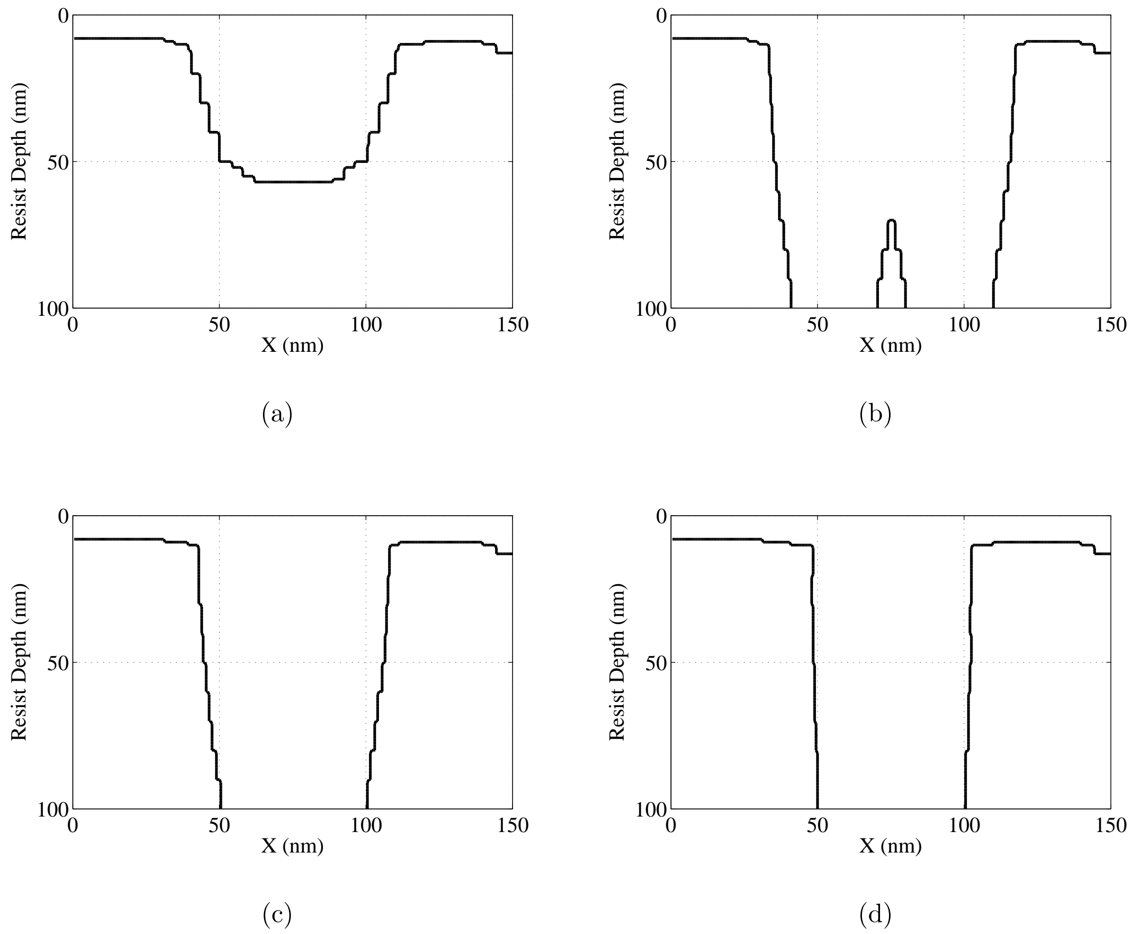

Figure 5.32: Cross-section resist profiles at the edge location of Pattern II: (a) the uniform dose distribution, (b) the Type-V dose distribution, (c) the Type-M dose distribution, and (d) the Type-A dose distribution on the substrate system of 100 nm PMMA on Si.

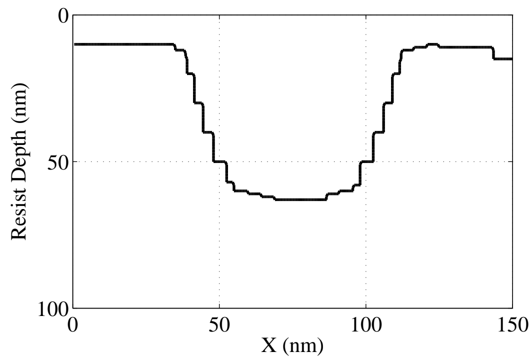

(a)

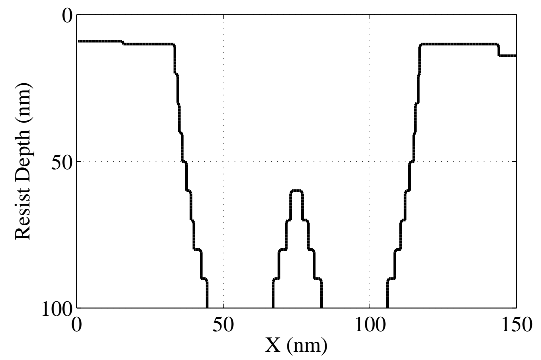

(b)

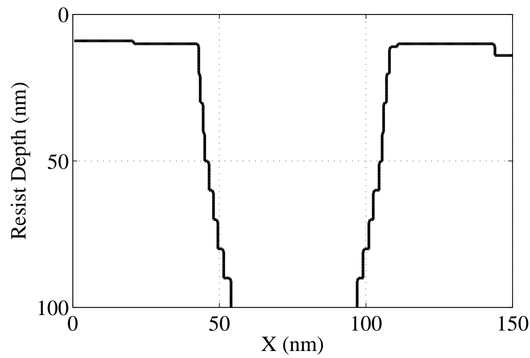

(c)

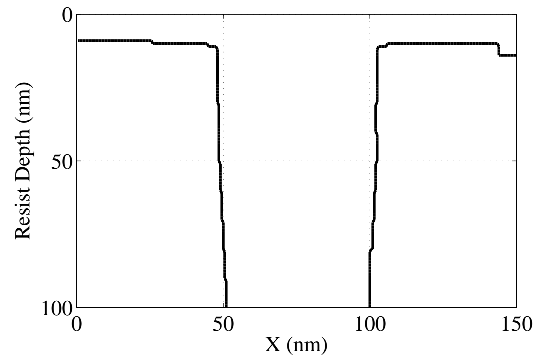

(d)

Figure 5.33: Cross-section resist profiles at the center location of Pattern II: (a) the uniform dose distribution, (b) the Type-V dose distribution, (c) the Type-M dose distribution, and (d) the Type-A dose distribution on the substrate system of 100 nm PMMA on Si.

maximum error reaches 100% in some cases, due to the underdevelopment in resist profiles (e.g., the bottom layer is not developed at all, leading to a zero width).

Location	Uniform		Type-V		Type-M		Type-A	
	Avg (%)	Max (%)	Avg (%)	Max (%)	Avg (%)	Max (%)	Avg (%)	Max (%)
Corner	55.53	100.00	31.50	47.50	6.06	11.00	3.44	6.50
Edge	53.13	100.00	37.22	52.50	9.28	16.50	2.17	4.00
Center	50.96	100.00	35.00	55.50	10.61	19.50	3.78	7.50

Table 5.5: Average and maximum percent width errors in resist profiles of Pattern I on the substrate system of 300 nm PMMA on Si for uniform, Type-V, Type-M and Type-A dose distributions.

Location	Uniform		Type-V		Type-M		Type-A	
	Avg (%)	Max (%)	Avg (%)	Max (%)	Avg (%)	Max (%)	Avg (%)	Max (%)
Corner	63.12	100.00	52.79	67.10	16.79	29.10	3.57	7.10
Edge	60.38	100.00	53.07	72.60	19.18	34.60	6.84	12.60
Center	58.63	100.00	44.24	73.20	17.63	36.70	6.60	16.40

Table 5.6: Average and maximum percent width errors in resist profiles of Pattern II on the substrate system of 100 nm PMMA on Si for uniform, Type-V, Type-M and Type-A dose distributions.

From the above profiles and tables of errors, it can be seen that the Type-A dose distribution provides the best correction quality as it has the best control of dose at the edge regions in order to compensate the increased background exposure. The results show that the Type-A dose distribution greatly improves the uniformity of resist profile among different locations of a pattern, and also achieves the resist profiles much closer to the target one in terms of CD error and sidewall shape (vertical). Also it is shown that the errors for the Type-A dose distribution are significantly smaller than those for the Type-M and Type-V dose distributions, as both average and maximum errors are greatly reduced. Therefore, the

Type-A dose distribution is proved to outperform the other two dose distribution types in the cases of small feature sizes, large pattern sizes, and high uniform pattern densities.

5.7.3 Performance Comparison for Large-scale Nonuniform Patterns

Finally, the effectiveness of different dose distribution types (Type-V, Type-M, Type-A) in achieving a vertical sidewall have been analyzed for large-scale nonuniform patterns. The substrate system employed in the simulation is composed of 300 nm PMMA on Si. The beam energy is set to 50 KeV with the beam diameter of 5 nm. A 2.5 μm by 2.5 μm pattern consisting of different types of squares and rectangles shown in Fig. 5.34 is employed for performance analysis. A total number of 100 features are distributed nonuniformly in this pattern with the smallest ones 50 nm by 50 nm squares and the largest ones 100 nm by 100 nm squares. The five test locations are shown in Fig. 5.34.

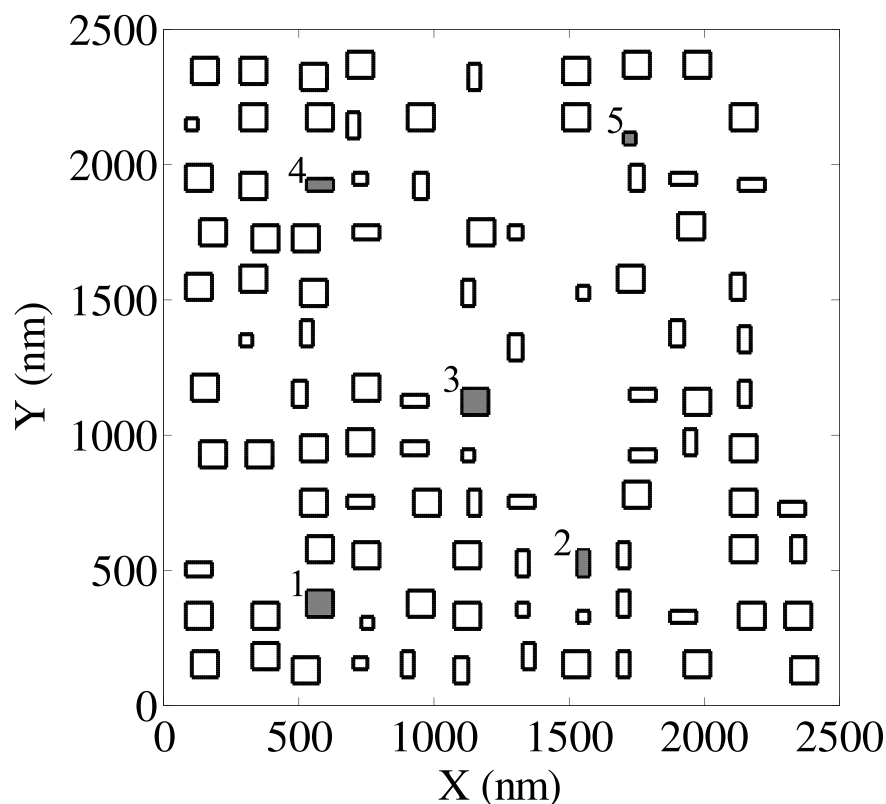

Figure 5.34: Five test locations in the test nonuniform pattern.

First, the pattern is corrected by the proposed correction procedure (refer to Section 5.6) but without considering the variation of pattern density at different locations, i.e., the average pattern density of the entire pattern is used for correction. The three dose distribution types, i.e., Type-V, Type-M, and Type-A, are employed for the target resist profile of vertical sidewall. The simulation results for no correction (a uniform dose distribution) and correction using different dose distribution types are compared in terms of resist profile with a constraint that the total dose must be the same for all the cases. The results (cross-section resist profiles in X-dimension and Y-dimension) at the test locations of the nonuniform pattern are provided in Figs. 5.35, 5.36, 5.37, and 5.38.

The average and maximum percent width errors (refer to Eq. 5.6 and Eq. 5.7) at the test locations of the nonuniform pattern are provided in Table 5.7 and Table 5.8, respectively. Note that the maximum error reaches 100% in some cases, due to the underdevelopment in resist profiles (e.g., the bottom layer is not developed at all, leading to a zero width).

Test Location	Uniform		Type-V		Type-M		Type-A	
	Avg (%)	Max (%)	Avg (%)	Max (%)	Avg (%)	Max (%)	Avg (%)	Max (%)
1	54.43	100.00	26.48	54.30	6.22	15.00	9.89	15.00
2	65.20	100.00	54.20	100.00	25.89	100.00	20.22	26.00
3	54.50	100.00	34.96	100.00	18.88	68.90	6.22	18.00
4	56.37	100.00	37.22	100.00	11.47	43.20	7.78	14.00
5	65.62	100.00	52.89	100.00	32.20	100.00	9.78	16.00

Table 5.7: Average and maximum percent width errors in X-dimension of resist profiles of the nonuniform pattern for uniform, Type-V, Type-M and Type-A dose distributions on the substrate system of 300 nm PMMA on Si without considering the variation of pattern density.

From the above profiles and tables of errors, it can be seen that the resist profiles are not well corrected, especially the same resist profiles are not achieved for same type of features at different locations with different pattern densities. Therefore, the necessity of taking

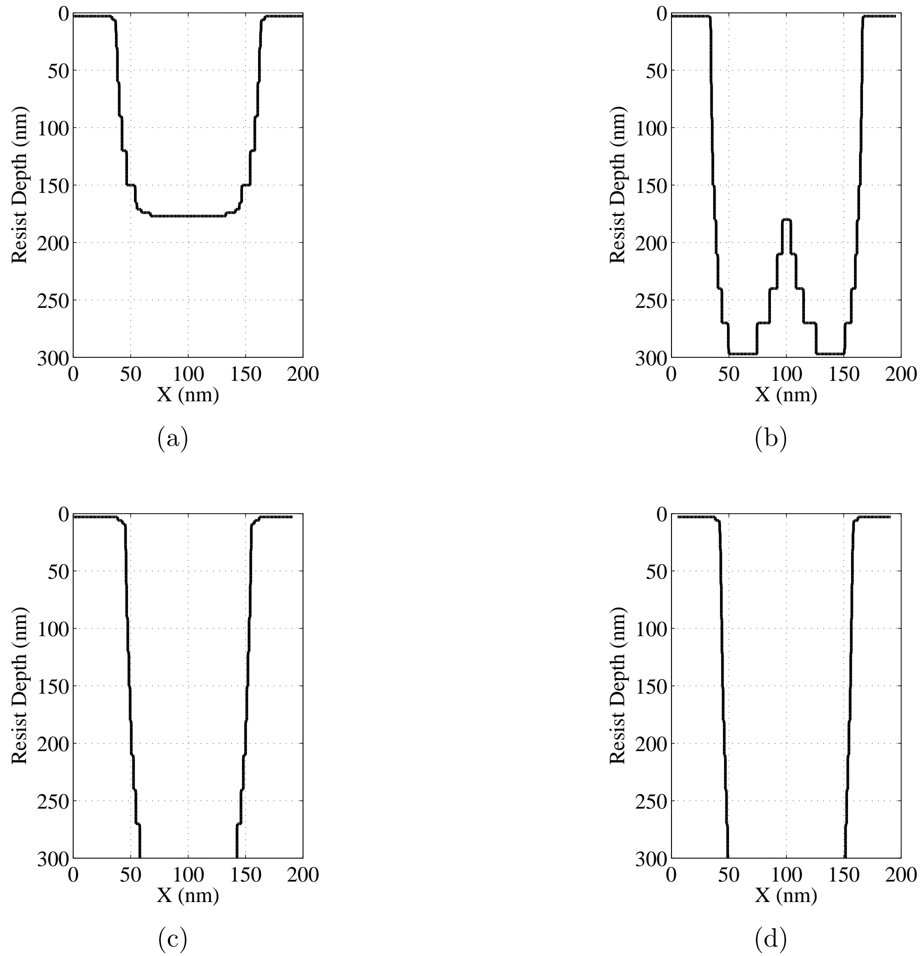

Figure 5.35: Cross-section resist profiles in X-dimension at the test location 1 of the nonuniform pattern: (a) the uniform dose distribution, (b) the Type-V dose distribution, (c) the Type-M dose distribution, and (d) the Type-A dose distribution on the substrate system of 300 nm PMMA on Si without considering the variation of pattern density.

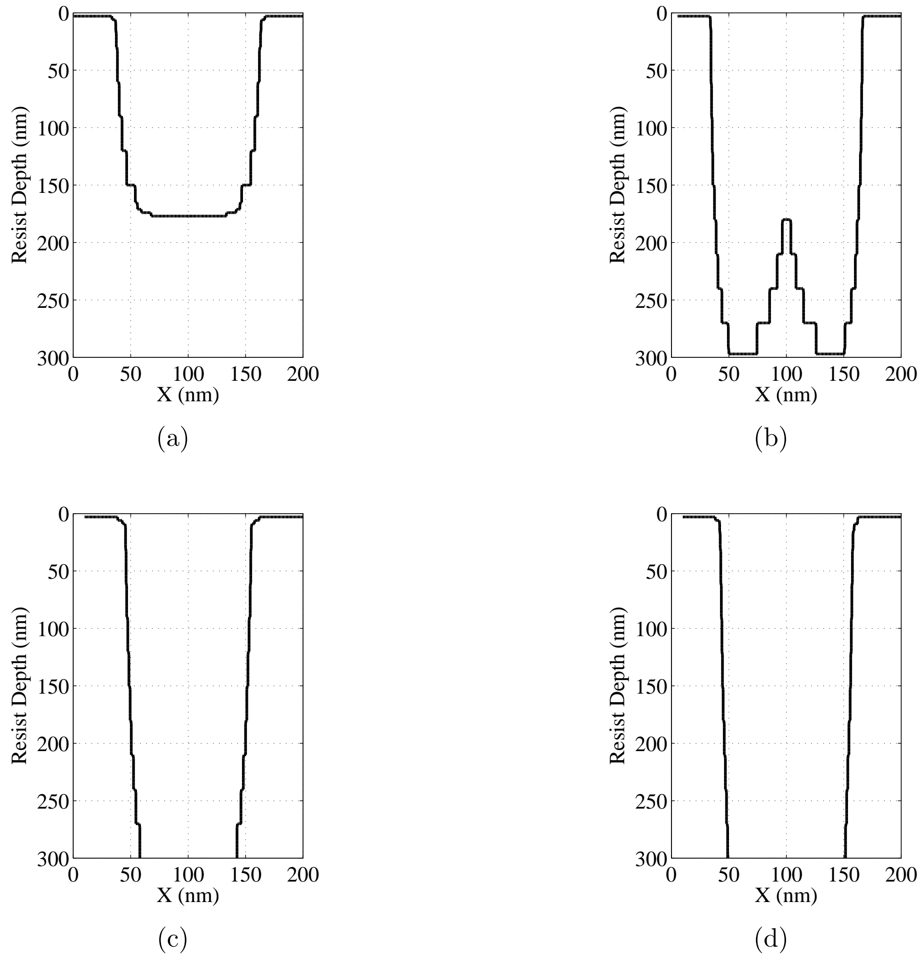

Figure 5.36: Cross-section resist profiles in Y-dimension at the test location 1 of the nonuniform pattern: (a) the uniform dose distribution, (b) the Type-V dose distribution, (c) the Type-M dose distribution, and (d) the Type-A dose distribution on the substrate system of 300 nm PMMA on Si without considering the variation of pattern density.

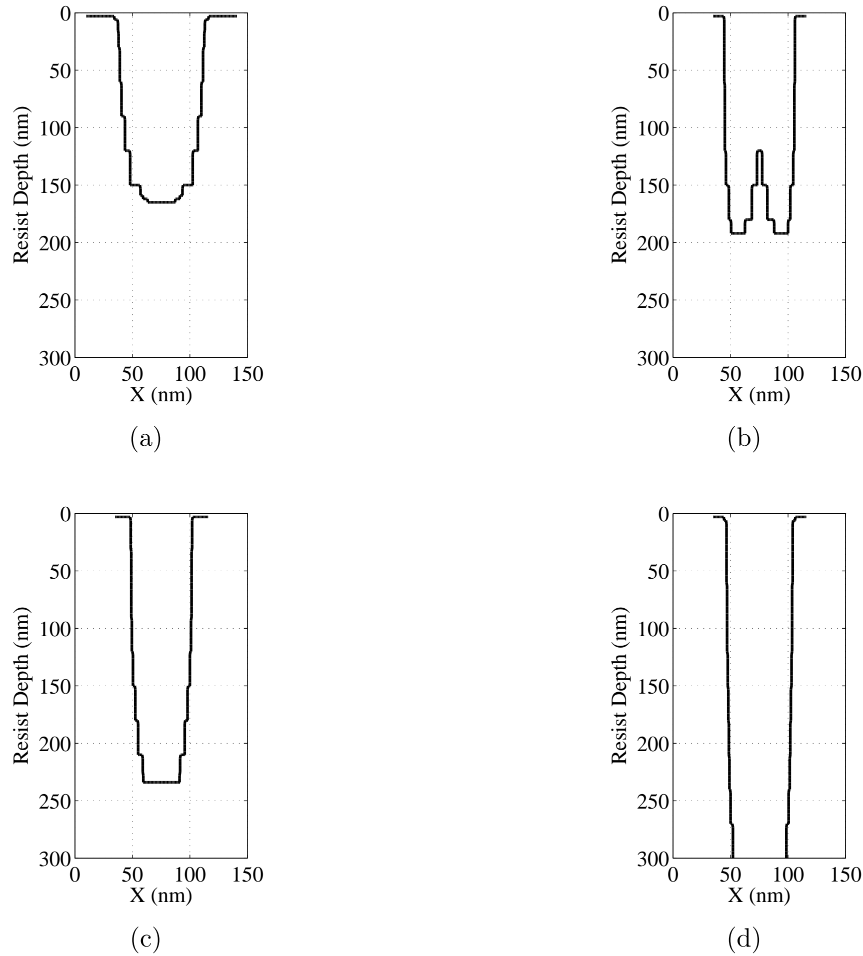

Figure 5.37: Cross-section resist profiles in X-dimension at the test location 5 of the nonuniform pattern: (a) the uniform dose distribution, (b) the Type-V dose distribution, (c) the Type-M dose distribution, and (d) the Type-A dose distribution on the substrate system of 300 nm PMMA on Si without considering the variation of pattern density.

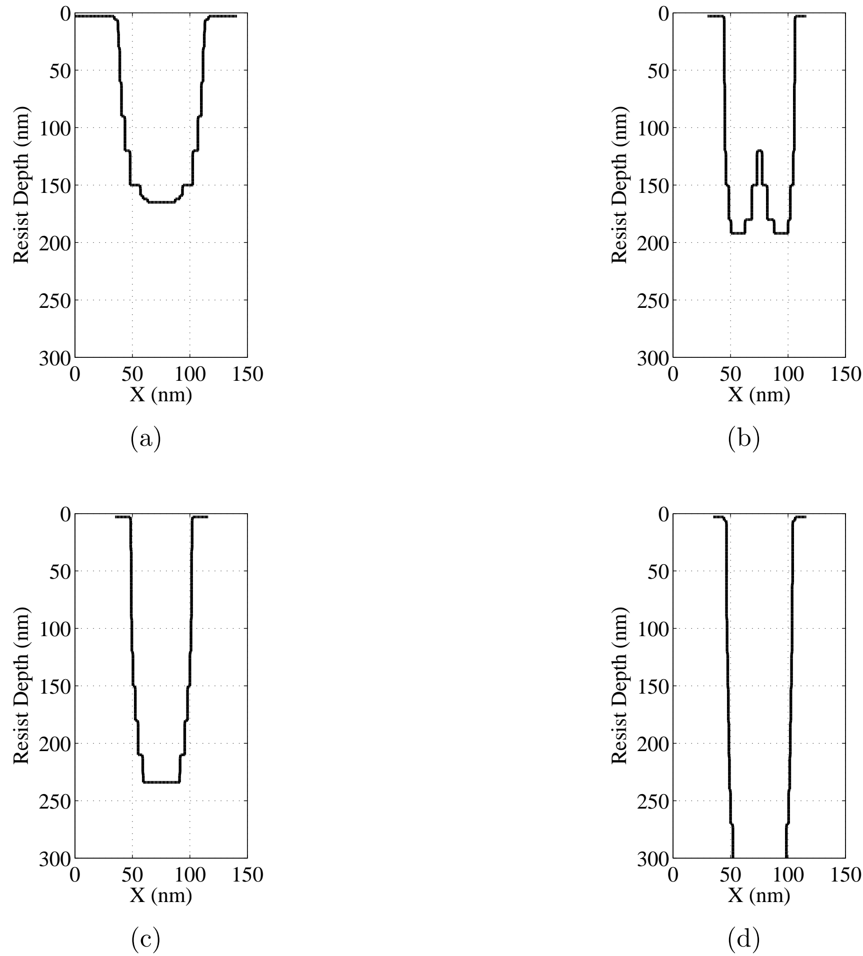

Figure 5.38: Cross-section resist profiles in Y-dimension at the test location 5 of the nonuniform pattern: (a) the uniform dose distribution, (b) the Type-V dose distribution, (c) the Type-M dose distribution, and (d) the Type-A dose distribution on the substrate system of 300 nm PMMA on Si without considering the variation of pattern density.

Test Location	Uniform		Type-V		Type-M		Type-A	
	Avg (%)	Max (%)	Avg (%)	Max (%)	Avg (%)	Max (%)	Avg (%)	Max (%)
1	54.48	100.00	26.48	54.30	6.22	15.00	9.89	15.00
2	56.88	100.00	41.84	100.00	22.93	98.40	6.94	18.00
3	54.50	100.00	34.96	100.00	18.88	68.90	6.22	18.00
4	65.16	100.00	59.38	100.00	25.29	61.60	31.56	40.00
5	65.62	100.00	52.89	100.00	32.20	100.00	9.89	16.00

Table 5.8: Average and maximum percent width errors in Y-dimension of resist profiles of the nonuniform pattern for uniform, Type-V, Type-M and Type-A dose distributions on the substrate system of 300 nm PMMA on Si without considering the variation of pattern density.

the variation of pattern density into account in the proposed correction procedure has been proved in order to achieve better correction quality.

The pattern is corrected by the proposed correction procedure (refer to Section 5.6) with the three dose distribution types, i.e., Type-V, Type-M, and Type-A, for the target resist profile of vertical sidewall. The simulation results for no correction (a uniform dose distribution) and correction using different dose distribution types are compared in terms of resist profile with a constraint that the total dose must be the same for all the cases. The results (cross-section resist profiles in X-dimension and Y-dimension) at the test locations of the nonuniform pattern are provided in Figs. 5.39, 5.40, 5.41, 5.42, 5.43, and 5.44.

The average and maximum percent width errors (refer to Eq. 5.6 and Eq. 5.7) at the test locations of the nonuniform pattern are provided in Table 5.9 and Table 5.10, respectively. Note that the maximum error reaches 100% in some cases, due to the underdevelopment in resist profiles (e.g., the bottom layer is not developed at all, leading to a zero width).

From the above profiles and tables of errors, it can be seen that the resist profiles obtained by the Type-V dose distribution are significantly deviates from the target one and indicate that a higher total dose is required. The resist profiles obtained by the Type-M dose

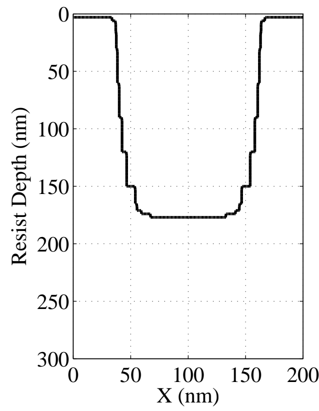

(a)

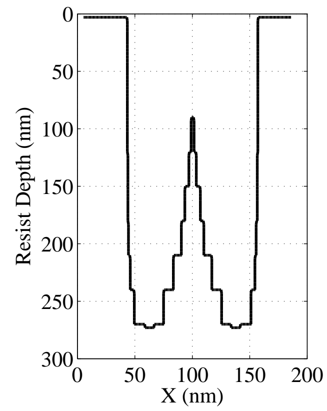

(b)

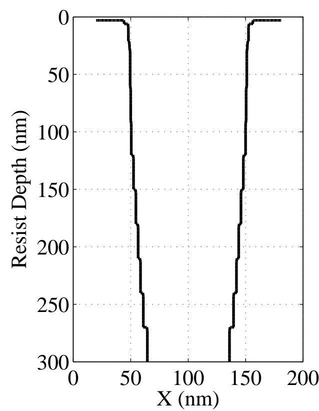

(c)

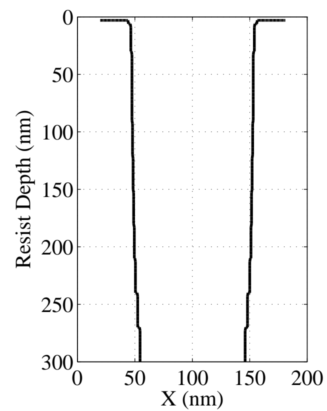

(d)

Figure 5.39: Cross-section resist profiles in X-dimension at the test location 1 of the nonuniform pattern: (a) the uniform dose distribution, (b) the Type-V dose distribution, (c) the Type-M dose distribution, and (d) the Type-A dose distribution on the substrate system of 300 nm PMMA on Si.

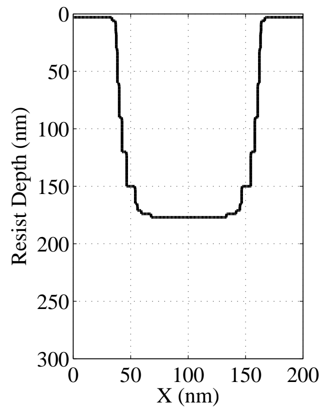

(a)

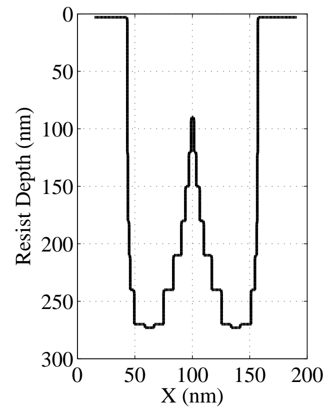

(b)

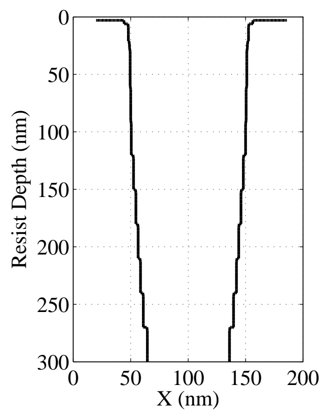

(c)

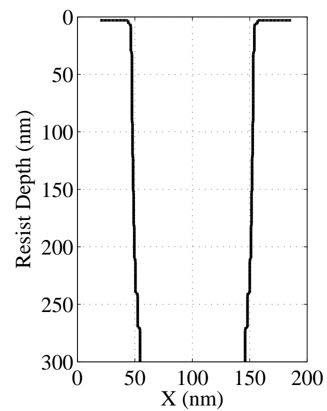

(d)

Figure 5.40: Cross-section resist profiles in Y-dimension at the test location 1 of the nonuniform pattern: (a) the uniform dose distribution, (b) the Type-V dose distribution, (c) the Type-M dose distribution, and (d) the Type-A dose distribution on the substrate system of 300 nm PMMA on Si.

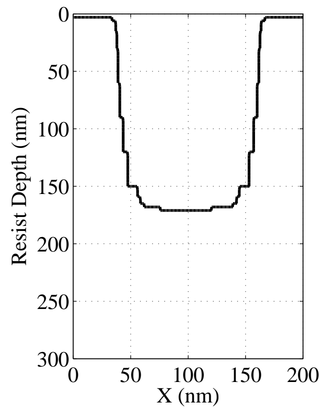

(a)

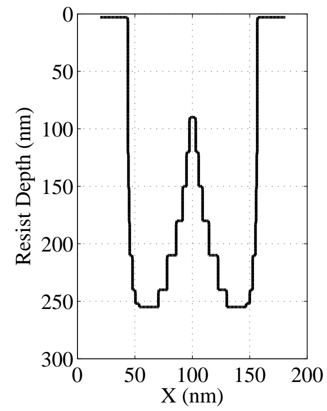

(b)

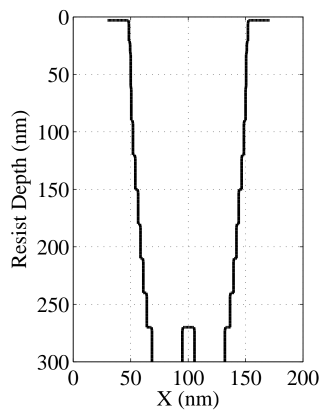

(c)

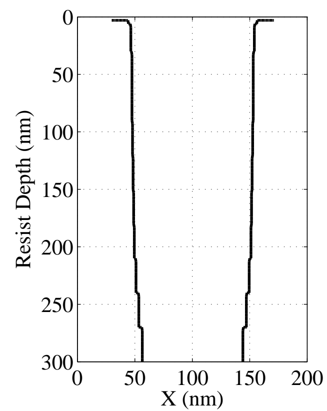

(d)

Figure 5.41: Cross-section resist profiles in X-dimension at the test location 4 of the nonuniform pattern: (a) the uniform dose distribution, (b) the Type-V dose distribution, (c) the Type-M dose distribution, and (d) the Type-A dose distribution on the substrate system of 300 nm PMMA on Si.

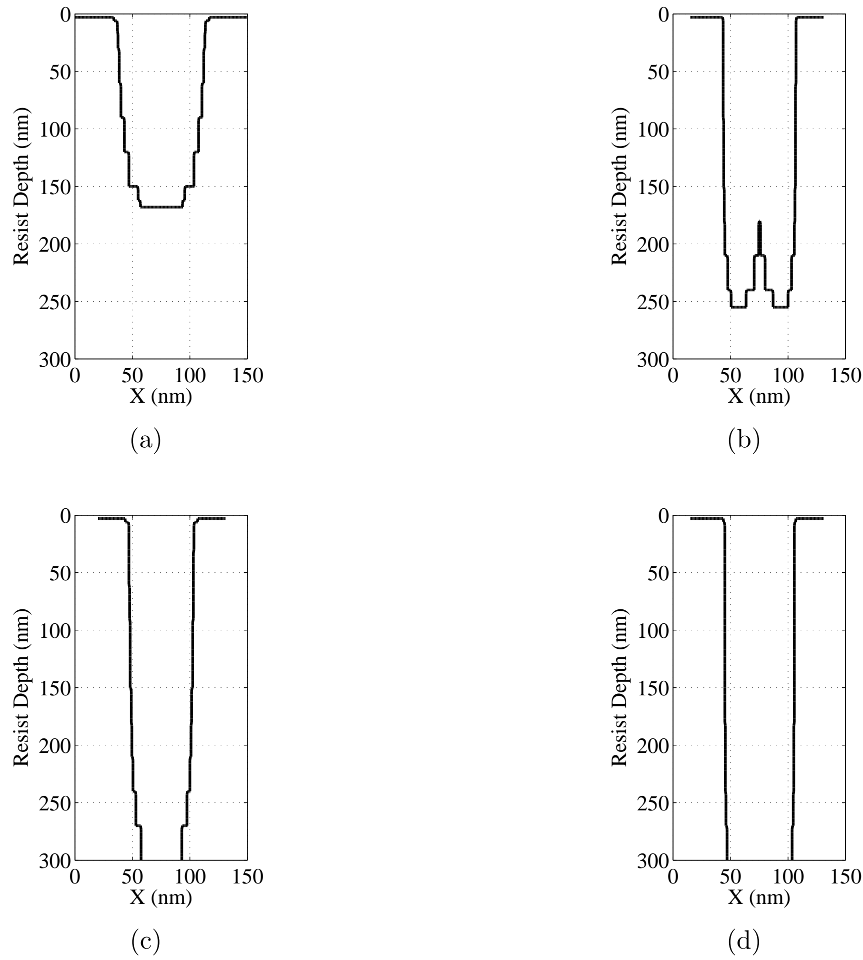

Figure 5.42: Cross-section resist profiles in Y-dimension at the test location 4 of the nonuniform pattern: (a) the uniform dose distribution, (b) the Type-V dose distribution, (c) the Type-M dose distribution, and (d) the Type-A dose distribution on the substrate system of 300 nm PMMA on Si.

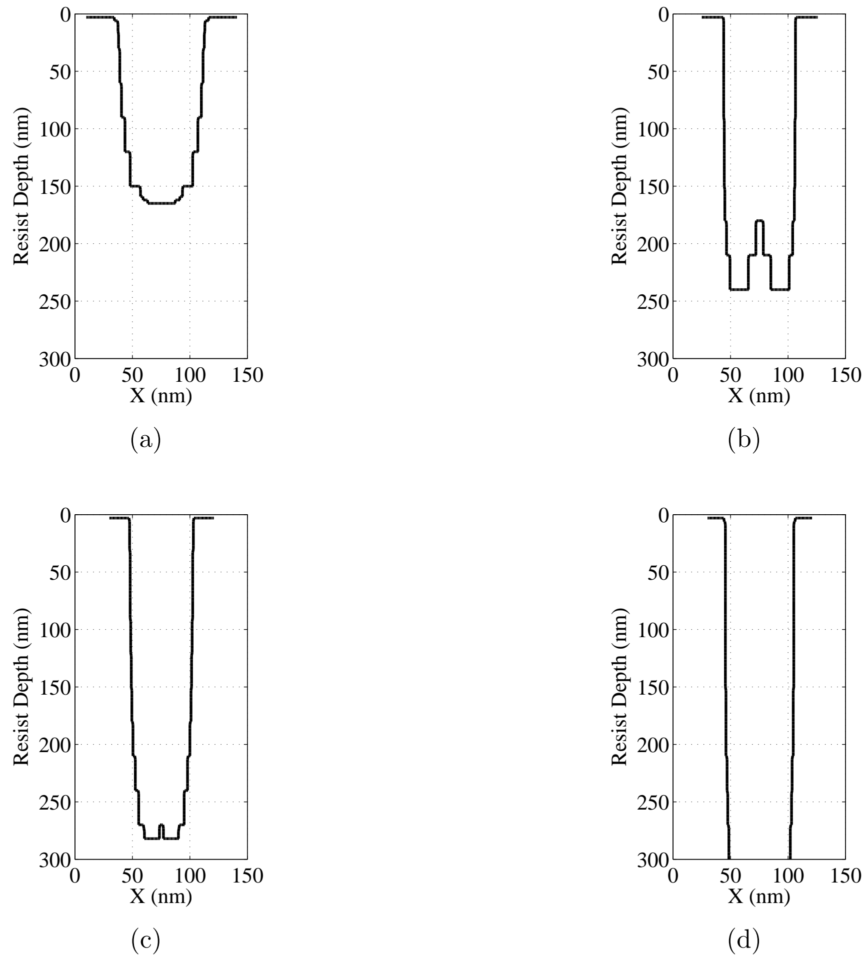

Figure 5.43: Cross-section resist profiles in X-dimension at the test location 5 of the nonuniform pattern: (a) the uniform dose distribution, (b) the Type-V dose distribution, (c) the Type-M dose distribution, and (d) the Type-A dose distribution on the substrate system of 300 nm PMMA on Si.

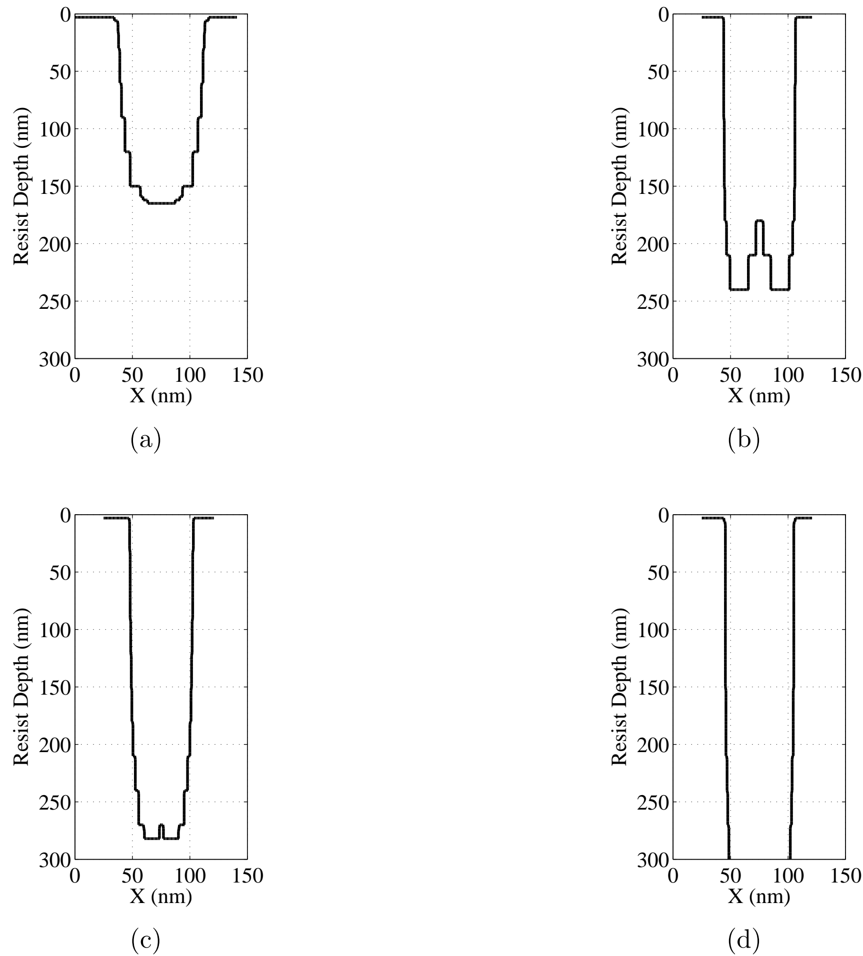

Figure 5.44: Cross-section resist profiles in Y-dimension at the test location 5 of the nonuniform pattern: (a) the uniform dose distribution, (b) the Type-V dose distribution, (c) the Type-M dose distribution, and (d) the Type-A dose distribution on the substrate system of 300 nm PMMA on Si.

Test Location	Uniform		Type-V		Type-M		Type-A	
	Avg (%)	Max (%)	Avg (%)	Max (%)	Avg (%)	Max (%)	Avg (%)	Max (%)
1	54.43	100.00	24.99	98.40	10.22	28.00	4.22	8.00
2	65.20	100.00	36.55	100.00	10.44	28.00	19.56	22.00
3	54.50	100.00	24.99	98.40	10.22	28.00	4.22	8.00
4	56.37	100.00	31.02	100.00	14.78	46.00	5.00	12.00
5	65.62	100.00	40.00	100.00	16.02	78.20	16.67	20.00

Table 5.9: Average and maximum percent width errors in X-dimension of resist profiles of the nonuniform pattern for uniform, Type-V, Type-M and Type-A dose distributions on the substrate system of 300 nm PMMA on Si.

Test Location	Uniform		Type-V		Type-M		Type-A	
	Avg (%)	Max (%)	Avg (%)	Max (%)	Avg (%)	Max (%)	Avg (%)	Max (%)
1	54.48	100.00	25.10	98.40	10.22	28.00	4.22	8.00
2	56.88	100.00	30.91	100.00	14.78	46.00	5.11	13.00
3	54.50	100.00	24.99	98.40	10.22	28.00	4.22	8.00
4	65.16	100.00	36.67	100.00	10.33	28.00	20.22	22.00
5	65.62	100.00	39.89	100.00	16.02	78.20	16.67	20.00

Table 5.10: Average and maximum percent width errors in Y-dimension of resist profiles of the nonuniform pattern for uniform, Type-V, Type-M and Type-A dose distributions on the substrate system of 300 nm PMMA on Si.

distribution are slightly better while the Type-A dose distribution provides the resist profiles closest to the target ones in terms of CD error and sidewall shape (vertical). Compared to the other two dose distributions, the Type-A dose distribution further reduces both average and maximum errors greatly. More importantly, very similar resist profiles are achieved for same type of features at different locations with different pattern densities. Therefore, it is further proved that the Type-A dose distribution performs the best in the cases of small feature sizes, large pattern sizes, and varied pattern densities.

5.7.4 Dependency on Feature and Lithographic Parameters

The dependency of dose distribution on a variety of system parameters (feature and lithographic parameters) has been analyzed by considering the region-wise dose contrast of

each dose distribution type (Type-V, Type-M, Type-A). The region-wise dose contrast is defined as the ratio of the highest dose of all the regions to the lowest dose of all the regions of a feature after correction, i.e., $d(1)/d(3)$ for the Type-V case, $d(2)/d(1)$ for the Type-M case, and $d(3)/d(1)$ for the Type-A case. A higher contrast dose distribution means that this ratio is larger, and vice versa.

The reason for such definitions is that these ratios play the most important role in determining the resist profile. For example, in the Type-A case, $d(3)$ determines how fast the developer can reach the bottom layer of resist at the center region, and $d(1)$ determines how possible the lateral developing process of the bottom layer of resist can catch up with that of the top layer of resist at the boundaries of the feature (the boundaries between the exposed area and the unexposed area). Therefore, the ratio $d(3)/d(1)$ clearly quantifies the effect of dose distribution on the resist profile for the Type-A case.

The employed system parameters are listed below:

- Feature Size: Affecting the influence of proximity effect on a feature.
- Feature Density: Affecting the background exposure level of a pattern.
- Resist Thickness: Affecting the exposure variation along the resist depth dimension.
- Beam Energy: Affecting the intensity and range of proximity effect.
- Beam Diameter: Affecting the intensity and range of proximity effect.
- Total Dose: Affecting the exposure distribution in the resist.
- Developing Time: Affecting the resist development process.
- Conversion Formula: Affecting the contrast of developing rates between the exposed area and the unexposed area.

The specific values of the above-mentioned system parameters are feature size (100 nm/50 nm), feature density (0%, i.e., Isolated Feature/50%), resist thickness (100 nm/300

nm/500 nm), beam energy (50 KeV/20 KeV), beam diameter (5 nm/10 nm), total dose (220 $\mu C/cm^2$/250 $\mu C/cm^2$/280 $\mu C/cm^2$), developing time (36 sec/40 sec/45 sec), and conversion formula (low contrast/high contrast). The default settings consist of a feature size of 100 nm, a feature density of 0% (isolated feature), a resist of 300 nm PMMA, a beam energy of 50 KeV, a beam diameter of 5 nm, an average dose of 250 $\mu C/cm^2$, a developing time of 40 sec, and a low contrast conversion formula.

In order to effectively analyze how the region-wise dose contrast is affected by the above system parameters, each of them is changed one at a time while fix all others constant as in the default settings. The results are provided in Table 5.11, Table 5.12, and Table 5.13.

Feature Size (nm)	Feature Density (%)	Resist Thickness (nm)	Beam Energy (KeV)	Beam Diameter (nm)	Total Dose ($\mu C/cm^2$)	Developing Time (sec)	Conversion Formula Contrast	Dose Contrast
100	0	300	50	5	250	40	low	3.32
50	0	300	50	5	250	40	low	6.70
100	0	300	50	5	250	40	low	3.32
100	50	300	50	5	250	40	low	400.2
100	0	100	50	5	250	40	low	1.11
100	0	300	50	5	250	40	low	3.32
100	0	500	50	5	250	40	low	40.9
100	0	300	50	5	250	40	low	3.32
100	0	300	20	5	250	40	low	40.6
100	0	300	50	5	250	40	low	3.32
100	0	300	50	10	250	40	low	6.06
100	0	300	50	5	220	40	low	8.18
100	0	300	50	5	250	40	low	3.32
100	0	300	50	5	280	40	low	1.65
100	0	300	50	5	250	36	low	6.70
100	0	300	50	5	250	40	low	3.32
100	0	300	50	5	250	45	low	1.82
100	0	300	50	5	250	40	low	3.32
100	0	300	50	5	250	40	high	2.23

Table 5.11: Region-wise dose contrast for the Type-V dose distribution.

Feature Size (nm)	Feature Density (%)	Resist Thickness (nm)	Beam Energy (KeV)	Beam Diameter (nm)	Total Dose ($\mu C/cm^2$)	Developing Time (sec)	Conversion Formula Contrast	Dose Contrast
100	0	300	50	5	250	40	low	29.2
50	0	300	50	5	250	40	low	54.8
100	0	300	50	5	250	40	low	29.2
100	50	300	50	5	250	40	low	332.1
100	0	100	50	5	250	40	low	15.5
100	0	300	50	5	250	40	low	29.2
100	0	500	50	5	250	40	low	41.7
100	0	300	50	5	250	40	low	29.2
100	0	300	20	5	250	40	low	126.9
100	0	300	50	5	250	40	low	29.2
100	0	300	50	10	250	40	low	33.1
100	0	300	50	5	220	40	low	33.2
100	0	300	50	5	250	40	low	29.2
100	0	300	50	5	280	40	low	27.2
100	0	300	50	5	250	36	low	30.0
100	0	300	50	5	250	40	low	29.2
100	0	300	50	5	250	45	low	20.1
100	0	300	50	5	250	40	low	29.2
100	0	300	50	5	250	40	high	20.1

Table 5.12: Region-wise dose contrast for the Type-M dose distribution.

From the above tables, it can be seen that a higher contrast dose distribution is usually generated by employing a smaller feature size, a larger feature density, a thicker resist, a lower beam energy, a larger beam diameter, a lower total dose, a shorter developing time, or a lower contrast conversion formula, respectively. For a smaller feature size, the path for the lateral development of the bottom layer of resist to catch up with that of the top layer of resist is shorter. For a larger feature density, the background exposure is higher. For a thicker resist, the exposure variation along the resist depth dimension is larger. For a lower beam energy or a larger beam diameter, the proximity effect is more. For a lower total dose or a shorter developing time, the time for the lateral development of the bottom layer of

Feature Size (nm)	Feature Density (%)	Resist Thickness (nm)	Beam Energy (KeV)	Beam Diameter (nm)	Total Dose ($\mu C/cm^2$)	Developing Time (sec)	Conversion Formula Contrast	Dose Contrast
100	0	300	50	5	250	40	low	20.1
50	0	300	50	5	250	40	low	35.9
100	0	300	50	5	250	40	low	20.1
100	50	300	50	5	250	40	low	495.6
100	0	100	50	5	250	40	low	16.5
100	0	300	50	5	250	40	low	20.1
100	0	500	50	5	250	40	low	72.1
100	0	300	50	5	250	40	low	20.1
100	0	300	20	5	250	40	low	30.0
100	0	300	50	5	250	40	low	20.1
100	0	300	50	10	250	40	low	22.3
100	0	300	50	5	220	40	low	24.6
100	0	300	50	5	250	40	low	20.1
100	0	300	50	5	280	40	low	18.2
100	0	300	50	5	250	36	low	22.3
100	0	300	50	5	250	40	low	20.1
100	0	300	50	5	250	45	low	12.2
100	0	300	50	5	250	40	low	20.1
100	0	300	50	5	250	40	high	10.0

Table 5.13: Region-wise dose contrast for the Type-A dose distribution.

resist to catch up with that of the top layer of resist is less. For a lower contrast conversion formula, the contrast of developing rates between the exposed area and the unexposed area is lower. Therefore, a higher contrast dose distribution can compensate these effects and provide better correction quality.

5.8 Summary

New types of dose distributions, i.e., Type-M and Type-A, have been derived under our 3-D exposure model and 3-D PEC method for achieving the target resist profile of vertical sidewall for nanoscale features with the minimum total dose. The new dose distribution types take the exposure variation along the resist depth dimension (in addition to the lateral dimensions) into account, and balance vertical and lateral developments of resist through

resist layers for realization of the target resist profile. Also, a dose optimization scheme has been developed, which consists of a systematic dose updating procedure coupled with a fast exposure computation and a critical-path-based resist development simulation. This dose optimization scheme is not only fast and effective, but also adaptable to different dose distribution types. Besides, a dose determination scheme has been developed, which utilizes the concept of critical path in dose determination. This scheme can adaptively determine the optimal dose distribution type and the minimum of required total dose based on a given circuit pattern and substrate system settings. The dependency of dose distribution on feature and lithographic parameters has also been analyzed by considering the region-wise dose contrast of each dose distribution type for a variety of system parameters. Through an extensive simulation on single features, large-scale uniform patterns, and large-scale nonuniform patterns, it has been shown that the proposed Type-M and Type-A dose distributions can significantly improve correction results, compared to the conventional Type-V dose distribution, in terms of resist profile, i.e., not only CD error but also sidewall shape, minimizing the total dose. Therefore, the proposed dose distribution types have a good potential to be employed for fabrication of nanoscale features.

Chapter 6

Conclusions

In this dissertation, we addressed the specific issue of control of CD and sidewall shape in true 3-D PEC in e-beam lithography.

In Chapter 2, we developed a fast path-based method for 3-D resist development simulation used for our study. The proposed method employs the concept of development paths to model the development process. In order to minimize the simulation time, we incorporated an adaptive approach into the simulation procedure which reduces the simulation time greatly without sacrificing simulation accuracy substantially. Through an extensive simulation, it has been shown that the resist profiles by the proposed method are well matched with those by the cell removal method, while the proposed method takes much less time for simulation, compared to the cell removal method. Therefore, the proposed path-based method has a good potential to be a practical and efficient alternative to the existing methods such as the time-consuming cell removal method.

In Chapter 3, we studied the problem of estimation of remaining resist profiles. We first formulated a layer-based model by analyzing the simulation results from a set of base patterns on different substrate systems and employed an adaptive procedure in estimation of the lateral development in remaining resist profiles. Then we proposed an adaptive estimation scheme which does not require calculation of exposure distribution and simulation of resist development process. Through simulation and also experiments, it is shown that the proposed method estimates almost the same resist profiles as those by a typical conventional method like the Exp-Dev method in most cases, and outperforms the 2-D Mod method by further reducing the estimation error. Therefore, the proposed method has a good potential

to provide an alternative way for estimation of resist profiles where the conventional methods are not applicable and/or are too time-consuming.

In Chapter 4, we investigated a more challenging problem, i.e., PEC for large-scale uniform patterns. We proposed a new practical method for true 3-D PEC to handle large-scale uniform patterns efficiently, which performs true 3-D PEC by taking into account the exposure variation along the resist depth dimension (in addition to the lateral dimensions). The cost (error) function employed in correction is not the conventional (2-D) CD error, but the 3-D CD error, i.e., the CD errors at multiple layers of resist are considered. Also, we incorporated the resist development simulation into the correction procedure to achieve realistic results. In order to alleviate the computational requirement for large-scale patterns, we developed a critical-location-based correction approach along with the deconvolution surface for deriving the corrected doses for other locations. Through an extensive simulation, it has been shown that the proposed 3-D PEC method can significantly improve correction results, compared to the 2-D PEC method, in terms of resist profile, i.e., not only CD error but also sidewall shape.

In Chapter 5, we made a study of dose distribution types. We derived two new types of dose distributions, i.e., Type-M and Type-A under our 3-D exposure model and 3-D PEC method for achieving the target resist profile of vertical sidewall minimizing the total dose. Their feasibility in 3-D PEC is due to the fact that the lateral development of resist becomes comparable to the vertical development for nanoscale features and the exposure varies along the resist depth dimension with high and low contrasts at the top and bottom layers of resist, respectively. The new dose distribution types take the exposure variation along the resist depth dimension (in addition to the lateral dimensions) into account, and balance vertical and lateral developments of resist through resist layers for realization of the target resist profile. Furthermore, we developed an adaptive dose optimization scheme, which consists of a systematic dose updating procedure coupled with a fast exposure computation and a critical-path-based resist development simulation. This dose optimization scheme is not only fast

and effective, but also adaptable to different dose distribution types. Besides, we developed a dose determination scheme, which utilizes the concept of critical path in dose determination. This scheme can adaptively determine the optimal dose distribution type and the minimum of required total dose based on a given circuit pattern and substrate system settings. We also analyzed the dependency of dose distribution on feature and lithographic parameters by considering the region-wise dose contrast of each dose distribution type for a variety of system parameters. Through an extensive simulation on single features, large-scale uniform patterns, and large-scale nonuniform patterns, it has been shown that the proposed Type-M and Type-A dose distributions can significantly improve correction results, compared to the conventional Type-V dose distribution, in terms of resist profile, i.e., not only CD error but also sidewall shape, minimizing the total dose. Therefore, the proposed dose distribution types have a good potential to be employed for fabrication of nanoscale features.

Bibliography

[1] T. H. P. Chang, "Proximity effect in electron-beam lithography," *J. Vac. Sci. Technol.*, 12(6), pp. 1271-1275, 1975.

[2] M. Parikh, "Self-consistent proximity effect correction technique for resist exposure (SPECTRE)," *J. Vac. Sci. Technol.*, 15(3), pp. 931-933, 1978.

[3] H. Sewell, "Control of pattern dimensions in electron lithography," *J. Vac. Sci. Technol.*, 15(3), pp. 927-930, 1978.

[4] J. C. H. Phang and H. Ahmed, "Line profiles in thick electron resist layers and proximity effect correction," *J. Vac. Sci. Technol.*, 16(6), pp. 1754-1758, 1979.

[5] D. F. Kyser and C. H. Ting, "Voltage dependence of proximity effects in electron beam lithography," *J. Vac. Sci. Technol.*, 16(6), pp. 1759-1763, 1979.

[6] N. Aizaki, "Proximity effect dependence on substrate material," *J. Vac. Sci. Technol.*, 16(6), pp. 1726-1733, 1979.

[7] M. Parikh, "Corrections to proximity effects in electron beam lithography. I. Theory," *J. Appl. Phys.*, 50(6), pp. 4371-4377, 1979.

[8] M. Parikh, "Corrections to proximity effects in electron beam lithography. II. Implementation," *J. Appl. Phys.*, 50(6), pp. 4378-4382, 1979.

[9] M. Parikh, "Corrections to proximity effects in electron beam lithography. III. Experiments," *J. Appl. Phys.*, 50(6), pp. 4383-4387, 1979.

[10] M. Parikh, "Calculation of changes in pattern dimensions to compensate for proximity effects in electron lithography," *J. Appl. Phys.*, 51(1), pp. 705-709, 1980.

[11] A. M. Carroll, "Optimization techniques for proximity effect compensation," *J. Vac. Sci. Technol.*, 19(4), pp. 1296-1299, 1981.

[12] E. Kratschmer, "Verification of a proximity effect correction program in electron-beam lithography," *J. Vac. Sci. Technol.*, 19(4), pp. 1264-1268, 1981.

[13] T. Kato, Y. Watakabe, and H. Nakata, "Proximity effect correction in electron-beam lithography," *J. Vac. Sci. Technol.*, 19(4), pp. 1279-1285, 1981.

[14] J. S. Greeneich, "Proximity effect correction using a dose compensation curve," *J. Vac. Sci. Technol.*, 19(4), pp. 1269-1274, 1981.

[15] J. B. Kruger, P. Rissman, and M. S. Chang, "Silicon transfer layer for multilayer resist systems," *J. Vac. Sci. Technol.*, 19(4), pp. 1320-1324, 1981.

[16] A. M. Carroll, "Proximity-effect correction with linear programming," *J. Appl. Phys.*, 52(1), pp. 434-437, 1981.

[17] Peter Vettiger, Theo Forster, and Dieter P. Kern, "Proximity effect correction on substrates of variable material composition," *J. Vac. Sci. Technol. B*, 1(4), pp. 1378-1382, 1983.

[18] D. G. L. Chow, J. F. McDonald, D. C. King, W. Smith, K. Molnar, and A. J. Steckl, "An image processing approach to fast, efficient proximity correction for electron beam lithography," *J. Vac. Sci. Technol. B*, 1(4), pp. 1383-1390, 1983.

[19] G. Owen and P. Rissman, "Proximity effect correction for electron beam lithography by equalization of background dose," *J. Appl. Phys.*, 54(6), pp. 3573-3581, 1983.

[20] A. S. Chen, A. R. Neureuther, and J. M. Pavkovich, "Proximity effect correction in variably shaped electron-beam lithography," *J. Vac. Sci. Technol. B*, 3(1), pp. 148-152, 1985.

[21] G. Owen, P. Rissman, and M. F. Long, "Application of the GHOST proximity effect correction scheme to round beam and shaped beam electron lithography systems," *J. Vac. Sci. Technol. B*, 3(1), pp. 153-158, 1985.

[22] M. E. Haslam, J. F. McDonald, D. C. King, M. Bourgeois, D. G. L. Chow, and A. J. Steckl, "Two-dimensional Haar thinning for data base compaction in Fourier proximity correction for electron beam lithography," *J. Vac. Sci. Technol. B*, 3(1), pp. 165-173, 1985.

[23] J. M. Pavkovich, "Proximity effect correction calculations by the integral equation approximate solution method," *J. Vac. Sci. Technol. B*, 4(1), pp. 159-163, 1986.

[24] E. Nishimura, T. Takigawa, T. Abe, and Y. Katoh, "Proximity effect reduction in high voltage electron-beam lithography by bias exposure method," *J. Vac. Sci. Technol. B*, 4(1), pp. 164-167, 1986.

[25] M. E. Haslam and J. F. McDonald, "Transform based proximity corrections: Experimental results and comparisons," *J. Vac. Sci. Technol. B*, 4(1), pp. 168-175, 1986.

[26] P. D. Gerber, "Exact solution of the proximity effect equation by a splitting method," *J. Vac. Sci. Technol. B*, 6(1), pp. 432-435, 1988.

[27] M. E. Haslam and J. F. McDonald, "Applying transform based proximity corrections to electron-beam lithography with 0.2-um features," *J. Vac. Sci. Technol. B*, 6(1), pp. 436-442, 1988.

[28] O. W. Otto and A. K. Griffith, "Proximity correction on the AEBLE-150," *J. Vac. Sci. Technol. B*, 6(1), pp. 443-447, 1988.

[29] O. W. Otto and A. K. Griffith, "A parallel processing approach to proximity correction," *J. Vac. Sci. Technol. B*, 6(6), pp. 2048-2052, 1988.

[30] R. L. Kostelak, E. H. Kung, M. G. R. Thomson, and S. Vaidya, "GHOST proximity correction technique: Its parameters, limitations, and process latitude," *J. Vac. Sci. Technol. B*, 6(1), pp. 448-455, 1988.

[31] R. L. Kostelak, E. H. Kung, M. G. R. Thomson, and S. Vaidya, "Evaluation of the proximity effect and GHOST correction technique for submicron electron beam lithography at 50 and 20 kV," *J. Vac. Sci. Technol. B*, 6(6), pp. 2042-2047, 1988.

[32] T. Abe, N. Ikeda, H. Kusakabe, R. Yoshikawa, and T. Takigawa, "Proximity effect correction for an electron beam direct writing system EX-7," *J. Vac. Sci. Technol. B*, 7(6), pp. 1524-1527, 1989.

[33] P. Vermeulen, R. Jonckheere, and L. Van Den Hove, "Proximity-effect correction in electron-beam lithography," *J. Vac. Sci. Technol. B*, 7(6), pp. 1556-1560, 1989.

[34] T. K. Leen, "Theory and practice of proximity correction by secondary exposure," *J. Appl. Phys.*, 65(4), pp. 1776-1781, 1989.

[35] T. Abe and T. Takigawa, "Proximity effect correction for high-voltage electron beam lithography," *J. Appl. Phys.*, 65(11), pp. 4428-4434, 1989.

[36] A. Muray, R. L. Lozes, K. Milner, and G. Hughes, "Proximity effect correction at 10 keV using ghost and sizing for 0.4 um mask lithography," *J. Vac. Sci. Technol. B*, 8(6), pp. 1775-1779, 1990.

[37] G. Owen, "Methods for proximity effect correction in electron lithography," *J. Vac. Sci. Technol. B*, 8(6), pp. 1889-1892, 1990.

[38] H.-Y. Liu and G. Owen, "The effect of resist contrast on linewidth error induced by e-beam proximity exposure," *J. Vac. Sci. Technol. B*, 8(6), pp. 1872-1876, 1990.

[39] R. J. Bojko and B. J. Hughes, "Quantitative lithographic performance of proximity correction for electron beam lithography," *J. Vac. Sci. Technol. B*, 8(6), pp. 1909-1913, 1990.

[40] R. C. Frye, "Adaptive neural network algorithms for computing proximity effect corrections," *J. Vac. Sci. Technol. B*, 9(6), pp. 3054-3058, 1991.

[41] S.-Y. Lee, J. C. Jacob, C.-M. Chen, J. A. McMillan, and N. C. MacDonald, "Proximity effect correction in electron-beam lithography: A hierarchical rule-based scheme - PYRAMID," *J. Vac. Sci. Technol. B*, 9(6), pp. 3048-3053, 1991.

[42] T. Abe, S. Yamasaki, R. Yoshikawa, and T. Takigawa, "The representative figure method for the proximity effect correction [III]," *J. Vac. Sci. Technol. B*, 9(6), pp. 3059-3062, 1991.

[43] M. Hintermaier, U. Hofmann, B. Hubner, C. K. Kalus, E. Knapek, H. W. P. Koops, R. Schlager, E. Seebald, and M. Weber, "Proximity correction using computer aided proximity correction (CAPROX): Evaluation and application," *J. Vac. Sci. Technol. B*, 9(6), pp. 3043-3047, 1991.

[44] K. Harafuji, A. Misaka, K. Kawakita, N. Nomura, H. Hamaguchi, and M. Kawamoto, "Proximity effect correction data processing system for electron beam lithography," *J. Vac. Sci. Technol. B*, 10(1), pp. 133-142, 1992.

[45] J. C. Jacob, S.-Y. Lee, J. A. McMillan, and N. C. MacDonald, "Fast proximity effect correction: An extension of PYRAMID for circuit patterns of arbitrary size," *J. Vac. Sci. Technol. B*, 10(6), pp. 3077-3082, 1992.

[46] F. Murai, H. Yoda, S. Okazaki, N. Saitou, and Y. Sakitani, "Fast proximity effect correction method using a pattern area density map," *J. Vac. Sci. Technol. B*, 10(6), pp. 3072-3076, 1992.

[47] M. A. McCord and T. H. Newman, "Low voltage, high resolution studies of electron beam resist exposure and proximity effect," *J. Vac. Sci. Technol. B*, 10(6), pp. 3083-3087, 1992.

[48] Z. C. H. Tan, K. Standiford, H. Y. Lem, and C. Nurmi, "Characterization of a positive resist and the application of proximity effect correction in electron-beam direct write," *J. Vac. Sci. Technol. B*, 10(6), pp. 3099-3103, 1992.

[49] V. V. Aristov, B. N. Gaifullin, A. A. Svintsov, S. I. Zaitsev, H. F. Raith, and R. Jede, "Accuracy of proximity correction in electron lithography after development," *J. Vac. Sci. Technol. B*, 10(6), pp. 2459-2467, 1992.

[50] M. G. R. Thomson, "Incident dose modification for proximity effect correction," *J. Vac. Sci. Technol. B*, 11(6), pp. 2768-2772, 1993.

[51] T. J. Stark, K. M. Edenfeld, D. P. Griffis, Z. J. Radzimski, and P. E. Russell, "Proximity effects in low-energy electron-beam lithography," *J. Vac. Sci. Technol. B*, 11(6), pp. 2367-2372, 1993.

[52] T. R. Groves, "Efficiency of electron-beam proximity effect correction," *J. Vac. Sci. Technol. B*, 11(6), pp. 2746-2753, 1993.

[53] B. D. Cook and S.-Y. Lee, "Fast proximity effect correction: An extension of PYRAMID for thicker resists," *J. Vac. Sci. Technol. B*, 11(6), pp. 2762-2767, 1993.

[54] K. Moriizumi and A. N. Broers, "Tolerance on alignment error in GHOST proximity effect correction," *J. Vac. Sci. Technol. B*, 11(6), pp. 2114-2120, 1993.

[55] H. Eisenmann, T. Waas, and H. Hartmann, "PROXECCO - Proximity effect correction by convolution," *J. Vac. Sci. Technol. B*, 11(6), pp. 2741-2745, 1993.

[56] E. A. Dobisz, C. R. K. Marrian, R. E. Salvino, M. A. Ancona, F. K. Perkins, and N. H. Turner, "Reduction and elimination of proximity effects," *J. Vac. Sci. Technol. B*, 11(6), pp. 2733-2740, 1993.

[57] S.-Y. Lee and B. D. Cook, "Interior area removal method for PYRAMID," *J. Vac. Sci. Technol. B*, 12(6), pp. 3449-3454, 1994.

[58] G. P. Watson, S. D. Berger, J. A. Liddle, and W. K. Waskiewicz, "A background dose proximity effect correction technique for scattering with angular limitation projection electron lithography implemented in hardware," *J. Vac. Sci. Technol. B*, 13(6), pp. 2504-2507, 1995.

[59] M. C. Peckerar, S. Chang, and C. R. K. Marrian, "Proximity correction algorithms and a co-processor based on regularized optimization. I. Description of the algorithm," *J. Vac. Sci. Technol. B*, 13(6), pp. 2518-2525, 1995.

[60] S. V. Dubonos, B. N. Gaifullin, H. F. Raith, A. A. Svintsov, and S. I. Zaitsev, "Proximity correction for 3D structures," *Microelectron. Eng.*, 27, pp. 195-198, 1995.

[61] T. Waas, H. Eisenmann, O. Vollinger, and H. Hartmann, "Proximity correction for high CD accuracy and process tolerance," *Microelectron. Eng.*, 27, pp. 179-182, 1995.

[62] R. Rau, J. H. McClellan, and T. J. Drabik, "Proximity effect correction for nanolithography," *J. Vac. Sci. Technol. B*, 14(4), pp. 2445-2455, 1996.

[63] T. Abe, "Reticle fabrication by high acceleration voltage electron beam: Representative figure method for proximity effect correction [VI]," *J. Vac. Sci. Technol. B*, 14(4), pp. 2474-2484, 1996.

[64] T. Kasuga, M. Konishi, T. Oda, and S. Moriya, "Studies on correction accuracy of proximity effect for the pattern area density method in electron beam direct writing," *J. Vac. Sci. Technol. B*, 14(6), pp. 3870-3873, 1996.

[65] S.-Y. Lee and B. Liu, "Region-wise proximity effect correction for heterogeneous substrates in electron-beam lithography: Shape modification," *J. Vac. Sci. Technol. B*, 14(6), pp. 3874-3879, 1996.

[66] B. D. Cook and S.-Y. Lee, "Performance analysis and optimal parameter selection for PYRAMID," *Microelectron. Eng.*, 30, pp. 61-64, 1996.

[67] T. A. Fretwell, R. Gurung, and P. L. Jones, "A visualisation and proximity correction tool for submicron E-beam lithography," *Microelectron. Eng.*, 30, pp. 65-68, 1996.

[68] G. P. Watson, L. A. Fetter, and J. A. Liddle, "Dose modification proximity effect correction scheme with inherent forward scattering corrections," *J. Vac. Sci. Technol. B*, 15(6), pp. 2309-2312, 1997.

[69] B. D. Cook and S.-Y. Lee, "Dose, shape, and hybrid modifications for PYRAMID in electron beam proximity effect correction," *J. Vac. Sci. Technol. B*, 15(6), pp. 2303-2308, 1997.

[70] S.-Y. Lee, B. Liu, and B. D. Cook, "Reducing recursive effect for fast proximity correction," *Microelectron. Eng.*, 35, pp. 491-494, 1997.

[71] G. P. Watson, S. D. Berger, and J. A. Liddle, "Characterizing GHOST proximity effect correction effectiveness by determining the worst-case error," *J. Vac. Sci. Technol. B*, 16(6), pp. 3256-3261, 1998.

[72] S.-Y. Lee and J. Laddha, "Adaptive selection of control points for improving accuracy and speed of proximity effect correction," *J. Vac. Sci. Technol. B*, 16(6), pp. 3269-3274, 1998.

[73] S. J. Wind, P. D. Gerber, and H. Rothuizen, "Accuracy and efficiency in electron beam proximity effect correction," *J. Vac. Sci. Technol. B*, 16(6), pp. 3262-3268, 1998.

[74] S.-Y. Lee and B. D. Cook, "PYRAMID-a hierarchical, rule-based approach toward proximity effect correction. I. Exposure estimation," *IEEE Trans. Semicond. Manuf.*, 11(1), pp. 108-116, 1998.

[75] B. D. Cook and S.-Y. Lee, "PYRAMID-a hierarchical, rule-based approach toward proximity effect correction. II. Correction," *IEEE Trans. Semicond. Manuf.*, 11(1), pp. 117-128, 1998.

[76] C. S. Ea and A. D. Brown, "Enhanced pattern area density proximity effect correction," *J. Vac. Sci. Technol. B*, 17(2), pp. 323-333, 1999.

[77] U. Hofmann, R. Crandall, and L. Johnson, "Fundamental performance of state-of-the-art proximity effect correction methods," *J. Vac. Sci. Technol. B*, 17(6), pp. 2940-2944, 1999.

[78] S.-Y. Lee and G. D. Ghare, "Distributed proximity effect correction on a network of workstations," *Microelectron. Eng.*, 46, pp. 291-294, 1999.

[79] V. Boegli, L. Johnson, H. Kao, L. Veneklasen, U. Hofmann, I. Finkelstein, S. Stovall, and S. Rishton, "Implementation of real-time proximity effect correction in a raster shaped beam tool," *J. Vac. Sci. Technol. B*, 18(6), pp. 3138-3142, 2000.

[80] K. Takahashi, M. Osawa, M. Sato, H. Arimoto, K. Ogino, H. Hoshino, and Y. Machida, "Proximity effect correction using pattern shape modification and area density map," *J. Vac. Sci. Technol. B*, 18(6), pp. 3150-3157, 2000.

[81] S.-Y. Lee and J. Laddha, "Application of neural network to enhancing accuracy of E-beam proximity effect correction," *Microelectron. Eng.*, 53, pp. 317-320, 2000.

[82] C. S. Ea and A. D. Brown, "Incorporating a corner correction scheme into enhanced pattern area density proximity effect correction," *J. Vac. Sci. Technol. B*, 19(5), pp. 1985-1988, 2001.

[83] M. Osawa, K. Takahashi, M. Sato, H. Arimoto, K. Ogino, H. Hoshino, and Y. Machida, "Proximity effect correction using pattern shape modification and area density map for electron-beam projection lithography," *J. Vac. Sci. Technol. B*, 19(6), pp. 2483-2487, 2001.

[84] S.-Y. Lee and J. Laddha, "Automatic determination of spatial dose distribution for improved accuracy in e-beam proximity effect correction," *Microelectron. Eng.*, 57-58, pp. 303-309, 2001.

[85] S.-Y. Lee and J. Laddha, "A hierarchical pattern representation format for proximity effect correction in E-beam lithography," *Microelectron. Eng.*, 57-58, pp. 311-319, 2001.

[86] K. Ogino, H. Hoshino, Y. Machida, M. Osawa, H. Arimoto, K. Takahashi, and H. Yamashita, "High-performance proximity effect correction for sub-70 nm design rule system on chip devices in 100 kV electron projection lithography," *J. Vac. Sci. Technol. B*, 21(6), pp. 2663-2667, 2003.

[87] F. Hu and S.-Y. Lee, "Dose control for fabrication of grayscale structures using a single step electron-beam lithographic process," *J. Vac. Sci. Technol. B*, 21(6), pp. 2672-2679, 2003.

[88] S.-Y. Lee and D. He, "Simultaneous dose modification for balanced E-beam proximity correction minimizing CD error," *Microelectron. Eng.*, 69(1), pp. 47-56, 2003.

[89] S.-Y. Lee, F. Hu, and J. Ji, "Representation of nonrectangular features for exposure estimation and proximity effect correction in electron-beam lithography," *J. Vac. Sci. Technol. B*, 22(6), pp. 2929-2935, 2004.

[90] M. Osawa, K. Ogino, H. Hoshino, Y. Machida, and H. Arimoto, "3D proximity effect correction based on the simplified electron energy flux model in electron-beam lithography," *J. Vac. Sci. Technol. B*, 22(6), pp. 2923-2928, 2004.

[91] L. H. A. Leunissen, R. Jonckheere, U. Hofmann, N. Unal, and C. Kalus, "Experimental and simulation comparison of electron-beam proximity correction," *J. Vac. Sci. Technol. B*, 22(6), pp. 2943-2947, 2004.

[92] H. Yamashita, J. Yamamoto, F. Koba, and H. Arimoto, "Proximity effect correction using blur map in electron projection lithography," *J. Vac. Sci. Technol. B*, 23(6), pp. 3188-3192, 2005.

[93] R. Murali, D. K. Brown, K. P. Martin, and J. D. Meindl, "Process optimization and proximity effect correction for gray scale e-beam lithography," *J. Vac. Sci. Technol. B*, 24(6), pp. 2936-2939, 2006.

[94] S.-Y. Lee and K. Anbumony, "Analysis of three-dimensional proximity effect in electron-beam lithography," *Microelectron. Eng.*, 83(2), pp. 336-344, 2006.

[95] K. Anbumony and S.-Y. Lee, "True three-dimensional proximity effect correction in electron-beam lithography," *J. Vac. Sci. Technol. B*, 24(6), pp. 3115-3120, 2006.

[96] S.-Y. Lee and K. Anbumony, "Accurate control of remaining resist depth for nanoscale three-dimensional structures in electron-beam grayscale lithography," *J. Vac. Sci. Technol. B*, 25(6), pp. 2008-2012, 2007.

[97] M. Peckerar, D. Sander, A. Srivastava, A. Foli, and U. Vishkin, "Electron beam and optical proximity effect reduction for nanolithography: New results," *J. Vac. Sci. Technol. B*, 25(6), pp. 2288-2294, 2007.

[98] K. Ogino, H. Hoshino, and Y. Machida, "Process variation-aware three-dimensional proximity effect correction for electron beam direct writing at 45 nm node and beyond," *J. Vac. Sci. Technol. B*, 26(6), pp. 2032-2038, 2008.

[99] L. E. Ocola, "Nanoscale geometry assisted proximity effect correction for electron beam direct write nanolithography," *J. Vac. Sci. Technol. B*, 27(6), pp. 2569-2571, 2009.

[100] J. Bolten, T. Wahlbrink, N. Koo, H. Kurz, S. Stammberger, U. Hofmann, and N. Unal, "Improved CD control and line edge roughness in E-beam lithography through combining proximity effect correction with gray scale techniques," *Microelectron. Eng.*, 87, pp. 1041-1043, 2010.

[101] N. Unal, D. Mahalu, O. Raslin, D. Ritter, C. Sambale, and U. Hofmann, "Third dimension of proximity effect correction (PEC)," *Microelectron. Eng.*, 87, pp. 940-942, 2010.

[102] T. Klimpel, M. Schulz, R. Zimmermann, H.-J. Stock, and A. Zepka, "Model based hybrid proximity effect correction scheme combining dose modulation and shape adjustments," *J. Vac. Sci. Technol. B*, 29(6), pp. 06F315, 2011.

[103] Q. Dai, S.-Y. Lee, S.-H. Lee, B.-G. Kim, and H.-K. Cho, "Estimation of resist profile for line/space patterns using layer-based exposure modeling in electron-beam lithography," *Microelectron. Eng.*, 88(6), pp. 902-908, 2011.

[104] Q. Dai, S.-Y. Lee, S.-H. Lee, B.-G. Kim, and H.-K. Cho, "Three-dimensional proximity effect correction for large-scale uniform patterns," *J. Vac. Sci. Technol. B*, 29(6), pp. 06F314, 2011.

[105] Q. Dai, S.-Y. Lee, S.-H. Lee, B.-G. Kim, and H.-K. Cho, "New types of dose distributions for vertical sidewall minimizing total dose in 3-D electron-beam proximity effect correction of nanoscale features," *J. Vac. Sci. Technol. B*, 30(6), pp. 06F307, 2012.

[106] S. J. Wind, M. G. Rosenfield, G. Pepper, W. W. Molzen, and P. D. Gerber, "Proximity correction for electron beam lithography using a three-Gaussian model of the electron energy distribution," *J. Vac. Sci. Technol. B*, 7(6), pp. 1507-1512, 1989.

[107] M. Gentili, L. Grella, A. Lucchesini, L. Luciani, L. Mastrogiacomo, and P. Musumeci, "Energy density function determination in very-high-resolution electron-beam lithography," *J. Vac. Sci. Technol. B*, 8(6), pp. 1867-1871, 1990.

[108] M. G. Rosenfield, S. J. Wind, W. W. Molzen, and P. D. Gerber, "Determination of proximity effect correction parameters for 0.1 um electron-beam lithography," *Microelectron. Eng.*, 11, pp. 617-623, 1990.

[109] A. Misaka, K. Harafuji, and N. Nomura, "Determination of proximity effect parameters in electron-beam lithography," *J. Appl. Phys.*, 68(12), pp. 6472-6479, 1990.

[110] T. A. Fretwell, R. Gurung, and P. L. Jones, "Curve fitting to Monte Carlo data for the determination of proximity effect correction parameters," *Microelectron. Eng.*, 17, pp. 389-394, 1992.

[111] S. Johnson, "Simulation of electron scattering in complex nanostructures: Lithography, metrology, and characterization," *Ph.D. Dissertation*, Cornell University, Ithaca, NY, 1992.

[112] E. Seo, B.-K. Choi, and O. Kim, "Determination of proximity effect parameters and the shape bias parameter in electron beam lithography," *Microelectron. Eng.*, 53, pp. 305-308, 2000.

[113] M. Rooks, N. Belic, E. Kratschmer, and R. Viswanathan, "Experimental optimization of the electron-beam proximity effect forward scattering parameter," *J. Vac. Sci. Technol. B*, 23(6), pp. 2769-2774, 2005.

[114] J. Zhou and X. Yang, "Monte Carlo simulation of process parameters in electron beam lithography for thick resist patterning," *J. Vac. Sci. Technol. B*, 24(3), pp. 1202-1209, 2006.

[115] D. Drouin, A. R. Couture, D. Joly, X. Tastet, V. Aimez, and R. Gauvin, "CASINO V2.42 - A fast and easy-to-use modeling tool for scanning electron microscopy and microanalysis users," *Scanning.*, 29, pp. 92-101, 2007.

[116] M. Hauptmann, K.-H. Choi, P. Jaschinsky, C. Hohle, J. Kretz, and L. M. Eng, "Determination of proximity effect parameters by means of CD-linearity in sub 100 nm electron beam lithography," *Microelectron. Eng.*, 86, pp. 539-543, 2009.

[117] S.-Y. Lee, Q. Dai, S.-H. Lee, B.-G. Kim, and H.-K. Cho, "Enhancement of spatial resolution in generating point spread functions by Monte Carlo simulation in electron-beam lithography," *J. Vac. Sci. Technol. B*, 29(6), pp. 06F902, 2011.

[118] Q. Dai, S.-Y. Lee, S.-H. Lee, B.-G. Kim, and H.-K. Cho, "Experiment-based estimation of point spread function in electron-beam lithography: Forward-scattering part," *Microelectron. Eng.*, 88(10), pp. 3054-3061, 2011.

[119] B. A. Nilsson, "Experimental evaluation method of point spread functions used for proximity effects correction in electron beam lithography," *J. Vac. Sci. Technol. B*, 29(6), pp. 06F311, 2011.

[120] N. Unal, M. D. B. Charlton, Y. Wang, U. Waizmann, T. Reindl, and U. Hofmann, "Easy to adapt electron beam proximity effect correction parameter calibration based on visual inspection of a Best Dose Sensor," *Microelectron. Eng.*, 88(8), pp. 2158-2162, 2011.

[121] H. Demers, N. Poirier-Demers, A. R. Couture, D. Joly, M. Guilmain, N. de Jonge, D. Drouin, "Three-dimensional electron microscopy simulation with the CASINO Monte Carlo software," *Scanning.*, 33, pp. 135-146, 2011.

[122] Y. Hirai, S. Tomida, K. Ikeda, M. Sasago, M. Endo, S. Hayama, and N. Nomura, "Three-dimensional resist process simulator PEACE," *IEEE Trans. Comput.-Aided Des.*, 10(6), pp. 802-807, 1991.